DIELECTRIC FILM CHARACTERIZATION BEYOND CLASSICAL LIMITS EXPLOITING SPATIALLY STRUCTURED ENTANGLED PHOTON PAIRS

A Thesis Submitted to
the Graduate School of
İzmir Institute of Technology
in Partial Fulfillment of the Requirements for the Degree of

DOCTOR OF PHILOSOPHY

in Electronics and Communication Engineering

by
Enes ATAÇ

June 2024
İZMİR

We approve the thesis of **Enes ATAÇ**

Examining Committee Members:

Prof. Dr. Mehmet Salih DİNLEYİCİ
Department of Electrical and Electronics Engineering, İzmir Institute of Technology

Assoc. Prof. Dr. Kıvılcım YÜKSEL ALDOĞAN
Department of Electrical and Electronics Engineering, İzmir Institute of Technology

Assist. Prof. Dr. Aziz KOLKIRAN
Department of Engineering Sciences, İzmir Kâtip Çelebi University

Assoc. Prof. Dr. Sevilay SEVİNÇLİ
Department of Photonics, İzmir Institute of Technology

Prof. Dr. Metin Hüseyin SABUNCU
Department of Electrical and Electronics Engineering, Dokuz Eylül University

28 June 2024

Prof. Dr. Mehmet Salih DİNLEYİCİ
Supervisor, Department of Electrical and Electronics Engineering
İzmir Institute of Technology

Prof. Dr. Mustafa Aziz ALTINKAYA
Head of the Department of
Electrical and Electronics Engineering

Prof. Dr. Mehtap EANES
Dean of the Graduate School of
Engineering and Sciences

ACKNOWLEDGMENTS

This thesis and the study that it contains would not have been possible without the contributions of a number of different people around me.

First and foremost I would like to express my sincere thanks to my advisor, Prof. M. Salih Dinleyici, for entrusting me with the invaluable chance to delve into the fascinating research domain of quantum sensing and metrology. I am deeply grateful for your unwavering support and guidance throughout every phase of my thesis research. Your enthusiasm always encourages me.

I owe particular thanks to each and every member of the thesis committee: Prof. Metin Sabuncu and Prof. Sevilay Sevinçli for valuable contributions which helped me a lot in revising the thesis, without which many arguments in the thesis would have been obscure. Special thanks go to Prof. Aziz Kolkıran and Prof. Kıvılcım Yüksel Aldoğan for serving on my thesis progress committee, as well as for constructive criticisms, and for the ongoing mentorship. I will always have the honor of having you in the jury.

I would like to extend my heartfelt gratitude to those who have supported and encouraged me throughout my PhD journey. To Simay Yılmaz, thank you for your pure and sincere friendship; your presence has been a source of comfort and joy. İrem Cumalı, your positivity and cheerful disposition have been a beacon of light during challenging times. Önder Yılmaz, thank you for your unique personality, insightful ideas, and wonderful friendship. Orkan Olcay and Fatih Onay, your steadfast support and encouraging words have always inspired and motivated me. Each of you has contributed significantly to this journey, and I am deeply grateful for your support. Finally, I could not imagine a PhD journey without the unwavering friendships of Çağın Ekici and Anıl Karatay, my closest allies. I would like to extend my special thanks to them for their significant contributions to the discussions related to my thesis.

Last but definitely not least, my eternal gratitude goes to my parents, Hüseyin and Fahriye Ataç, and my sister Özge Ataç for their years of love and unconditional endless support. The work is dedicated to each of them individually.

ABSTRACT

DIELECTRIC FILM CHARACTERIZATION BEYOND CLASSICAL LIMITS EXPLOITING SPATIALLY STRUCTURED ENTANGLED PHOTON PAIRS

Quantum optics introduces new opportunities, alternative methodologies, and potentially groundbreaking technologies centered around generating, manipulating, and detecting distinct quantum states of light. This field opens up new avenues for exploration and application in instrumentation, measurement, and metrology. From this point of view, the main objective of the thesis is to propose a novel quantum entanglement-based phase diffraction scheme for the thickness characterization of ultra-thin transparent dielectric films on an optical fiber beyond classical limits. In addition, since coincidence detection and optical coherence have an essential role in the suggested system, we also present a practical and non-sophisticated measurement procedure for thermal light characterization by extracting time bin information from spatially distributed intensity data using a standard CCD camera.

To accomplish the aforementioned purposes, we first examine the effect of entanglement on measurement systems, specifically optical microscopy, since it intrinsically offers better optical resolution. Then, the spatial entanglement concept is integrated with the phase diffraction scheme for dielectric film characterization on a curved surface. An alternative configuration with thermal photons is also demonstrated. According to the outcomes, the thickness of the transparent dielectric films can be accurately estimated below one-twentieth of the wavelength of interest. In the second part, we have introduced a proof-of-concept experimental setup by exploiting the single-pixel intensity measurements of a conventional CCD camera to extract thermal light photon statistics and second-order coherence function. In this way, we proved that the bunched light phenomenon can be observed with off-the-shelf detectors beyond coherence time. A comprehensive feasibility analysis of the CCD camera is also reported.

Finally, the results are evaluated with pros and cons, drawing a road map for future works. We have briefly explained promising perspectives including the N-fold detection scheme, the influence of pump coherence on the characterization system and practical engineering applications of proposed photon statistics setup.

ÖZET

UZAYSAL YAPILANDIRILMIŞ DOLANIK FOTON ÇİFTLERİNDEN FAYDALANARAK KLASİK KIRINIM SINIRLARI ÖTESİNDE DİELEKTRİK FİLM KARAKTERİZASYONU

Kuantum optiği, ışığın farklı kuantum durumlarını üretmeye, manipüle etmeye ve tespit etmeye odaklanan yeni fırsatlar, alternatif metodolojiler ve potansiyel olarak çığır açıcı teknolojiler sunar. Bu alan enstrümantasyon, ölçüm ve metrolojide keşif ve uygulama için yeni yollar açmaktadır. Buradan hareketle tezin temel amacı, klasik sınırların ötesinde bir optik fiber üzerindeki ultra-ince şeffaf dielektrik filmlerin kalınlık karakterizasyonuna dayalı yeni bir kuantum dolaşıklık tabanlı faz kırınım şeması önermektir. Ek olarak, önerilen sistemde çakışma tespiti ve optik tutarlılık önemli bir rol oynadığından, standart bir CCD kamera kullanarak mekansal olarak dağıtılmış yoğunluk verilerinden zaman aralığı bilgisini çıkararak termal ışık karakterizasyonu için pratik ve karmaşık olmayan bir ölçüm prosedürü de sunuyoruz.

Yukarıda belirtilen amaçları gerçekleştirmek için öncelikle kuantum dolanıklığın ölçüm sistemleri üzerindeki etkisini, özellikle de doğası gereği daha iyi çözünürlük sunduğundan, optik mikroskopiyi inceledik. Daha sonra, uzaysal dolaşıklık kavramı, kavisli bir yüzey üzerinde dielektrik film karakterizasyonu için faz kırınım şeması ile entegre edilir. Termal fotonlarla alternatif bir konfigürasyon da gösterilmiştir. Sonuçlara göre, şeffaf dielektrik filmlerin kalınlığı, ilgilenilen dalga boyunun yirmide birinin altında doğrulukta tahmin edilebilmektedir. İkinci bölümde, termal ışık foton istatistiklerinin ve ikinci dereceden tutarlılık fonksiyonunun çıkarılması için geleneksel bir CCD kameranın tek piksel yoğunluk ölçümlerinden yararlanarak kavram kanıtı deney düzeneğini tanıttık. Böylece, kümelenmiş ışık olgusunun tutarlılık süresinin ötesinde kullanıma hazır dedektörlerle gözlemlenebileceğini kanıtladık. CCD kameranın kapsamlı bir fizibilite analizi de rapor edilmiştir.

Son olarak, sonuçlar artıları ve eksileri ile değerlendirilerek gelecekteki çalışmalar için bir yol haritası çizilmiştir. N-katlı algılama şeması, pompa tutarlılığının karakterizasyon sistemi üzerindeki etkisi ve önerilen foton istatistik kurulumunun pratik mühendislik uygulamaları dahil olmak üzere umut verici perspektifleri kısaca açıkladık.

TABLE OF CONTENTS

LIST OF FIGURES

Figure **Page**

Figure **Page**

Figure **Page**

Figure **Page**

Figure **Page**

LIST OF TABLES

Table **Page**

LIST OF ABBREVIATIONS

CCD . . . . . Charge Coupled Device
EMCCD . . . . . Electron Multiplying Charge Coupled Device
EPR . . . . . Einstein-Podolsky-Rosen
HBT . . . . . Hanbury Brown-Twiss
FBG . . . . . Fiber Bragg Grating
ICCD . . . . . Intensified Charge Coupled Device
ITO . . . . . Indium Tin Oxide
LED . . . . . Light Emitting Diode
ND . . . . . Neutral Density
OCT . . . . . Optical Coherence Tomography
QED . . . . . Quantum Electrodynamics
PVA . . . . . Poly Vinly Alcohol
SNR . . . . . Signal-to-Noise Ratio
SPDC . . . . . Spontaneous Parametric Down-Conversion
SPR . . . . . Surface Plasmon Resonance

CHAPTER 1

INTRODUCTION

Over the last decades, many research and studies have aimed to understand the quantum features held within light, which contribute towards establishing quantum optics. Such investigations not only enlighten us to realize and explore the quantum behaviors of light but also introduce new paradigms in our understanding of its interactions with matter, marking a transformative epoch in the landscape of optical science (Agarwal,2012; Garrison and Chiao, 2008; Simon et al., 2017). The theoretical framework of the field of quantum optics offers the opportunity to exploit powerful tools that can not be explained classically. The generation and detection of non-classical light states are the primary goals of quantum optics. These states have drawn much attention, especially in metrology and information technology.

In light of all these considerations, my Ph.D. research mainly presents novel and practical instrumentation, measurement, and metrology techniques and procedures, focusing on two main subjects: (1) novel quantum-based solutions for enhancing the thickness determination of ultra-thin dielectric films in the characterization systems beyond classical limits and (2) design and construction of practical photon statistics and optical coherence setups utilizing ordinary, non-sophisticated and low-cost laboratory pieces of equipment, including comprehensive analysis supported by numerical simulations and experiments. To achieve and realize the purposes above, five fundamental research areas in classical and quantum optics have been combined: dielectric film characterization, phase diffraction, quantum metrology, photon statistics, and photoelectric detection of light. Therefore, this chapter is devoted to clearly explaining the motivation of the thesis by evaluating and discussing essential studies in the literature. This way, the advances and fundamental shortcomings in these research areas are shown to the readers by emphasizing their strong and weak sides.

1.1. Dielectric Films in Optical Fiber Sensors

Thin dielectric films constitute an essential subject area within the field of fiber optic sensor technologies, finding prominent applications in devices such as fiber Bragg

gratings (FBG) and surface plasmon resonance (SPR) sensors (Mishra and Gupta, 2012; Alwis et al., 2012). These sensors usually serve as transducers, interrogators or sensing elements. They have numerous application areas for crucial parameters such as temperature (Mishra et al., 2016; Leal-Junior et al., 2018), strain (Sampath et al., 2018), gas sensing (Mishra et al., 2016; Zhou et al., 2021), humidity (Woyessa et al., 2016; Premkumar and Vadivel, 2017) and molecular interactions (Gong et al., 2021; Sezemsky et al., 2021). In general, they are intricately conjuncted with specific sub-wavelength dielectric films to achieve more intelligent sensing capabilities, as evidenced in existing literature (Li et al., 2020; Wang et al., 2017). Nevertheless, the performance of these sensors is significantly affected by subtle variations in the thickness and surface roughness of the employed dielectric films (Zhang et al., 2013; Verma et al., 2019; Rajendran et al., 2024). Therefore, precise and well-defined optical characterization of the films has become an important and challenging subject for quality assurance in recent years.

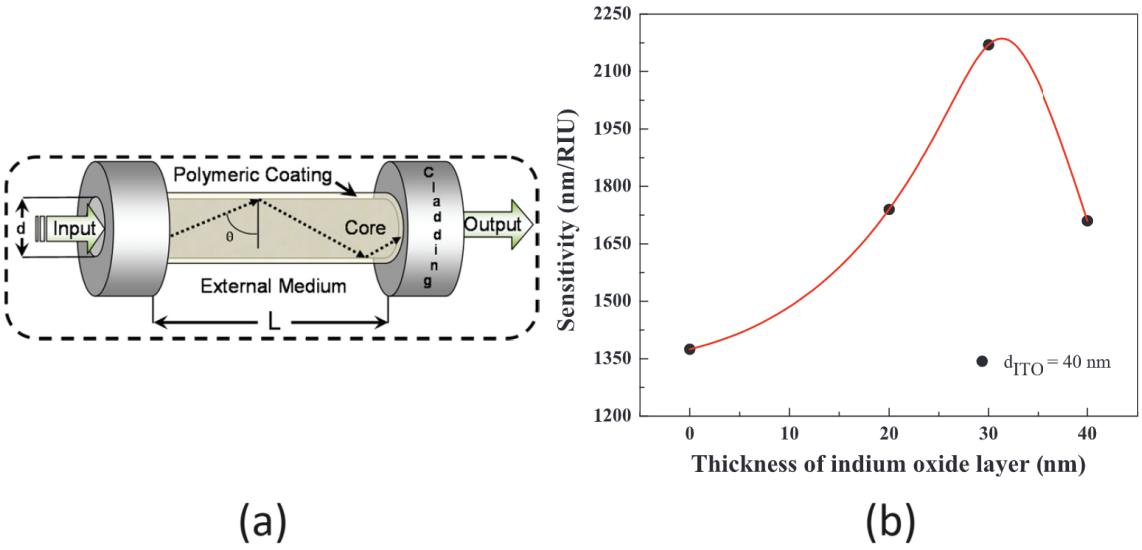

Figure 1.1. (a) Typical configuration of polymer coated optical fiber (Zamarreño et al., 2011) (b) Sensitivity variation of dielectric layer (IO) for various thickness (Kapoor and Sharma, 2020)

Figure 1.1(a) gives a typical and basic configuration of dielectric film-coated optical fiber. The cladding part of the fiber is usually removed and replaced by a particular thin film (e.g., indium-tin oxide, poly-vinyl alcohol, poly-acrylic acid) that is sensitive in pursuit of measuring the desired quantity. The desired quantity can be determined precisely by evaluating the variations in the spectrum of incident light, explicitly depending

on the parameters of dielectric coating (e.g., refractive index and thickness) (Riza et al., 2020). However, nanoscale variations on the thickness of dielectric films strongly affect the sensitivity (or resolution) of the optical fiber sensor as seen in Figure 1.1(b). This specific example reveals that the sensitivity takes its maximum value at around 30 nm and even a few nanometers of variation in film thickness can reduce sensitivity to insufficient levels.

As the thickness of dielectric films is a small fraction of the wavelength of interest, notably around 50 nm, particularly in the context of SPR sensors, the precise and accurate determination of optical properties at the nanoscale is essential and challenging task for optimizing sensor precision. In literature, the prevalent methods for thickness characterization mostly depends on advanced interferometric (Kim, 2022; Nestler and Helm, 2017) and spectroscopic (Yoshino et al., 2017; Debnath et al., 2009) techniques. However, the implementation of these techniques demands intricate procedures involving expensive and finely calibrated measurement equipment. Furthermore, the complexity of the characterization process significantly increases, particularly for curved substrates due to the geometric nuances and the necessity for pointwise scanning of the sample. Hence, these consequences compels the need to advance methods dealing with the complexities needed to achieve higher precision, especially when using curved substrates.

1.2. Phase Diffraction in Optical Characterization

Phase diffraction is a wealthy subject and potent property to characterize the optical properties of transparent objects (e.g., solids, liquids, dielectric films). It arises from the interaction between an incident light wave and a phase object (Ekici and Dinleyici, 2017). Since the phase of the diffracted field from the phase objects is extremely sensitive to slight variations on the thickness and refractive index through the optical path length, it carries valuable information about the system (Tavassoly et al., 2001; Sabatyan and Tavassoly, 2009; Tavassoly and Saber, 2010). The general scheme of the conventional phase diffraction-based optical characterization systems and experimental setup is given in Figure 1.2 and Figure 1.3, respectively. The working principle mainly depends on Fresnel diffraction theory exploiting the tracing incident wavefront through the optical path (Volpe et al., 2017). In the proposed system, the wavefront is usually modeled by the paraxial complex rays, including amplitude and phase. The input wavefront undergoes specific phase delays while traversing through the phase object such as optical fiber. At the end of tracing, the field distribution on the detector (or image plane) is obtained. Given

the phase's exquisite sensitivity to small variations in the optical parameters through the optical path, the resulting diffraction pattern on the detector is modified. Considering that the thickness of the dielectric film is a variable of the optical path, the nanoscale variations in thickness can be extracted by evaluating the minima shifts and amplitude deviations on the recorded intensity pattern (Ataç, 2019).

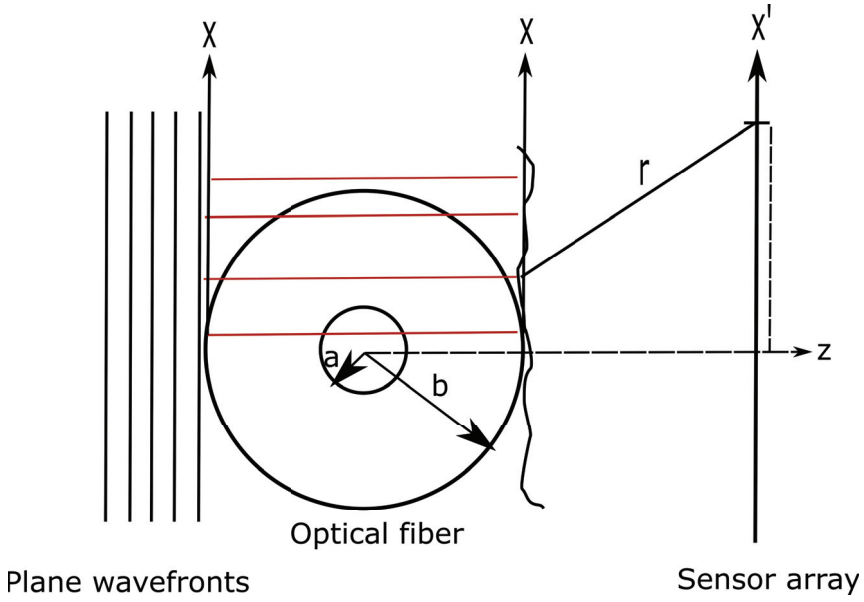

Figure 1.2. Illustration of classical phase diffraction from optical fiber with a plane wave input

In the literature, some proposed phase diffraction schemes utilize optical and computational manipulations to detect sub-wavelength thickness variations in the order of a few tens of nanometers. It has been demonstrated (Ataç and Dinleyici, 2020) that the thickness of a nanoscale thin film can be determined approximately with a resolution of about one-tenth of the wavelength of interest, leveraging the combination of conventional phase diffraction technique and spatially structured illumination. Besides, the system should have been optimized with neural networks to increase the resolution further (Ataç et al., 2023). Although the results are far beyond the classical diffraction limits, which approximately correspond $\lambda/2$ (Monticone et al., 2014), recent developments in fiber optic sensor technologies need more precise measurements to extract optical properties of phase objects on nanoscales since they have a substantial effect on the performance of sensors (Liu et al., 2020; Villeneuve-Faure et al., 2018). Despite the phase diffraction's recognition as a potent, straightforward, and cost-effective method in optical characteri-

zation techniques, the classical light sources and measurement procedures utilized in the schemes impose inherent limitations on thickness resolution. Therefore, shifting characterization techniques to quantum-based models could be a solution to enhance system resolution.

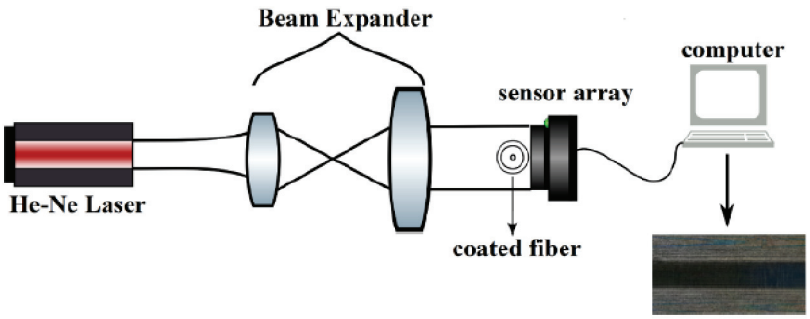

(a)

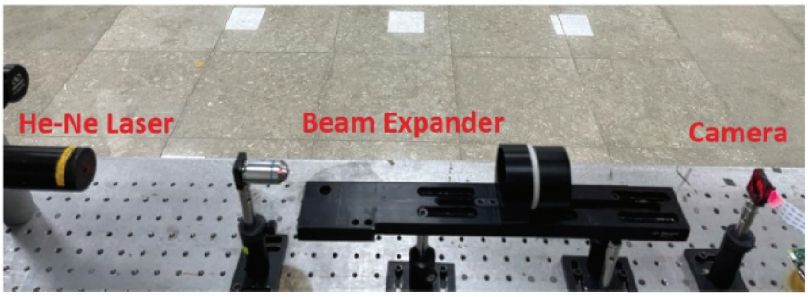

(b)

Figure 1.3. (a) The scheme for phase diffraction from the coated optical fiber (b) experimental photo (Ataç et al., 2023)

1.3. Quantum Metrology for Optical Characterization

Metrology occupies a central and indispensable role in the domains of science and engineering. In essence, its focal point is the pursuit of optimal precision in diverse parameter estimation tasks, along with the identification of measurement methodologies capable of attaining such precision (an interferometer example given in Figure 1.4). At the beginning of metrology science, it focused on classical and semi-classical systems, encompassing mechanical systems explicable by classical physics and optical systems

modeled through classical wave optics (Sirohi, 2017; Bernd et al., 2012). However, due to the constraints imposed by classical physics (e.g., diffraction limit, shot noise), classical metrology is naturally limited in its precision (Xiang and Guo, 2013). Therefore, new methodologies and techniques have been investigated to improve system precision beyond classical limits, especially by exploiting the inherent advantages of quantum optics, the most common example of which is quantum entanglement (Nawrocki, 2015).

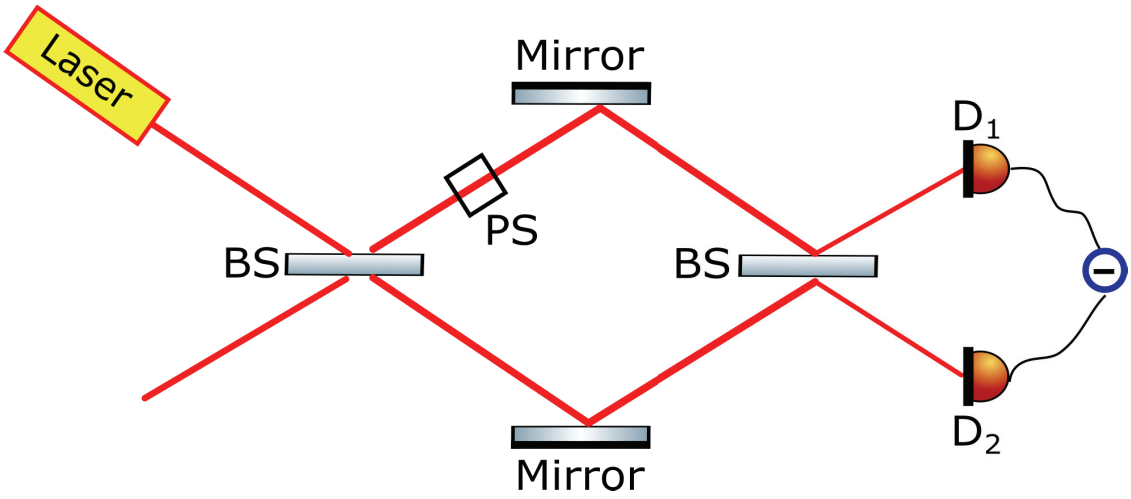

Figure 1.4. A classical optical metrology setup: Conventional Mach−Zehnder interferometry with coherent light input and intensity difference detection. BS: Beam splitter, PS: Phase shifter D_i: Detector

Fundamentally, all processes of measurement are subject to the principles of quantum mechanics (Taylor and Bowen, 2016). This reality points to the fact that it is imperative to incorporate quantum mechanics into the analysis to ascertain the ultimate constraints of these technologies. Therefore, like quantum computing, quantum information processing, or quantum cryptography, metrology has undergone a reexamination to incorporate the consequences of quantum mechanics (Dowling and Seshadreesan, 2014). From this point of view, quantum metrology has demonstrated the capacity to achieve measurement precision surpassing classical limits (DeMille et al., 2024), evolving into a compelling frontier of research with promising potential applications in recent years as quantum sensing (Giovannetti et al., 2011), quantum imaging (Shih, 2007; Cameron et al., 2024) and quantum lithography (Dowling, 2008).

Quantum metrology mainly provides a theoretical framework suitable for assessing the precision performance of measurement devices leveraging quantum mechanical probes endowed with non-classical features such as entanglement or squeezing (Giovan-

netti et al., 2006). In Figure 1.5, a typical scenario of parameter estimation is given. In the concept of the system, the preparation of probes in appropriate quantum states is initiated, subject them to evolution through the process, and employ a well-suited detection strategy to measure the probes at the output. Subsequently, a comparative analysis between the input and output probe states is conducted, facilitating the estimation of the unknown parameter associated with the physical process. It has been proven that when N probes are characterized by quantum entanglement conversely N classical probes, the determination of the unknown parameter becomes possible with a precision that scales inversely as $1/N$, which is known as Heisenberg limit, in optical interferometry systems (Holland and Burnett, 1993; Demkowicz-Dobrzański et al., 2012). In addition, the same quantum enhancement method can be utilized in atomic spectroscopy where spin-squeezed states have been used to enhance the precision of frequency calibration (Meyer et al., 2001)

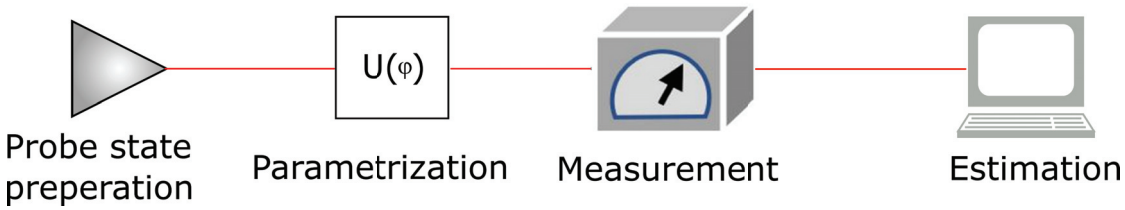

Figure 1.5. A schematic of the quantum parameter estimation

It has also been proven that the utilization of intensity correlations, as a metrology technique, could improve the optical resolution by coincidence detection for microscopic applications (Simon and Sergienko, 2010a). In the last decade, similar correlation techniques have been used in quantum-based imaging systems by the concept of spatial entanglement generated via spontaneous parametric down-conversion (SPDC) (Simon and Sergienko, 2010b; Abouraddy et al., 2002; D'Angelo et al., 2001). By considering the effect of quantum entanglement on system precision, the utilization of quantum entanglement-based systems for dielectric film characterization, as a probe, may be helpful in improving system sensitivity. This idea may be integrated with the phase diffraction scheme. To further improve the system resolution, spatially entangled photons are also combined with a pinhole to block stray lights, which is the essential principle of confocal quantum microscopy (Karmakar, 2019). In this way, the carried thickness information traversing to the phase object is doubled courtesy of entangled photons, and confocality is provided with the help of a compatible aperture. Considering the main objective of

the thesis, this approach may provide significant enhancement for the determination of ultra-thin film thickness more accurately.

1.4. Photon Statistics of Light Sources

The probability distribution of the photon number carries significant information to describe the physical processes or systems. Together with the optical mode's structure and the state of coherence, these statistics furnish a comprehensive account of light properties. Therefore, accurate assessment of photon statistics is a necessity for numerous applications, such as non-classical light sources (Waks et al., 2004), quantum metrology (Couteau et al., 2023) and quantum communication (Wakui et al., 2014). Statistical correlations, on the other hand, find applications in a wide range of areas, from describing both classical and quantum nature of light (Turunen et al., 2022; Yu et al., 2023; Torres et al., 2003) to the emerging field of imaging (Gatti et al., 2004; Albarelli et al., 2020; Gilaberte Basset et al., 2019). In the literature, there are various studies and methods for photon statistics (Hloušek et al., 2019; Zubizarreta Casalengua et al., 2020) and coherence properties of the light (Laiho et al., 2022; Boitier et al., 2009; Kuhn et al., 2016; Liu et al., 2019). However, measurement complexity and adequate instrumentation requirements vary significantly by fundamental source types: thermal, coherent, and non-classical.

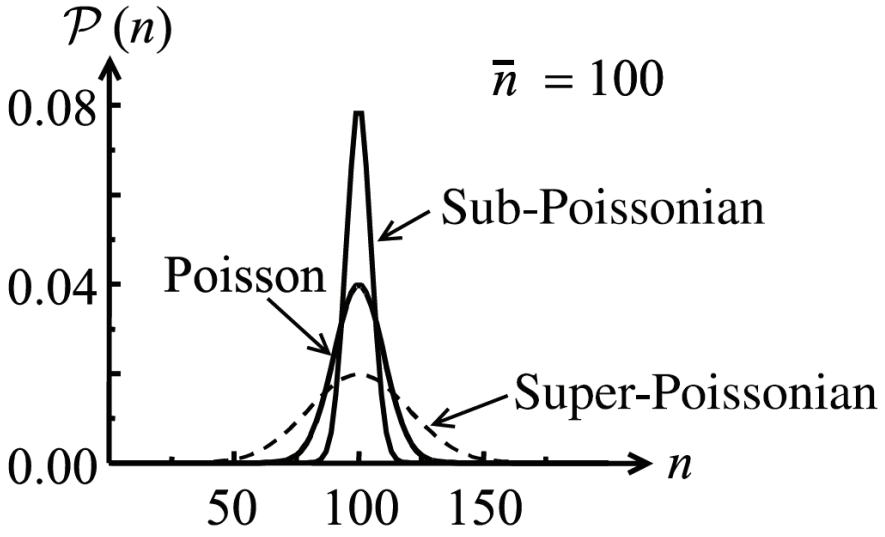

Figure 1.6. Photon statistics of light: super Poisson, Poisson and sub-Poisson (Fox, 2006)

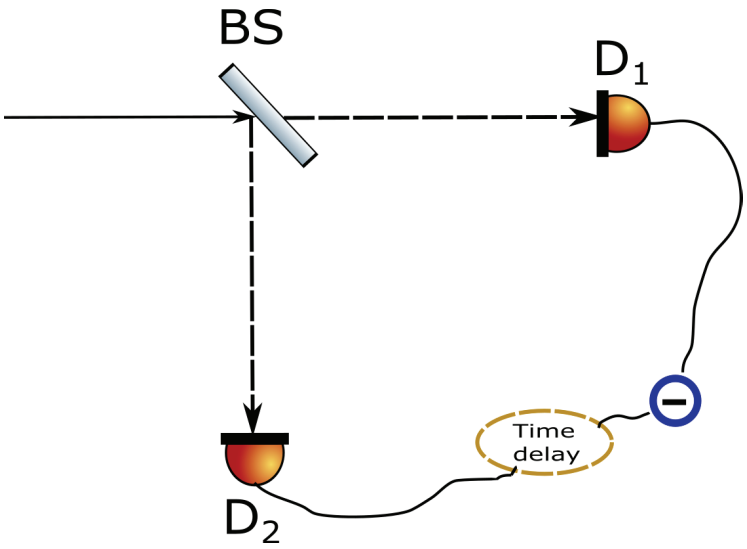

Figure 1.7. A second order correlation function $g^{(2)}(\tau)$ measurement setup

The determination of photon number, specifically through the photon counting process, primarily relies on quantum projective light intensity measurements within each detector integration period. This procedure can be conceptualized as an iterative approach involving multiple sequential measurements on an identical photon state, wherein the counting outcome signifies the photon number distribution of the light. From the semi-classical perspective, this outcome corresponds to the intensity distribution since photon number is proportional to the intensity of light (Mandel, 1958). Considering all-optical light source types, there are three main photon number distribution categories: super Poisson, Poisson, and sub-Poisson distribution, as given in Figure 1.6. Within the classical optics framework, a perfectly coherent beam characterized by a constant intensity stands as the pinnacle of stability. As such, it serves as a fundamental benchmark for categorizing diverse light sources and modalities by evaluating the standard deviation inherent in their photon number distributions. Therefore, the Poisson distribution constitutes a rudimentary model employed in the statistical inference of photon statistics (Sparavigna, 2021) since it represents the coherent light statistics. On the other hand, the thermal light reveals Bose-Einstein or super-Poisson distribution due to the large time-varying intensity fluctuations which corresponds that the variance (Δn) of the distribution is greater than the mean value ($\bar{n}$) (Fox, 2006). However, on the contrary to thermal distribution, sub-Poisson statistics has very narrow variance value which indicates that it is more stable and deterministic than perfectly coherent light due to having regular time arrivals between photons (Paul, 1982). In the literature, sub-Poisson distribution is regarded as the clear signature of the quantum nature of light which has no direct classical counterpart. To

extract accurate and reliable photon counting information by avoiding classical results and treatments due to the time averaging, the integration time of the detector should be shorter than the coherence time of the light (Mandel, 1958). Otherwise, the distribution approximate Poisson distribution regardless of the utilized light source.

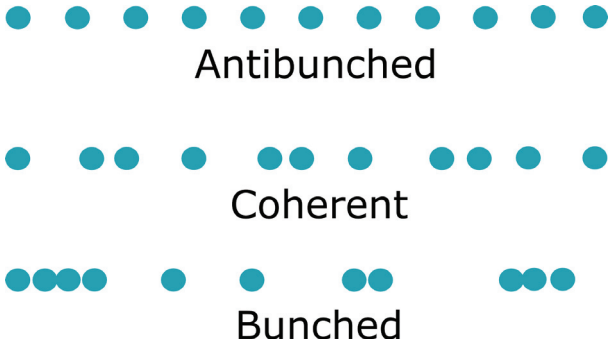

Figure 1.8. Illustration of photon time arrivals for antibunched, coherent and bunched light

Another approach for the extraction of light source characteristics is based on the realization of second-order coherence function $g^{(2)}(\tau)$ measurements, in addition to the threefold classification of light depending on whether the statistics are sub-Poissonian, Poissonian, or super-Poissonian. The approach is implemented with two detectors by evaluating the time delay between optical paths of photons. In the literature, this two-fold or joint detection scheme is usually called as coincidence detection. A basic scheme for coincidence detection is given in Figure 1.7. The main reason of this measurement type is about that first-order correlation function does not completely reflect the statistical properties of light (Ekici, 2021). By evaluating $g^{(2)}(\tau)$, the light is described as antibunched, coherent, or bunched. In the case of antibunched light, photons are emitted with consistent intervals between them, as opposed to random spacing. (Leuchs et al., 2015). On the other hand, in thermal light sources, photons move together in groups, forming bunches that result in high fluctuations in photon number or intensity (Morgan and Mandel, 1966). As in photon counting experiments, exposure time of the detector is highly significant. Otherwise, fluctuations in photon number disappear, causing the $g^{(2)}(\tau)$ to converge towards one.

In $g^{(2)}(\tau)$ classification, the value of $g^{(2)}(\tau)$ is evaluated and we encounter scenarios in which photons disperse at consistent temporal intervals or aggregate into bunches. The light is considered as coherent light when $g^{(2)}(0)$ equals one since there are ran-

dom time arrivals between photons. If $g^{(2)}(0)$ is greater than one, the source is defined as thermal or bunched light due to the fact that it comprises a photon stream characterized by bunched photon formations. Actually, it means that upon detecting a photon at time $t = 0$, there is an elevated likelihood of detecting another photon in close temporal proximity compared to more extended time intervals. Therefore, the bunches of photons coincide with high-intensity fluctuations. Lastly, the case $g^{(2)}(0) < 1$ is corresponds to the non-classical source where it is called as anti-bunched light. There is a sharp dip is observed in the $g^{(2)}(\tau)$ graph (see Figure 1.9). In the antibunched light, there is a well-defined spacing between photons. Bunched and coherent light align with classical results, unlike anti-bunched light, which lacks a classical counterpart and is thus a purely quantum optical phenomenon. An illustration of three optical sources in terms of the photons streams and their characterizations according to the second-order correlation function are given in Figure 1.8 and Table 1.1, respectively.

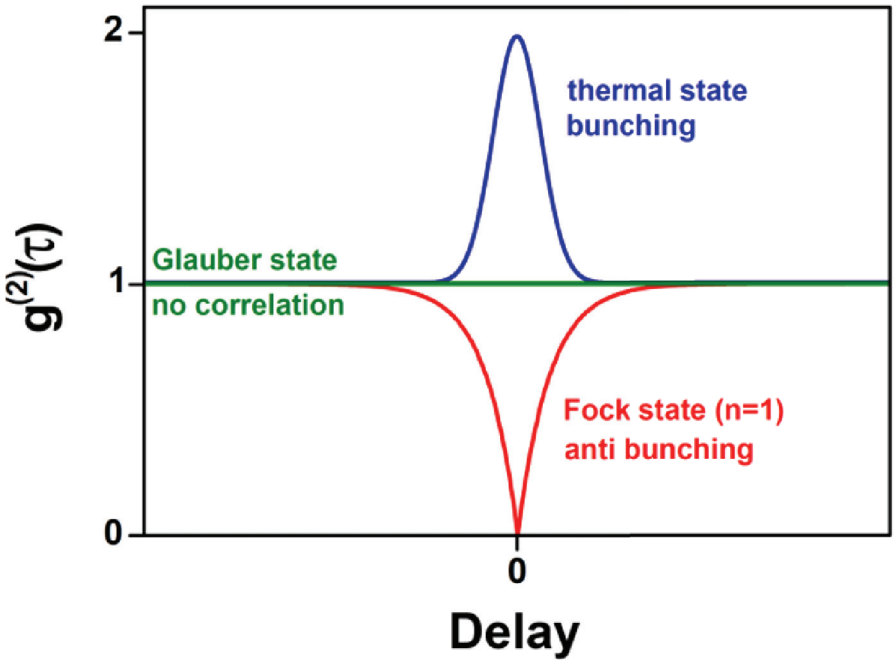

Figure 1.9. Second order correlation function $g^{(2)}(\tau)$ for three different light sources

Table 1.1. Characterization of light sources according to the second-order coherence function

Source type	**Photon stream**	$g^{(2)}(0)$
Thermal source	Bunched	>1
Coherent source	Random	=1
Non-classical source	Anti-bunched	<1

1.5. Photoelectric Detection of Light

The interaction between light and matter exhibits inherent randomness or stochastic behavior. Therefore, any attempt to measure light entails inevitable fluctuations. These fluctuations are ascribed to quantum phenomena, wherein light undergoes absorption solely in discrete units of energy, commonly referred to as quanta. The most elemental strategy for explaining these phenomena requires an investigation of the principles encapsulated within the framework of quantum electrodynamics (QED) (Bromberg, 2016). Hence, the quantization of electromagnetic fields becomes imperative, and the consequences of foundational postulates in quantum mechanics are to be scrutinized within the framework of the detection problem. While fundamentally essential, this methodology presents a challenge, demanding a comprehensive knowledge of quantum mechanics mathematics and relying minimally on physical intuition.

Semi-classical theory of photodetection, the light is classically but the photoelectric effect in the detector is quantized, is useful formalism to mitigate rigorous quantum mechanical approach and offers the advantage of relative simplicity in terms of requisite mathematical prerequisites, while also affording a more extensive application of physical intuition (Goodman, 2015). The primary advantage of this approach is its ability to establish the photon number-intensity relationship from a classical perspective (Straka et al., 2018). In the literature, it has been demonstrated that the projections of the semi-classical theory align entirely with those of the more rigorous quantum mechanical methodology in addressing all detection issues associated with the photoelectric effect (Mandel et al., 1964). Given that a significant majority of optical detection problems are grounded in the photoelectric effect, the initial assumption incurs relatively minimal sacrifice of generality and semi-classical theory provide it. A basic scheme for the photo-detection of light is given in Figure 1.10. It is assumed that the input light is very faint due to the quantum efficiency of conventional photon detectors (Mandel and Wolf, 1995). The in-

put field interacts with atoms in the photo-cathode, causing the photoelectric effect and freeing individual electrons. These electrons, in turn, trigger the release of more electrons in the electron multiplier region of the tube, generating a detectable current pulse. The counted pulses represent the release of individual electrons from the photo-cathode. Actually, the number of electrons reflects the photon number over the intensity values, created by photocurrents.

Although semi-classical approach is suitable for the light source characterization where the light has Poisson and super-Poisson distribution, it is impossible to extract sub-Poisson statistics which needs fully quantum mechanical treatment (Loudon, 2000). However, at this complicated situation, we encounter the requirement of a perfect and sophisticated laboratory environment problem to obtain accurate photon statistics because the random sampling nature of optical components (i.e., beam splitters) and low quantum efficiency, especially for single photon detection, ruin the original statistics of photons. Considering these necessary conditions, there is need for specific detectors having high quantum efficiencies. In addition, the detectors should have shorter integration time than the light source to provide meticulous statistical analysis due to the coherence problem of optical sources as we mentioned in previous section. Among the types of light sources, the coherent source have longer coherence time whereas thermal light sources generally have coherence time smaller than nanoseconds (Tan et al., 2014). If the detector's integration or exposure time is not adequate for photon statistics and optical coherence measurements, the results are indeed time average, which evolves Poisson distribution by deviating from the accurate form. This strongly indicates that the selection of detector plays a significant role in the observation of photon statistics and optical coherence in particular when the quantum efficiency and noise factors of the detector as well as the integration time issue are considered (Zambra et al., 2005; Boitier et al., 2009). Since commercially available CCD cameras usually have exposure time in the order of several tens of milliseconds and quantum efficiency at around %50, observing photon statistics with these devices a non-sophisticated laboratory environment remains a significant gap in the literature, is still challenging.

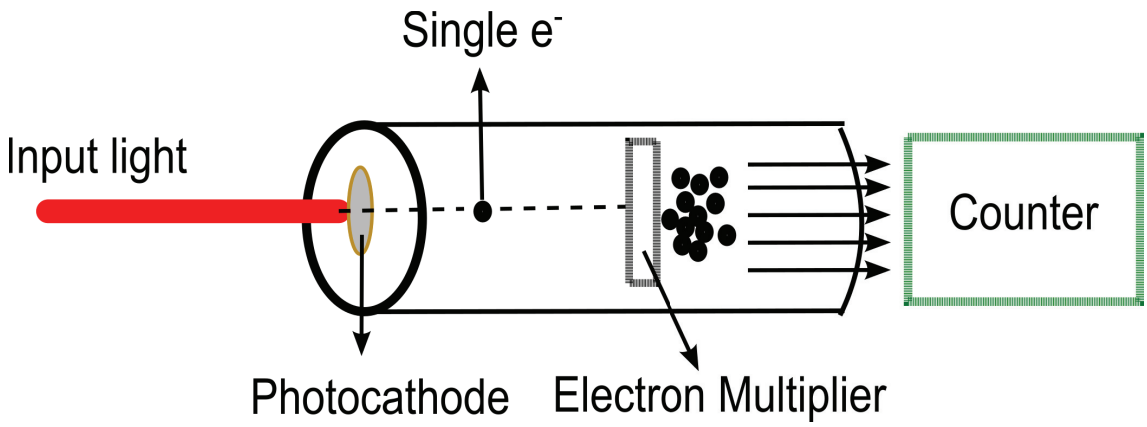

Figure 1.10. An illustration of the a single-photon counting PMT

1.6. Outline of the thesis

The outline of the remainder of the thesis chapters is presented here. The thesis structure follows logical order to enhance understanding of the basic work here.

Chapter 2 provides a theoretical background and mathematical preliminaries for quantum entanglement and two-photon diffraction. Comprehensive analysis of entangled photon pairs generation from SPDC and its impact on the system resolution is discussed analytically and in numerical simulations.

Quantifying light according to the photon statistics and second-order coherence function is given in Chapter 3. The photon distributions and antibunching phenomenon are explained in detail. The theory of photodetection from the semi-classical perspective is examined, including coincidence detection.

Chapter 4 presents a novel quantum-based approach for ultra-thin dielectric film characterization exploiting the phase diffraction of spatially entangled photons. The results demonstrate that the transverse spatial correlations significantly improve the accurate determination of film thickness. An alternative method utilizing thermal photon input is also investigated.

Chapter 5 proposes a practical measurement procedure for photon statistics and coherence measurements of thermal light beyond coherence time. The proof-of-concept experiments were conducted with measurements in the CCD pixels, proving the observation of bunching phenomenon on the ordinary detectors.

Chapter 6 focuses on concluding remarks and future directions.

CHAPTER 2

ENTANGLEMENT AND BIPHOTON DIFFRACTION

This chapter presents the theoretical background of the biphoton phase diffraction for quantum-based dielectric film thickness measurement setups and simulations. At first, we start with a fundamental introduction to the entangled state. Then, we examine the spontaneous parametric down-conversion (SPDC), the most common method to generate an entangled state, including the polarization effects through the process. After delineating a brief quantum detection process with optical coherence, we demonstrate the impact of spatially entangled photon diffraction on the resolution limit by verifying it with analytical models and simulations.

2.1. Quantum Entangled Photons

One of the most surprising consequences of quantum mechanics is the quantum entanglement effect, which describes the strong connection that forms between two or more particles that are located at different locations in space. It was proposed first as a gedanken experiment by Einstein−Podolsky−Rosen (EPR) in the seminal paper (Einstein et al., 1935). The paper introduces an entangled two-particle system based on the superposition of two-particle wave-function. Two main assumptions, locality and reality, was made by EPR. The locality claim that objects are only influenced by their immediate surroundings. And the reality means that if we can predict a measurement's outcome with certainty before the measurement, then that outcome doesn't depend on the choice of measurement technique.

In the theoretical framework, within a maximally entangled bipartite system, the determination of an observable (be it associated with space-time or spin) for an individual subsystem is indeterminate. However, upon measuring a specific value for such an observable in one subsystem, the corresponding value for the other subsystem becomes unequivocally fixed, irrespective of the spatial separation between the particles. This implies that while each subsystem may exhibit entirely random or all conceivable values for a given physical observable during its propagation, the non-local correlations between them become definitively established upon executing a joint measurement. From a mathe-

matical standpoint, the entanglement of two particles, denoted as particle one and particle two, manifests when their joint quantum state can not be factorized into the quantum states of the individual particles. An elementary representation of entangled state is (Einstein et al., 1935):

$$|\psi\rangle = \sum_{x,y} \delta(x + y - c_0) \, |x\rangle \, |y\rangle \tag{2.1}$$

where x and y are assumed as the momentum or the position of particle one and two, respectively, and c_0 is a constant. The physical interpretation of entanglement through the equation is that measuring a quantum observable on particle one affects the outcome of the same observable for particle two, and vice versa, by transcending the inter-particle distance and circumventing any need for manipulating particle two. This information, via non-factorability, can easily be extracted from the delta function.

Another traditional example of an entangled two-particle system, suggested by Bohm is a singlet state, refers to a system in which all electrons are paired, of two spin 1/2 particles:

$$|\psi\rangle = \frac{1}{\sqrt{2}}(|\uparrow\rangle_1 \, |\downarrow\rangle_2 - |\downarrow\rangle_1 \, |\uparrow\rangle_2) \tag{2.2}$$

where $|\uparrow\rangle$ and $|\downarrow\rangle$ represents spin-up and spin-down, respectively. At first sight from this equation, two options are absolutely indistinguishable with equal probabilities. This inference is the actual definition of superposition. Secondly, there is a sign between two parts of the entangled state where it could be minus or plus. It expresses the stable phase relation, in other words, correlation. The correlation term here actually implies the experimental evidence of coherence. Therefore, superposition and correlation in the wave-function are two inevitable terms that build up quantum entanglement.

Lastly, the most basic examples are four polarized Bell states (or EPR-Bohm-Bell states) which are a set of polarization states for a pair of entangled:

$$\phi^{\pm} = \frac{1}{\sqrt{2}}(|H\rangle_1 \, |H\rangle_2 \pm |V\rangle_1 \, |V\rangle_2) \tag{2.3}$$

$$\psi^{\pm} = \frac{1}{\sqrt{2}}(|H\rangle_1 \, |V\rangle_2 \pm |V\rangle_1 \, |H\rangle_2) \tag{2.4}$$

where $|H\rangle_i$ and $|V\rangle_i$ represent two orthogonal polarization bases.

2.2. Entangled Photon Generation

Spontaneous parametric down-conversion (SPDC) is a powerful and common method to generate entangled photon pairs. The term "spontaneous" indicates that the process occurs in the crystal spontaneously. Meanwhile, "parametric" highlights the conservation of total energy throughout the entire process. On the other hand, "down-conversion" refers that generated photons have lower frequency than the pump (Catalano, 2014). It is a $\chi^{(2)}$ non-linear optical phenomenon via the interaction of three waves (Di Giuseppe et al., 2002). The highly intense pump field is annihilated to generate signal (s) and idler (i) photons by conserving energy and momentum. The names of signal and idler are based on a historical story, likely attributable to the frequent use of non-degenerate processes in the early stages of SPDC experimentation. During this period, one radiation occupied the visible range (and was, therefore, easily detectable and visible, referred to as the "signal"), while the other existed in the infrared spectrum (generally escaping detection, thus labeled as the "idler") (Shih, 2003).

The limitations in SPDC arising from the principles of energy and momentum conservation, called as phase matching conditions, result in entanglement between the two down-converted photons across multiple degrees of freedom, encompassing aspects such as energy-time (Strekalov et al., 1996), position-momentum (Zhang et al., 2019), polarization (Shih, 1999), and angular position-orbital angular momentum (Rarity and Tapster, 1990). The generation probability of signal and idler photons depends on the phase matching function, and the efficiency is maximum during the perfect phase matching. Figure 2.1 illustrates the energy-level diagram of the SPDC process, wherein the absorption of a photon at frequency ω_p leads to the transition of the absorber to a virtual state. Subsequently, it undergoes decay to the ground state, emitting photons at two distinct frequencies ω_s and ω_i, respectively.

$$\omega_p = \omega_s + \omega_i \tag{2.5}$$

$$\vec{k_p} = \vec{k_s} + \vec{k_i} \tag{2.6}$$

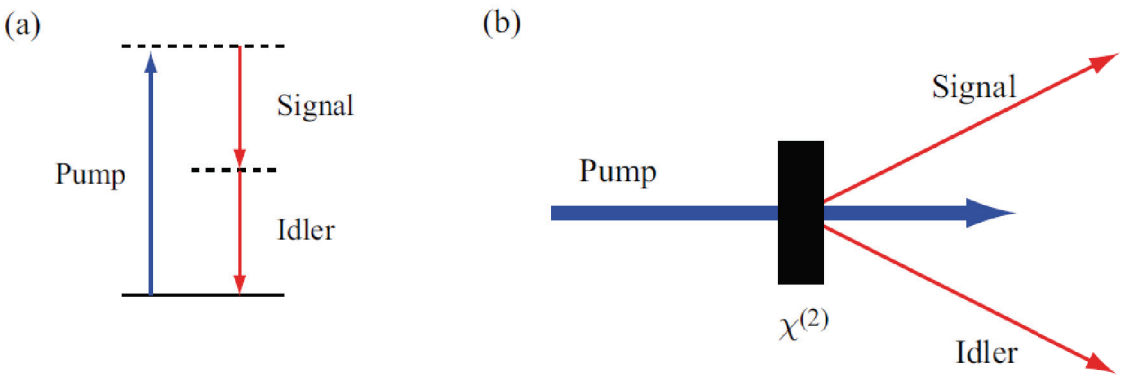

Figure 2.1. Nonlinear optical process of SPDC: (a) Energy level diagrams of SPDC (b) Down-conversion process through second-order nonlinear crystal (Jha, 2009)

2.2.1. Biphoton State of SPDC

To define the process step-by-step, we start with Maxwell equations since they provides information about the behavior of electromagnetic field in a medium deprived of free charges and currents:

$$\nabla \cdot \vec{D}(\vec{r},t) = 0 \tag{2.7}$$

$$\nabla \cdot \vec{B}(\vec{r},t) = 0 \tag{2.8}$$

$$\nabla \times \vec{E}(\vec{r},t) = -\frac{\partial \vec{B}(\vec{r},t)}{\partial t} \tag{2.9}$$

$$\nabla \times \vec{H}(\vec{r},t) = -\frac{\partial \vec{D}(\vec{r},t)}{\partial t} \tag{2.10}$$

Here, we focus on the medium that is assumed magnetically isotropic but electrically anisotropic. The electric displacement vector inside the medium:

$$\vec{D}(\vec{r},t) = \epsilon_0 \vec{E}(\vec{r},t) + \vec{P}(\vec{r},t) \tag{2.11}$$

where $\vec{P}(\vec{r},t)$ is polarization vector. When the pump field is highly intense, the polarization field is expressed as a power series taking high order contributions:

$$\vec{P}(\vec{r},t) = \epsilon_0 \Big[\underbrace{\chi^{(1)}\vec{E}(\vec{r},t)}_{linear} + \underbrace{\chi^{(2)}\vec{E}^2(\vec{r},t) + \chi^{(3)}\vec{E}^3(\vec{r},t) + ...}_{non-linear} \Big] \tag{2.12}$$

To derive interaction Hamiltonian for SPDC, we start with the classical total energy density of electromagnetic field:

$$H_{EM} = \frac{1}{2}\int d^3r(\vec{D}(\vec{r},t)\cdot\vec{E}(\vec{r},t) + \vec{B}(\vec{r},t)\cdot\vec{H}(\vec{r},t)) \tag{2.13}$$

Since the nonlinear interaction beyond second order is considered here to not appreciably affect the polarization, the classical Hamiltonian for the electromagnetic field can be broken up into two terms, one linear, and one nonlinear:

$$H_{EM} = H_L + H_{NL} \tag{2.14}$$

where

$$\begin{aligned} H_{NL} &= \frac{1}{2}\int d^3\vec{r}\vec{D}(\vec{r},t)\cdot\vec{E}(\vec{r},t) \\ &= \frac{1}{2}\epsilon_0\int d^3\vec{r}\chi^{(2)}(\vec{r};\omega(\vec{k_p}),\omega(\vec{k_s}),\omega(\vec{k_i}))\vec{E}_i(\vec{r},t)\vec{E}_j(\vec{r},t)\vec{E}_k(\vec{r},t) \end{aligned} \tag{2.15}$$

where Einstein notation is used for representation of pump, signal and idler. Now, we need to make transition from the classical representation to quantum representation. To make this, electric field functions $\vec{E}(\vec{r},t)$ are replaced by the field observables $\hat{E}(\vec{r},t)$ which can be defined as:

$$\hat{E}^+(\vec{r},t) = \frac{1}{V^{1/2}}\sum_{\vec{k},s} i\sqrt{\frac{\hbar\omega(\vec{k})}{2\epsilon_0}}\hat{a}_{\vec{k},s}(t)\vec{\epsilon}_{\vec{k},s}e^{i\vec{k}\cdot\vec{r}} \tag{2.16}$$

where s, ϵ and $\hat{a}_{\vec{k},s}(t)$ represent component of polarization, unit polarization vector and photon annihilation operator, respectively. Then, quantum Hamiltonian of electromagnetic field becomes:

$$\hat{H} = H_L + \frac{1}{2}\epsilon_0 \int d^3\vec{r}\Big(- \frac{1}{V}\sum_{\vec{k}_s,s}\sum_{\vec{k}_i,s} \chi^{(2)}(\vec{r};\omega(\vec{k_p}),\omega(\vec{k_s}),\omega(\vec{k_i})) \\ \times \sqrt{\frac{\hbar\omega(\vec{k_s})\omega(\vec{k_i})}{4\epsilon_0^2}} e^{-i(\vec{k}_s+\vec{k}_i)\cdot\vec{r}} E_i(\vec{r},t)\hat{a}^\dagger_{\vec{k}_s,s}(t)\hat{a}^\dagger_{\vec{k}_i,i}(t)\vec{\epsilon}_{\vec{k}_s,s}\vec{\epsilon}_{\vec{k}_i,i} + h.c.\Big) \quad (2.17)$$

In the equation above, we take the pump field classically since the pump field is usually several orders of magnitude larger than signal and idler fields. If we define the pump field in terms of plane waves:

$$E_i(\vec{r},t) = \frac{1}{2\pi}\int d^2\vec{q}_p \underbrace{E_i(\vec{q}_p,t)\vec{\epsilon}_{\vec{k}_p}}_{\tilde{E}_i(\vec{q}_p,t)} e^{i(\vec{q}_p\cdot\vec{r})} e^{i(k_{pz}z-\omega_p t)} \quad (2.18)$$

Then, Hamiltonian becomes:

$$\hat{H} = \hat{H}_L + \frac{1}{4\pi}\epsilon_0 \int d^3\vec{r}d^2\vec{q}_p\Big(- \frac{1}{V}\sum_{\vec{k}_s,s}\sum_{\vec{k}_i,s} \chi^{(2)}(\vec{r};\omega(\vec{k_p}),\omega(\vec{k_s}),\omega(\vec{k_i}))\sqrt{\frac{\hbar\omega(\vec{k_s})\omega(\vec{k_i})}{4\epsilon_0^2}} \\ \times e^{-i(\vec{q}_s+\vec{q}_i-\vec{q}_p)\cdot\vec{r}} e^{-i(k_{sz}+k_{iz}-k_{pz})} e^{-i\omega_p t}\tilde{E}_i(\vec{q}_p,t)\hat{a}^\dagger_{\vec{k}_s,s}(t)\hat{a}^\dagger_{\vec{k}_i,i}(t)\vec{\epsilon}_{\vec{k}_s,s}\vec{\epsilon}_{\vec{k}_i,i}\vec{\epsilon}_{\vec{k}_p} + h.c.\Big) \quad (2.19)$$

Let us define $\Delta\vec{q} = \vec{q}_s + \vec{q}_i - \vec{q}_p$ and $\Delta k_z = k_{sz} + k_{iz} - k_{pz}$. If the crystal is rectangular with side lengths L_x, L_y and L_z and the crystal is isotropic (does not depend on $\vec{r}$), we can simplify our equation to:

$$\hat{H} = \hat{H}_L + \frac{1}{4\pi}\epsilon_0 \int d^2\vec{q}_p\Big(-\frac{L_xL_yL_z}{V}\sum_{\vec{k}_s,s}\sum_{\vec{k}_i,s} \chi^{(2)}(\vec{r};\omega(\vec{k_p}),\omega(\vec{k_s}),\omega(\vec{k_i}))\sqrt{\frac{\hbar\omega(\vec{k_s})\omega(\vec{k_i})}{4\epsilon_0^2}} \\ \times sinc\big(\frac{\Delta q_xL_x}{2}\big) sinc\big(\frac{\Delta q_yL_y}{2}\big) sinc\big(\frac{\Delta q_zL_z}{2}\big) e^{-i\omega_p t}\tilde{E}_i(\vec{q}_p,t)\hat{a}^\dagger_{\vec{k}_s,s}(t)\hat{a}^\dagger_{\vec{k}_i,i}(t)\vec{\epsilon}_{\vec{k}_s,s}\vec{\epsilon}_{\vec{k}_i,i}\vec{\epsilon}_{\vec{k}_p} + h.c.\Big) \quad (2.20)$$

At this point, we start to derive the state of the entangled photons generated by SPDC. We assume that the pump photon starts interacting with crystal at time t=0. The

state at that time is $|\psi(0)\rangle = |vac\rangle_s |vac\rangle_i$. The biphoton state evolves under interaction Hamiltonian H_{NL}:

$$|\psi(t)\rangle = e^{-\frac{i}{\hbar}\int_0^t \hat{H}_{NL}dt} |\psi(0)\rangle \tag{2.21}$$

Since the parametric interaction is assumed to be very weak weak, the state in Equation (2.21) can be approximated by the first two terms of perturbation expansion:

$$|\psi(t)\rangle \approx \left(1 - \frac{i}{\hbar}\int_0^t \hat{H}_{NL}dt'\right) |\psi(0)\rangle \tag{2.22}$$

We assume that polarizations of down-converted photons are fixed, so that we can neglect sums over s. With this, the sum over the components of the nonlinear susceptibility is proportional to the value $d_{eff} = \frac{1}{2}\chi^{(2)}$. Besides, since nonlinear crystal is much larger than the optical wavelengths the sums over k_s and k_i can be replaced by integrals:

$$\lim_{V\to\infty} \frac{1}{V}\sum_{\vec{k},s} = \frac{1}{(2\pi)^3}\sum_{s_s}\int d^3\vec{k}_s \tag{2.23}$$

Then, interaction Hamiltonian simplifies (Schneeloch and Howell, 2016):

$$H_{NL} = C_{NL}d_{eff}\iint d^3\vec{k}_s d^3\vec{k}_i \sqrt{\omega(\vec{k_s})\omega(\vec{k_i})}\int d^2\vec{q}_p \left[\prod_{m=1}^{3} sinc\left(\frac{\Delta k_m L_m}{2}\right)\right] \times \tilde{E}_i(\vec{q}_p, t)e^{i\Delta\omega t}a^\dagger(\vec{k}_s)a^\dagger(\vec{k}_i) \tag{2.24}$$

If we substitute in Equation (2.22), the down-converted field can be expressed as:

$$\begin{aligned}|\Psi\rangle &\approx C_0 |0_s\rangle |0_i\rangle \\ &+ C_1 \iint d^3\vec{k}_s d^3\vec{k}_i \Phi(\vec{k_s}, \vec{k_i})\sqrt{\omega(\vec{k_s})\omega(\vec{k_i})}e^{\frac{i\Delta\omega T}{2}} sinc\left(\frac{\Delta\omega T}{2}\right) a^\dagger(\vec{k}_s)a^\dagger(\vec{k}_i) |0_s\rangle |0_i\rangle\end{aligned} \tag{2.25}$$

where biphoton wavefunction (or phase-matching function) is:

$$\Phi(\vec{k_s}, \vec{k_i}) = \int d^2\vec{q}_p \left[\prod_{m=1}^{3} sinc\left(\frac{\Delta k_m L_m}{2}\right)\right] \upsilon(\vec{q}_p) \tag{2.26}$$

where $\upsilon(\vec{q_p})$ is normalized pump amplitude spectrum.

For the simplicity, there can be made some more assumptions. In this way not only the system models are simplified but also mathematical calculations become smoother especially considering analytic and numerical integrations. Therefore, if we assume the pump field to be plane and monochromatic, the crystal size is infinite and interaction time is infinite, the Hamiltonian in Equation (2.17) can be simplified and the state at the output of the crystal can be represented as (Shih, 2012):

$$|\Psi\rangle = A \int d^3\vec{k_s} d^3\vec{k_i} \delta(\omega_p - \omega_s - \omega_i) \delta(\vec{k_p} - \vec{k_s} - \vec{k_i}) \hat{a}^\dagger_{\vec{k_s},s}(t) \hat{a}^\dagger_{\vec{k_i},i} |0\rangle_s |0\rangle_i \tag{2.27}$$

2.2.2. Polarization Properties in SPDC

Determining the generation and emission directions of down-converted photons relies on constraints decided by the conservation of energy and momentum, commonly referred to as phase-matching conditions. When the propagation directions of the down-converted signal and idler photons align with that of the pump photon, it is termed collinear phase matching. Conversely, in non-collinear phase matching, the signal and idler photons propagate in directions not aligned with the pump photon. As seen from the Equation (2.25) and (2.26), the efficiency of SPDC is directly related with the phase matching function $\Phi(\vec{k_s}, \vec{k_i})$ where efficiency takes the maximum value under perfect phase matching condition. When the phase mismatch in $\Delta k_z \neq 0$ increases, the efficiency of SPDC decreases. Also, there is a classification for the values of down-converted photon's frequency where the degenerate case corresponds that the photons have equal wavelengths and the non-degenerate case corresponds that the photons have different wavelengths.

We start by identifying the different polarization scenarios that could satisfy the phase-matching condition. To analyze the polarization effects, we specifically focus on the collinear case. In this configuration, the phase matching constraint $\Delta k_z = 0$ requires the equation below (Powers and Haus, 2017):

$$\frac{n_{p\mu}(\omega_p)\omega_p}{c} = \frac{n_{s\mu}(\omega_s)\omega_s}{c} + \frac{n_{i\mu}(\omega_i)\omega_i}{c} \tag{2.28}$$

where mentioned earlier p, s, i, ω represents the pump, signal, idler and frequency, respectively. The sub-index μ implies two conditions. If the direction of polarization is perpendicular to the optic axis, it is ordinary polarized and $\mu = o$. However, it is called extraordinary polarized and $\mu = e$ when the direction of polarization is parallel to the optic axis. For this reason, $n_{pe}(\omega_p)$ represents the refractive index of extra-ordinary pump photon having frequency ω_p. Combining the Equation (2.28) with energy conservation constraint $\omega_p = \omega_s + \omega_i$, the equation becomes:

$$n_{p\mu} - n_{s\mu} = \frac{\omega_i}{\omega_p}(n_{i\mu} - n_{s\mu}) \tag{2.29}$$

As seen from the equation above, there can be different polarization scenarios for pump, signal and idler photons including the type of uniaxial crystal. However, only a few combinations are survived due to the phase matching constraints given in Table 2.1 (Karan et al., 2020).

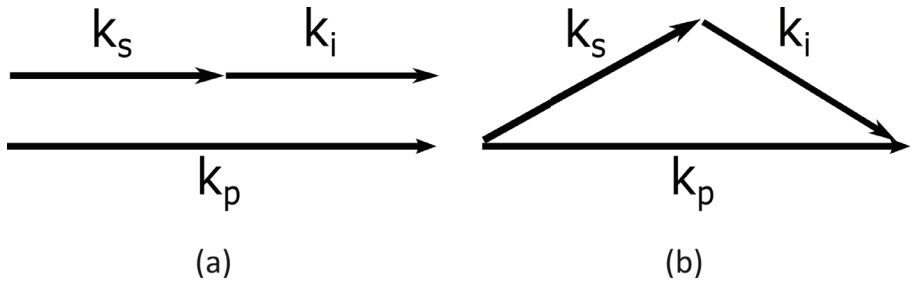

Figure 2.2. Perfect phase matching diagrams of SPDC for the cases: (a) collinear (b) non-collinear

Table 2.1. Polarization scenarios for signal and idler photons

Type	**Positive uniaxial crystal**	**Negative uniaxial crystal**
type-I	o→e+e	e→o+o
type-II	o→e+o o→o+e	e→o+e e→e+o

The general and common visualization for phase matchings is given in Figure 2.3. There are two rings, one for ordinary and the second for extraordinary. These pairs of photons coming on the opposite sides of laser beam due to the momentum conservation.

Their colours also represent the energy conservation. The overlap regions of the cones provide superposition (or indistinguishability of photons). For experimental procedures, SPDC has two fundamental categories, type-I and type-II, based on the abovementioned analyses (Briggs et al., 2021). In type-I SPDC, the photon pairs have the same polarization. For the degenerate emission, the photon pairs also have equal wavelengths emerge in a cone centering on the pump beam. On the other hand, in type-II SPDC, the photon pairs are orthogonally polarized and emitted into two cones (ordinary and extraordinary). For the degenerate collinear case, the photon pairs have equal wavelengths, and two cones are tangent to each other at one line at the pump beam direction, which means that the pump photon and the SPDC photon pair propagate together (parallel each other). This specialized case is obtained via tilting the of the non-linear crystal (Lee et al., 2016).

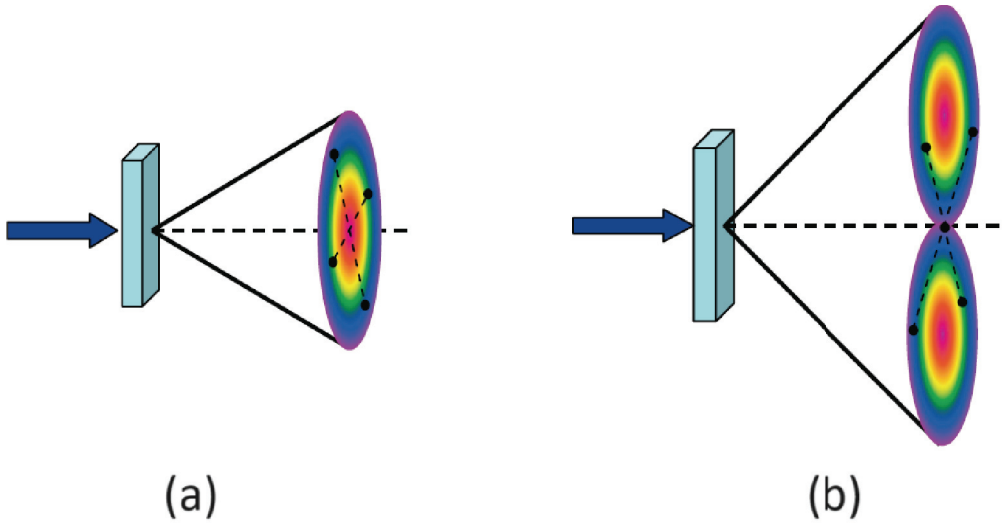

Figure 2.3. Phase matching outputs of SPDC (a) type-I (b) collinear degenerate type-II

2.3. Quantum Theory of Optical Coherence

In quantum field theory, positive frequency part of electric field operator $\hat{E}^{+}(\vec{r}t)$ is called as photon annihilation operator and negative part $\hat{E}^{-}(\vec{r}t)$ is called as photon creation operator. When the $\hat{E}^{+}(\vec{r}t)$ applied to an n photon state, it produces (n-1) photon state and its Hermitian adjoint $\hat{E}^{-}(\vec{r}t)$ produces (n+1) photon state. The further applications of annihilation operator reduce the number of photons until state in which the field is empty of all photons.

$$\hat{E}^{+}(\vec{r}t)\,|vac\rangle = 0 \tag{2.30}$$

$$\langle vac|\,\hat{E}^{-}(\vec{r}t) = 0 \tag{2.31}$$

In experiments, the detection process is corresponds to the absorption process which means that the field we are measuring is the one associated with photon annihilation, the complex field $\hat{E}^{+}(\vec{r}t)$. To express absorption process, we need to define the concept of probability amplitude which represents the transition of photon to the initial state $|i\rangle$ to a final state $|f\rangle$ as:

$$\langle f|\,\hat{E}^{+}(\vec{r}t)\,|i\rangle \tag{2.32}$$

For an ideal photon detector (assuming negligible size) which has a frequency-independent photo-absorption probability, the rate at which it records photons is proportional to the sum over all final states $|f\rangle$ of the squared absolute values of the Equation (2.32). In other words, the probability per unit time that a photon be absorbed by an ideal detector at point $\vec{r}$ at time t is proportional to (Stöhr, 2019):

$$\sum_{f} |\,\langle f|\,\hat{E}^{+}(\vec{r}t)\,|i\rangle\,|^{2} = \sum_{f} \langle i|\,\hat{E}^{-}(\vec{r}t)\,\underbrace{|f\rangle\,\langle f|}_{\mathbb{I}}\,\hat{E}^{+}(\vec{r}t)\,|i\rangle = \langle i|\,\hat{E}^{-}(\vec{r}t)\hat{E}^{+}(\vec{r}t)\,|i\rangle \tag{2.33}$$

where $\mathbb{I}$ is identity operator. In the quantum-based perspective, the result is crucial to note that such a detector for quanta corresponds to the the mean value of the product $\hat{E}^{-}(\vec{r}t)\hat{E}^{+}(\vec{r}t)$, and not the square of the real field $\hat{E}(\vec{r}t)$ (Glauber, 1963).

Capturing photon intensities using a single photon detector does not fully encompass the spectrum of measurements feasible for the field. However, it fundamentally delineates the majority of traditional optical experiments. Therefore, a second type of measurement, called as coincidence detection, we may make consists of the use of two detectors situated at different points r (for signal) and r' (for idler) to detect photon coincidences. Then, this transition takes the form (Shih, 2020):

$$\sum_f |\langle f|\hat{E}^+(\vec{r}'t')\hat{E}^+(\vec{r}t\,|i\rangle\,|^2 = \sum_f \langle i|\hat{E}^-(\vec{r}t)\hat{E}^-(\vec{r}'t')\,|f\rangle\,\langle f|\hat{E}^+(\vec{r}'t')\hat{E}^+(\vec{r}t\,|i\rangle$$
$$= \langle i|\hat{E}^-(\vec{r}t)\hat{E}^-(\vec{r}'t')\hat{E}^+(\vec{r}'t')\hat{E}^+(\vec{r}t\,|i\rangle \quad (2.34)$$

The interpretation of Equation (2.34) is the probability that one photon recorded at $\vec{r}$ at time t and another at $\vec{r}'$ at time t'. When it expands to the N-fold coincidence of photons for arbitrary N for the difficult elaborate experiments. The total rate for such coincidences will be proportional to:

$$\sum_f |\langle f|\hat{E}^+(\vec{r}'t')\hat{E}^+(\vec{r}t\,|i\rangle\,|^2 = \langle i|\hat{E}^-(\vec{r_1}t_1)...\hat{E}^-(\vec{r_n}t_n)\hat{E}^+(\vec{r_n}t_n)...\hat{E}^+(\vec{r_1}t_1\,|i\rangle \quad (2.35)$$

2.4. Two-Photon Diffraction

The generalized diffraction geometry for signal (or idler) is given in Figure 2.4. Each photon pairs are correlated in itself but mimic classical independent point sources between each other (Saleh et al., 2000). The signal (or idler) photon can be born at any position on the source (point B), propagates through the optical path r_{BX}, and is annihilated at point X on the detector plane where $\vec{r}$ and $\vec{\rho}$ represent the transverse position vector on the source and detector planes, respectively. All biphoton probability amplitudes are superposed on the detector plane after propagation.

In our model, the configuration assumes that the entangled photons are produced by degenerate collinear type-II SPDC ($\omega_s = \omega_i = \omega_p/2 = \omega$). The signal and idler photons are born at the same position, and their propagation angles are close to zero with respect to the pump direction (k_{pz}). The critical point is that we obtain entanglement (see Equation (2.27)) in both in space and polarization with the help this phase matching type (Shih and Sergienko, 1994).

The joint-detection probability $G^{(2)}$ between two points at the output of the source can be measured using two photon-counting detectors (D_1 and D_2). According to central theorem of quantum optics Glauber theory of photodetection and optical coherence, the joint-detection probability at the detectors between D_1 (at point ρ_s) and D_2 (at point ρ_i)

is expressed as (Glauber, 1963):

$$G^{(2)}(\vec{\rho}_s, z_s, t_s; \vec{\rho}_i, z_i, t_i) = \left| \left\langle 0|\hat{E}_i^{(+)}(\vec{\rho}_i, z_i, t_i)\hat{E}_s^{(+)}(\vec{\rho}_s, z_s, t_s)\right|\Psi\right\rangle \right|^2 = |\Phi(\vec{\rho}_s, z_s, t_s; \vec{\rho}_i, z_i, t_i)|^2 \tag{2.36}$$

where $\Phi(\vec{\rho}_s, z_s, t_s; \vec{\rho}_i, z_i, t_i)$ corresponds to the biphoton wavefunction.

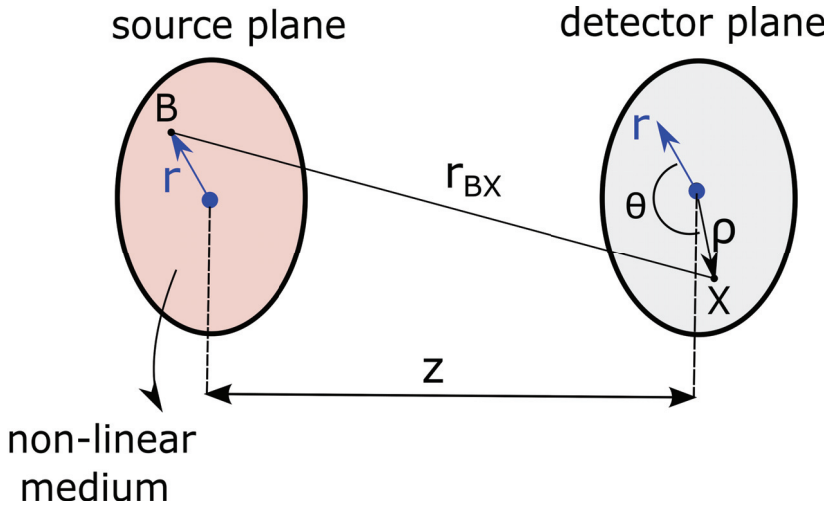

Figure 2.4. Diffraction geometry for spatially entangled photons from source plane to detector plane

The electric field operator of the system can be written in Fourier integral representation using optical transfer function $g(\vec{\kappa}_j, \omega_j; \vec{\rho_k}, z)$ as:

$$\hat{E}^+(\vec{\rho}_k, z, t_j) = \int d\vec{\kappa}_j d\omega_j g(\vec{\kappa}_j, \omega_j; \vec{\rho_k}, z)\hat{a}_j(\vec{\kappa}_j, \omega_j) \tag{2.37}$$

where ω_j, $\vec{\kappa}_j$ and $\hat{a}_j$ are the frequency, transverse wavevector, and annihilation operator of the signal and idler, respectively. According to the Huygens-Fresnel principle, the Fresnel propagator of the system (in Figure 2.4) for free space is:

$$g(\vec{\kappa}_j, \omega_j; \vec{\rho_k}, z) = \int_{aper} d\vec{r} \frac{A(\vec{r})}{r_{BX}} e^{i\vec{\kappa}_j \cdot \vec{r}} e^{-i\frac{\omega_j}{c} r_{BX}} \tag{2.38}$$

where $A(\vec{r})$ and $e^{i\vec{\kappa}_j \cdot \vec{r}}$ is aperture function and the phase factor associated with the each transverse wavevectors $\vec{\kappa}$ on source plane. Also $\vec{\rho_k}$ is the transverse coordinates on detectors where $k = 1$ for signal and $k = 2$ for idler due to the coincidence detection. The

optical path length r_{BX} is written using Fresnel approximation assuming r, $\rho \ll z$. We also assume $r_{BX} \approx z$ for magnitude part since it is less sensitive than phase.

$$r_{BX} = \sqrt{z^2 + |\vec{r_j} - \vec{\rho_k}|^2} \approx z\left(1 + \frac{|\vec{r_j} - \vec{\rho_k}|^2}{2z^2}\right) \approx z\left(1 + \cancel{\frac{r_j^2}{2z^2}} + \frac{\rho_k^2}{2z^2} - \frac{\vec{r_j} \cdot \vec{\rho_k}}{z^2}\right) \quad (2.39)$$

If the electric field operators for both signal and idler are substituted in Equation (2.36) using Equation (2.27) , the transverse part of the biphoton wavefunction is obtained as:

$$\begin{aligned}
\Phi(\vec{\rho_1}, z; \vec{\rho_2}, z) &= \left\langle 0 | \hat{E_i}^{(+)}(\vec{\rho_1}, z) \hat{E_s}^{(+)}(\vec{\rho_2}, z) \middle| \Psi \right\rangle \\
&= \langle 0 | \underbrace{C_1 \int d\vec{\kappa_s} \int_{aper} d\vec{r} \frac{A(\vec{r})}{z} e^{i\vec{\kappa_s}\cdot\vec{r}} e^{-i\frac{\omega_s}{cz}(\vec{r}\cdot\vec{\rho_1})} \hat{a}(\vec{\kappa_s}, \omega_s)}_{\hat{E_s}} \\
&\quad \times \underbrace{C_2 \int d\vec{\kappa_i} \int_{aper} d\vec{r'} \frac{A(\vec{r'})}{z} e^{i\vec{\kappa_i}\cdot\vec{r'}} e^{-i\frac{\omega_i}{cz}(\vec{r'}\cdot\vec{\rho_2})} \hat{a}(\vec{\kappa_i}, \omega_i)}_{\hat{E_i}} \\
&\quad \times \underbrace{C_0 \int d\vec{\kappa_s} d\vec{\kappa_i} \delta(\vec{\kappa_s} + \vec{\kappa_i}) \hat{a}^\dagger(\vec{\kappa_s}, \omega_s) \hat{a}^\dagger(\vec{\kappa_i}, \omega_i) |0, 0\rangle}_{|\Psi\rangle}
\end{aligned} \quad (2.40)$$

where C_0, C_1 and C_2 include phase factors and constants. Then, we can obtain:

$$\begin{aligned}
\Phi(\vec{\rho_1}, z; \vec{\rho_2}, z) = \Phi_0 \int_{aper} d\vec{r} A(\vec{r}) e^{-i\frac{\omega_s}{cz}(\vec{r}\cdot\vec{\rho_1})} \int_{aper} d\vec{r'} A(\vec{r'}) e^{-i\frac{\omega_i}{cz}(\vec{r'}\cdot\vec{\rho_2})} \\
\times \int d\vec{\kappa_s} d\vec{\kappa_i} \delta(\vec{\kappa_s} + \vec{\kappa_i}) e^{i(\vec{\kappa_s}\cdot\vec{r} + \vec{\kappa_i}\cdot\vec{r'})}
\end{aligned} \quad (2.41)$$

where Φ_0 includes all phase factor and constants. Assuming flat intensity distribution:

$$A(\vec{r}) = \begin{cases} 1, & \text{inside the slit} \\ 0, & \text{otherwise} \end{cases} \quad (2.42)$$

and since the last integral in Equation (2.41) yields $\delta(\vec{r} - \vec{r'})$, the wavefunction becomes:

$$\Phi(\vec{\rho_1}, z; \vec{\rho_2}, z) = \tilde{\Phi}_0 \int_{aper} d\vec{r} e^{-i\frac{\omega}{cz}(\vec{r}\cdot\vec{\rho_1}+\vec{r}\cdot\vec{\rho_2})} \tag{2.43}$$

where the joint detection probability is the absolute square of Equation (2.43). If the equation is examined for the circular aperture case using polar coordinates:

$$\int_0^R \int_0^{2\pi} r dr d\theta e^{-i\frac{\omega r}{cz}(\rho_1 \cos\theta_1 + \rho_2 \cos\theta_2)} = \frac{2J_1(\frac{R}{z}\frac{\omega}{c}|\vec{\rho_1} + \vec{\rho_2}|)}{\frac{R}{z}\frac{\omega}{c}|\vec{\rho_1} + \vec{\rho_2}|} \tag{2.44}$$

Since signal and idler photons fall at the same pixels on the detectors in the perfect spatial entanglement case, $\vec{\rho_1} = \vec{\rho_2} = \vec{\rho}$ is taken calculating diffraction pattern on the detector plane which corresponds two times narrower diffraction pattern comparing classical case as given in Figure 2.5.

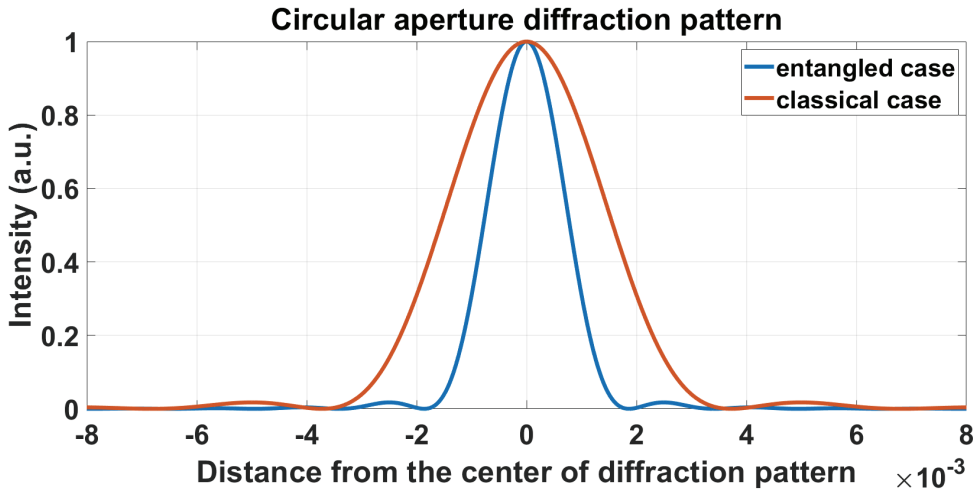

Figure 2.5. Diffraction profile of circular aperture for classical and spatially entangled case

CHAPTER 3

PHOTON STATISTICS AND PHOTODETECTION THEORY

This chapter briefly explain two fundamental perspectives photon statistics, and optical coherence, emphasizing their importance, especially for light source characterization. Since the theory of photodetection is essential to obtain accurate and precise statistical results, we tried to establish a bridge between them. The common and specific measurement technique, "coincidence detection," is also discussed with advantages and disadvantages by evaluating its suitability with detector requirements for various experiments.

3.1. Photon Counting Procedure

The measurement of photon statistics, namely the photon counting procedure, primarily hinges upon quantum projective measurements of light intensity conducted within each integration (or exposure) time of the detector. Since the distributions associated with photon numbers carry a significant wealth of information essential for characterizing the underlying physical processes or systems, photon counting can be defined as an important process in optics (Stevens, 2013; Kumazawa et al., 2019). It has large application areas from non-classical optical sources to quantum communication as mentioned in Section 1.4. A general photon counting setup configuration is given in Figure 3.1. It usually comprises an exceedingly sensitive light detector on the single photon level coupled to an electronic counting mechanism. The detector generates short voltage pulses, which are electron counts, in response to the incident field, while the counter records the quantity of emitted pulses within a defined temporal interval.

At first glance, the extraction of statistics may seem straightforward in that the detector's emission of electrons serves as conclusive evidence for the existence of discrete energy packets, or photons, in the incident light beam. As well, the fluctuations in the count rate are anticipated to provide insights into the statistical properties of the incoming photon stream. However, the argument is more complex than it appears. A longstanding question in optical physics pertains to whether the individual events recorded by pho-

ton counters are inherently connected to photon statistics or merely artefacts resulting from the complexities of the detection process (Koczyk et al., 1996). Therefore, there is needed to distinguish two fundamental but different perspectives: (1) the intrinsic photon statistics of the input light and (2) the statistical nature of the photodetection process. Therefore, it is clear that high-quality detectors are needed (Morton, 1968). Due to the sufficiency of the semi-classical approach in our proposed model, which provides simplicity, we generally use it to explain the photon counting process in the following, where the light is classical, but the photoelectric effect is quantized.

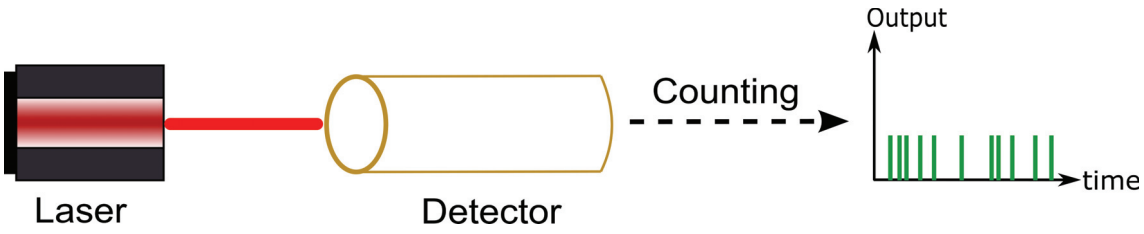

Figure 3.1. A coherent source photon counting scheme

The primary objective of the photon counting experiments is to quantify the photons incident upon the detector within a defined time interval. We start assuming that the incident beam consist of a stream of photons. The photon flux, denoted as Φ, is characterized as the mean quantity of photons traversing a cross-sectional area of the beam within a specified time unit as:

$$\Phi = \frac{IA}{\hbar\omega} = \frac{P}{\hbar\omega} \tag{3.1}$$

where A is the area of the beam and P is the power. Since the quantum efficiency is very important parameters for photon counting experiments due to the fact that it represents the ratio between the number of counts and number of incident photons, it is needed to taken into account. Therefore, the average number of counts ($N(\Delta t)$) is written as:

$$N(\Delta t) = \eta\Phi T \tag{3.2}$$

where average count rate $\mathcal{R}$ is:

$$\mathcal{R} = \frac{N}{\Delta t} = \eta\Phi = \frac{\eta P}{\hbar\omega} \quad counts\ s^{-1} \tag{3.3}$$

Considering that typical detectors have dead time at around 1 μs, the classical definition for upper limit is around 10^6 $counts$ s^{-1}. If the conventional quantum efficiency of detector is included to the calculations, other limit or requirement for photon counting process is working with very faint light (on the order of pW).

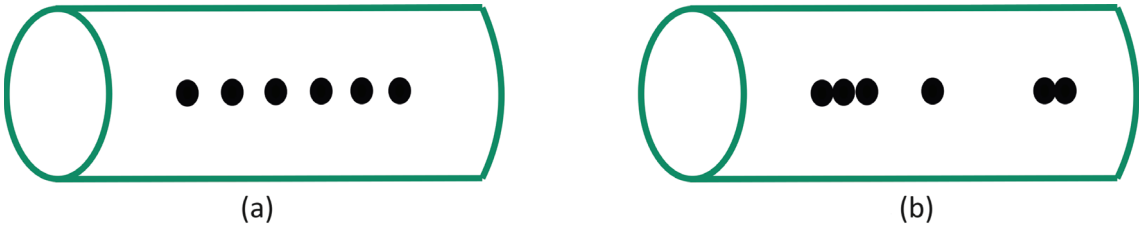

Figure 3.2. A section from an input beam containing fixed number of photons (a) equally spaced (b) non-equally spaced

In Figure 3.2, there are two illustrations of a beam with a fixed number of photons. The distribution of photons through the section varies, may be equally spaced or not, according to the type of incident field (e.g., thermal, coherent, or non-classical). By evaluating the number of photon distribution in each segment, the photon statistics are extracted. However, there is a need to be careful that the length of the segment directly affects and determines the obtained statistics. Since the length corresponds to the time interval, the analogy can be made between the time interval and exposure time of detectors. The effect of time interval is shown in 3.3. It is apparent that longer time intervals cause incorrect photon statistics due to the averaging, especially for optical sources with considerably lower coherence time. Therefore, the accurate detection of both photon statistics and optical fluctuations is not possible in optical systems with ordinary detectors with a long exposure time. Hence, the integration time of detectors is significant in extracting accurate and precise photon statistics and optical coherence analysis, which are two distinct perspectives for light source characterization.

If the same scenario is considered for a realistic detector case, the effect of detector's frame time is given in Figure 3.4. The sampling rate is in terms of 1/frame rate where one frame rate corresponds actual camera frame rate and two frame rate corresponds half

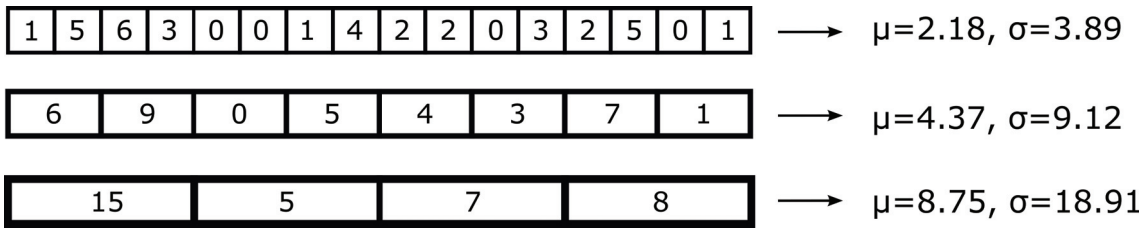

Figure 3.3. Illustration of the time interval effect on the mean (μ) and variance (σ) values

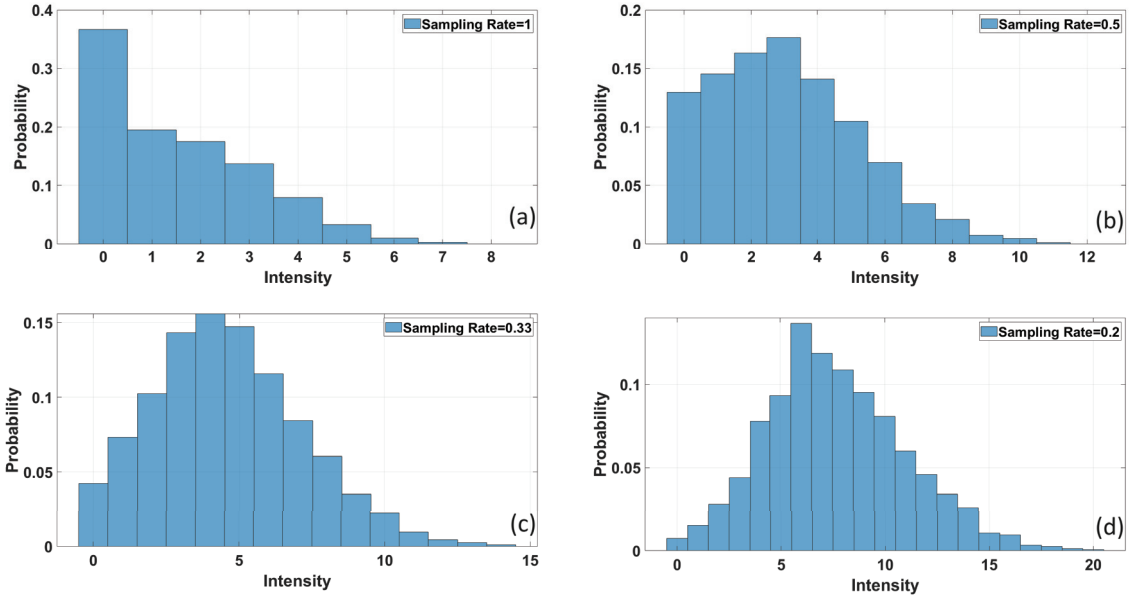

Figure 3.4. The convergence of Bose-Einstein distribution to the Poisson distribution due to the increasing frame time of the detector

of actual frame rate. It can be easily seen that when camera's exposure time increases, means poor quality, the distribution deviates from its accurate form and approximate to the Poisson distribution.

Furthermore, random sampling of the photons causes again incorrect information for photon statistics. This situation may arise for some reasons such as (1) due to inefficient detector collection, only a portion of the light emitted from the source is gathered, or (2) reductions in optical components occur as a result of absorption, scattering, or reflections from surfaces, or (3) the inefficiency in the detection process arises from the utilization of detectors with low quantum efficiency. The first situation involves stochastic photon selection from the source, the second entails random photon removal from the beam, and the third encompasses the random selection of a subset of photons for de-

tection. The first two problem result in degradation of photon statistics, while the third compromises the correlation between photon statistics and photo-electron statistics. Considering that extraction of photon statistics and optical coherence functions of quantum light sources is very sensitive and fragile, quality of detectors and avoiding from optical loss are crucial parameters (Chunnilall et al., 2014).

3.2. Photon Number Distributions

The field of quantum optics focuses on examining the consequences of treating light as a stream of photons rather than a classical wave. Although the distinctions between these perspectives are subtle, they require careful scrutiny to detect significant deviations from classical theories. In general, there are three main categories in the photon statistics approach: Poisson, super-Poissonian, and sub-Poissonian. Notably, the observation of Poisson and super-Poissonian statistics aligns with classical light theory, while sub-Poissonian statistics serve as a clear signature of the quantum nature or photon nature of light. However, they need to be examined in detail because the complexity of measurements and the need for suitable equipment vary significantly, such that sub-Poissonian light is highly susceptible to optical losses and inefficient detection methods.

In the photon statistics classification, the implementations are usually realized over the mean photon ($\bar{n}$) and variance $(\Delta n)^2$ values, especially with their ratios. The ratio between two parameters gives an insight about source characteristics such that large variance values are the strong indication of the bunching phenomenon due to the large fluctuations on the mean photon number. The summary of three fundamental light sourc category according to the $\bar{n}/(\Delta n)^2$ ratio is given Table 3.1. In the followings, we examine these classes in details.

Table 3.1. Characterization of light sources according to the photon number statistics

Source type	**Intensity**	$\bar{n}/(\Delta n)^2$
Incoherent, thermal or chaotic source	Fluctuated	>1
Coherent source	Constant	=1
Non-classical source	Constant	<1

3.2.1. Poisson Statistics

The Poisson distribution is a probability distribution utilized in the domains of probability theory, statistics, and physics. The discrete distribution quantifies the probability associated with a specific number of events. Employed as a modeling tool, the Poisson distribution serves to predict the frequency of events occurring within a given temporal or spatial interval. It has large application areas from photon counting experiments to modeling of nuclear decay of atoms (Hu, 2008). The distribution has some fundamental assumptions in the theory: (1) an event is described by integers; (2) the incidence of an event has no influence on the probability of a subsequent event, indicative of the independence of occurrences; (3) the average event rate remains independent of the unfolding of any particular occurrences.

In optics, Poissonian light sources are widely employed in fields such as photon counting, quantum optics experiments, and telecommunications, owing to their predictable and well-behaved statistical properties (Goodman, 2015). The classical and well-known example of a coherent light source is lasers. Since individual photons are emitted randomly (see Figure 3.5) from the laser's active medium, they exhibit Poissonian photon statistics. The experiments are realized in faint light condition. The reason is that as the intensity of the coherent light source increases, the statistical behavior of the detected photons becomes less Poissonian and more deterministic. The general representation of coherent light-wave photon statistics with constant intensity is (Saleh and Teich, 2019):

$$P(n) = \frac{\bar{n}^n}{n!} e^{-\bar{n}} \tag{3.4}$$

$$(\Delta n)^2 = \bar{n} \tag{3.5}$$

where n is the number of photons, $\bar{n}$ is the mean and $(\Delta n)^2$ is the variance in the count number.

In light sources exhibiting Poissonian behavior, the arrival of photons follows a statistical pattern in which the fluctuations in photon counts are directly related to the square root of the average photon count. This unique characteristic, specific to the Poisson distribution, implies that the timing and intensity of photon arrivals are statistically independent, maintaining a consistent average photon count over time.

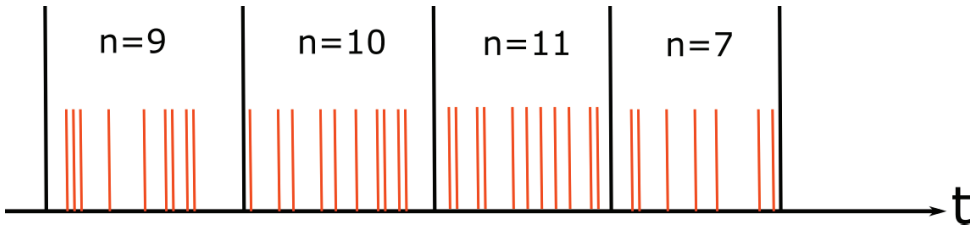

Figure 3.5. Illustration of random arrivals of photons from the coherent light source through the constant optical power. Each interval represents integration time of the detector.

3.2.2. Super-Poissonian Statistics

A light source that is governed by Super-Poissonian statistics has time-varying light intensities. It is characterized by photon statistics that deviate from the Poisson distribution, indicating correlations or fluctuations in photon arrival times with large $(\Delta n)^2/\bar{n}$. In practical terms, this means that in super-Poissonian light sources, such as electromagnetic radiation emitted by hot body, certain types of lasers or chaotic light-emitting systems, the photon count variance exceeds the average photon count, resulting in a greater degree of uncertainty in photon arrival times. A typical example of a light source with super-Poisson behavior is thermal light, a type of electromagnetic radiation emitted by a hot object. Considering the single mode thermal radiation, the probability that there will be n photons in the mode ω obeys the Bose-Einstein distribution given as (Saleh and Teich, 2019):

$$P_{\omega}(n) = \frac{1}{\bar{n}+1}\left(\frac{\bar{n}}{\bar{n}+1}\right)^{n} \tag{3.6}$$

$$(\Delta n)^2 = \bar{n} + \bar{n}^2 \tag{3.7}$$

where n is the number of photons, $\bar{n}$ is the mean and $(\Delta n)^2$ is the variance in the count number. It can be seen that $P_{\omega}(n)$ has the maximum number for $n = 0$ and decreases for larger n (see Figure 3.6). The critical point is that the Bose-Einstein distribution is valid for only single mode thermal field. When the number of modes in the input thermal field increases, the distribution start to deviate from Bose-Einstein. Considering that there are multi-mode fields in most studies, the general formula for the N_m thermal modes is:

$$(\Delta n)^2 = \bar{n} + \frac{\bar{n}^2}{N_m} \tag{3.8}$$

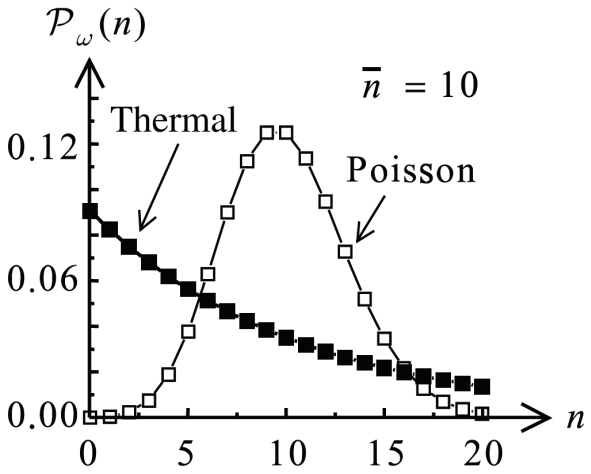

Figure 3.6. Photon statistics of light sources with Bose-Einstein and Poisson distributions (Fox, 2006)

The key feature of light sources exhibiting Bose-Einstein statistics is that photons arriving in bunches rather than having a deterministic or random. This effect called as photon bunching. When such a light beam hits a photodetector, more photon pairs are detected in close proximity to each other than at greater distances apart.

3.2.3. Sub-Poissonian Statistics

As we know from Section 1.4, sub-Poissonian light exhibits a photon number distribution narrower than that of Poisson statistics (see Figure 1.6). These light sources are called as antibunched light source which demonstrates greater stability compared to perfectly coherent light (Scully and Zubairy, 1997). Sub-Poissonian light lacks a classical equivalent and observation of sub-Poissonian statistics a distinct indicator of the quantum nature of light. The time intervals between photons are more regular than random time interval. In perfect or highly sub-Poisson case, the variance value is represented as $(\Delta n)^2 = 0$. This situation also called as photon number state. Furthermore, the photon count number is the same for each experiment and equals to the mean number. The photon number (N) of a beam in the time interval T would be the integer value determined by (Fox, 2006):

$$N = Int\left(\eta \frac{T}{\Delta t}\right) \tag{3.9}$$

which would be exactly the same for every measurement. Int represents the integer output of the equation. Since the result is interpreted as deterministic, the expectation is that the photon distribution should be delta function as given in Figure 3.7. Photon streams, having $\Delta n = 0$, is called as number or Fock state. These states are the purest form of sub-Poissonian light. The probability of $P(n)$ to find n_i photons in one mode is either one for $n = n_i$ and zero for $n \neq n_i$ which is the clear indication that photon number is fully determined. The quantum representation of Fock state is given as the eigenstate of the photon number operator n_i:

$$\hat{n_i} \left|n_i\right\rangle = n_i \left|n_i\right\rangle \tag{3.10}$$

where the eigenvalue n_i of the photon number operator describes the number of photons in a specific mode i. The light sources with Fock state $n = 1$ is called as single photon sources.

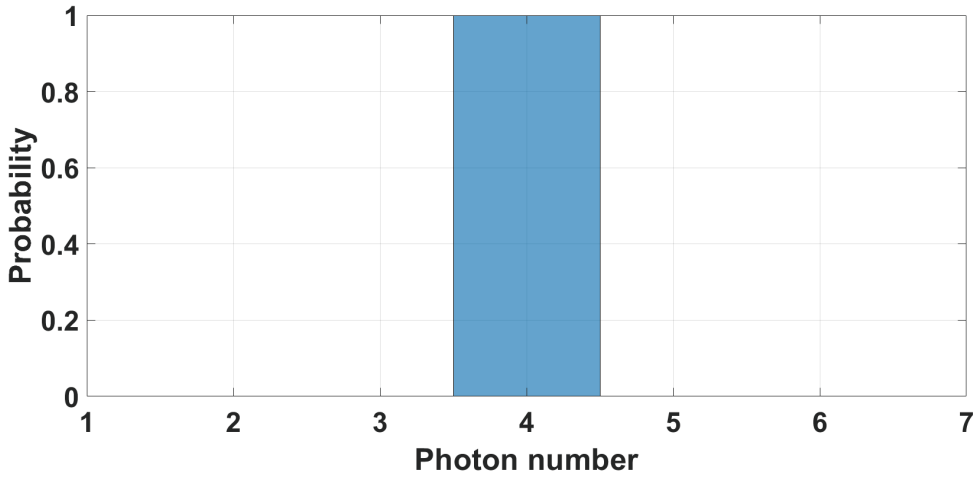

Figure 3.7. Photon number statistics of a sub-Poissonian light with $\bar{n}$=4

3.3. Semi-classical Theory of Photodetection

When light impinges upon specific metallic surfaces, it can cause the release of electrons, a phenomenon known as the photoelectric effect (Klassen, 2011). These emitted particles are referred to as photoelectrons. By placing a positively charged electrode near the photoemissive cathode to attract these photoelectrons, an electric current is generated in response to the incident light. This setup transforms the device into a photoelectric detector for the optical field, is a crucial instrument in photometry. Various methods are available to amplify the photoelectric current (Garrison and Chiao, 2008). One notable amplification device is the photomultiplier, illustrated schematically in Figure 3.8. The photoelectrons are accelerated sufficiently so that when they strike the positive electrode, they trigger the release of several secondary electrons for each incident primary electron. These secondary electrons, in turn, are accelerated to strike other surfaces with secondary emission capabilities. After more similar stages of amplification, each photoelectron emission from the aperture results in a pulse comprising millions of electrons at the anode. This pulse is substantial enough to be detected by an electronic counter. By calculating these photoelectric pulses, an experimental light detector is achieved.

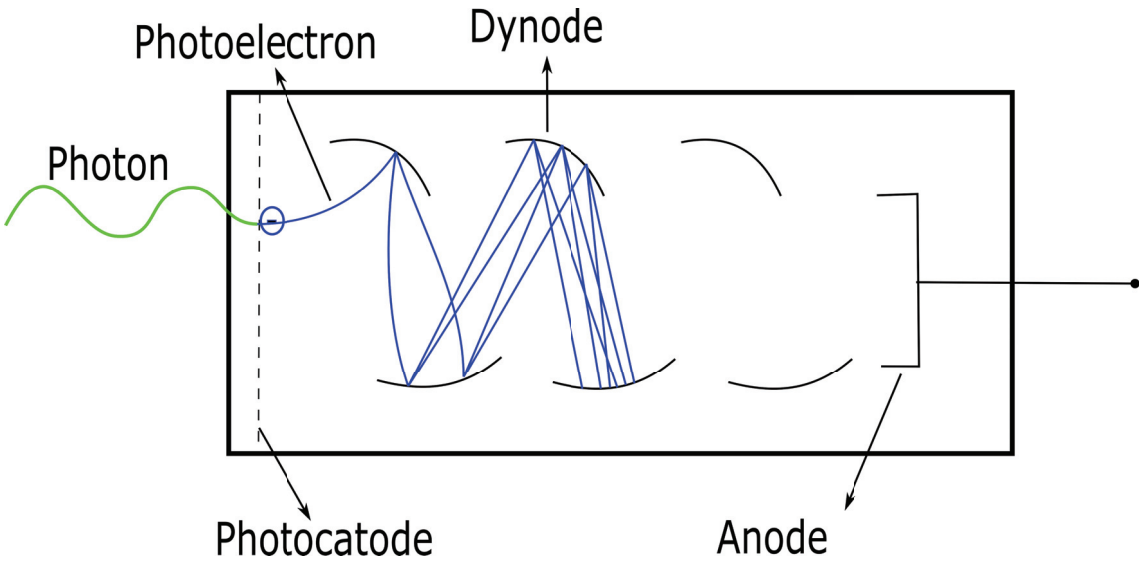

Figure 3.8. A photomultiplier tube scheme with secondary electron emissions

Experimental findings indicate that photoelectric emission from a specific surface occurs exclusively when the incident light's frequency surpasses a predefined threshold,

as illustrated in the accompanying Figure 3.9. Once this critical frequency is exceeded, the rate of photoelectron emission per unit time correlates proportional with the intensity of the incident light (Grynberg et al., 2010). Simultaneously, the average kinetic energy of the emitted photoelectrons remains unaffected by variations in light intensity. Comprehending this phenomenon proved challenging within the classical framework of physics. Einstein found it most plausible to explain if electrons within the metal were confined to a potential well with a minimum binding energy. In this conceptualization, light is considered to consist of discrete particles or photons (quantas) with an energy of $\hbar\omega$ at frequency ω. The photon flux is directly proportional to the light intensity or power flow. When a photon is absorbed at the photoelectric surface, it gives its energy to an electron. However, unless the photon energy $\hbar\omega$ exceeds a threshold value E_0, it is insufficient to release the electron.

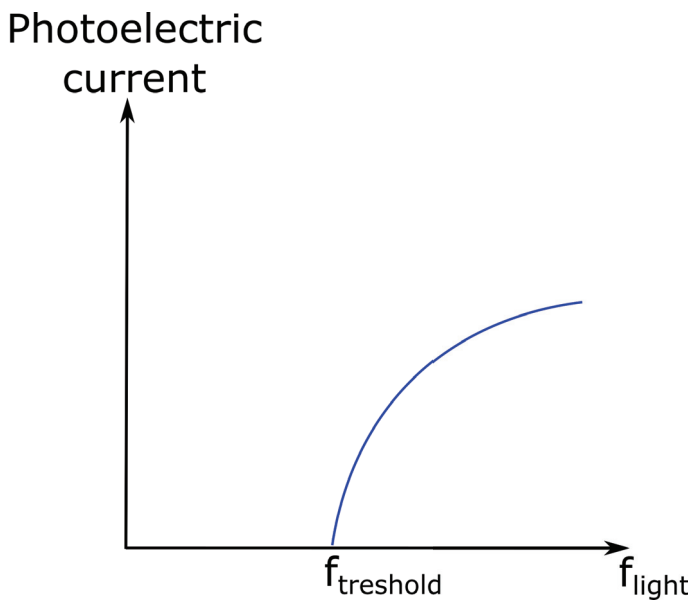

Figure 3.9. Characteristic of photoelectric emission

While the basic quantum model provided some insights into the photoelectric effect, a more comprehensive framework, encompassing quantum mechanics and quantum electrodynamics, was necessary for a detailed description and the derivation of probability expressions for photoelectric emission at different time instances. Although a fully quantized treatment represents the exact solution to this problem, for numerous applications, there is no imperative need to fully quantize the electromagnetic field. Instead, one can comprehend the photodetector's response by persisting with a classical electromagnetic

wave representation of the field as long as the photoelectrons are subjected to quantum mechanics. In this scenario, the field acts as an external potential, perturbing the bound electrons of the photocathode. This approach is termed the semi-classical approach, proving considerably more straightforward than the fully quantized treatment. Although it has some limitations under some circumstances (Shapiro, 2009), it is a practical and useful model for engineering applications. Therefore, we will investigate the photodetection theory mainly from a semi-classical perspective.

3.3.1. Photodetection Probability

In the semi-classical approximation, the photodetection probability $P(t)\Delta t$ is written as given in Equation (3.11) under some assumptions (Mandel and Wolf, 1995). These assumptions are that there are N-bound electrons on the illuminated photoelectric surface, the incident light in the form of a plane wave perpendicular to the photocathode, there is minimal depletion of bound states, and no significant mutual influence among different photoemissions.

$$P(t)\Delta t \sim \eta I(\vec{r}, t)\Delta t \tag{3.11}$$

where $\vec{r}$ is an arbitrary point on the photocathode surface and η is a constant characterizing the detector efficiency for a particular frequency and particular polarization. In this point, it should be noted that $P(t)\Delta t$ is differential probability, which means that we are interested in detections in one or more differential time intervals. This relation is only valid for $\eta I(\vec{r}, t)\Delta t \ll 1$ due to providing photon number-intensity proportionality. Even if the time interval is very small, the condition will not be met for high-intensity values since the perturbation can not be terminated at the lowest non-vanishing term due to the high order contributions. Therefore, we will exclude the option based high-intensity levels which is one of the reason that why photon statistics experiments are realized in very faint light condition. However, Equation (3.11) should be modified for realistic cases by considering the randomly fluctuating electromagnetic field. There is need to introduce a collection of realizations for the optical field which is ensemble averaging since physically significant results are derived only through the process of averaging across all members of the ensemble. If the ensemble is denoted by $\langle\rangle$, the differential photoelectric detection probability of a fluctuating field is rewritten as:

$$P_1(\vec{r},t)\Delta t = \eta\langle I(\vec{r},t)\rangle\Delta t \tag{3.12}$$

On the other hand, in terms of integral detection probability, the expected number $\mathcal{N}$ is written for the average number of photoelectric detections in a finite time interval from t to T is:

$$\langle\mathcal{N}\rangle = \eta\int_t^{t+T}\langle I(\vec{r},t^{'})\rangle dt^{'} \tag{3.13}$$

If the field exhibits stationary, the average of $I(\vec{r},t)$, naturally unaffected by the variable time t. Then, the equation above becomes:

$$\langle\mathcal{N}\rangle = \eta\langle I(\vec{r})\rangle T \tag{3.14}$$

which is proportional to T.

3.3.2. Multiple Photoelectric Detection and Correlations

After deriving the expression for the differential probability of a photoelectric detection occurring at a specific point and time, we can extend this to scenarios where multiple detections are recorded at different times and detectors. Therefore, let us consider the case that there are two photodetectors of quantum efficiencies α_1, α_2 with areas S_1, S_2 centered at points $\vec{r}_1$, $\vec{r}_2$ where we assume that the plane wave is normally incident due to the fact that each illuminated detectors are small enough, as given in Figure 3.10. We are interested in the joint detection probability $P_2(\vec{r}_1,t_1,\Delta t_1;\vec{r}_2,t_2,\Delta t_2)$ that photodetections will be registered by one detector at time t within Δt_1, and by the other detector at time t_2 within Δt_2, with $t_2 > t_1$.

We will assess the joint probability of detection in two stages. We first calculate the differential probability for first photodetection as:

$$P(\vec{r}_1,t_1,\Delta t_1) = \alpha_1 S_1 I(\vec{r}_1,t_1)\Delta t_1 \tag{3.15}$$

where $I(\vec{r}_1,t_1)$ is the light intensity or photon density at $\vec{r}_1$, t_1 in the coherent state.

Then, using this state to be initial state for the second measurement, calculate the probability for the second detection. The differential probability of second measurement is represented as:

$$P(\vec{r}_2, t_2, \Delta t_2) = \alpha_2 S_2 I(\vec{r}_2, t_2)\Delta t_2 \tag{3.16}$$

These probabilities are then multiplied together to yield $P_2(\vec{r}_1, t_1, \Delta t_1; \vec{r}_2, t_2, \Delta t_2)$:

$$P_2(\vec{r}_1, t_1, \Delta t_1; \vec{r}_2, t_2, \Delta t_2) = \alpha_1 S_1 I(\vec{r}_1, t_1)\Delta t_1 \alpha_2 S_2 I(\vec{r}_2, t_2)\Delta t_2 \tag{3.17}$$

where it is written in more general form as:

$$P_2(\vec{r}_1, t_1; \vec{r}_2, t_2) = \eta_1 \eta_2 \langle I(\vec{r}_1, t_1) I(\vec{r}_2, t_2)\rangle \tag{3.18}$$

It is noted that this probability involves intensity correlation function in the second order. In addition, for a fluctuating field,

$$\langle I(\vec{r}_1, t_1) I(\vec{r}_2, t_2)\rangle \neq \langle I(\vec{r}_1, t_1)\rangle \langle I(\vec{r}_2, t_2)\rangle \tag{3.19}$$

and so

$$P_2(\vec{r}_1, t_1; \vec{r}_2, t_2) \neq P_1(\vec{r}_1, t_1) P_1(\vec{r}_2, t_2) \tag{3.20}$$

where $P_1(\vec{r}, t)$ is the single probability density for photodetection. This implies that two photodetections at $\vec{r}_1$, t_1 and $\vec{r}_2$, t_2 are not independent but correlated. Although two photodetection events do not affect each other, they are correlated by the fluctuations of common electromagnetic waves. It can be explained as, in general, correlations between successive photoelectric pulses are to be expected. This is true even if one photoemission can not physically influence another one. The reason is that each photodetection yields information about the field that affects our estimate of the probability of another photodetection. We can express this in another way that invokes a more classical picture of the optical field by saying that intensity fluctuations cause the photodetections at two or more space-time points to be correlated.

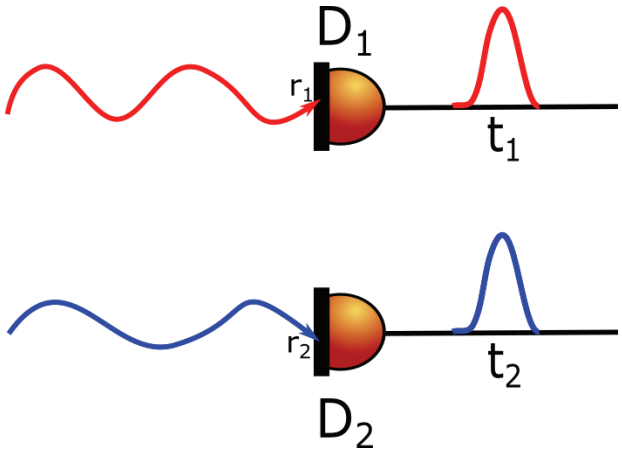

Figure 3.10. Multiple photodetection with two detectors

The normalized intensity correlation function $\lambda(\vec{r}_1, t_1; \vec{r}_2, t_2)$ can be express to define the degree of correlation as:

$$\lambda(\vec{r}_1, t_1; \vec{r}_2, t_2) \equiv \frac{\langle I(\vec{r}_1, t_1) I(\vec{r}_2, t_2)\rangle}{\langle I(\vec{r}_1, t_1)\rangle \langle I(\vec{r}_2, t_2)\rangle} - 1 \tag{3.21}$$

Then, we can re-express the joint detection probability in the form:

$$\begin{aligned} P_2(\vec{r}_1, t_1; \vec{r}_2, t_2)\Delta t_1 \Delta t_2 &= \alpha_1 S_1 \langle I(\vec{r}_1, t_1)\rangle \Delta t_1 \alpha_2 S_2 \langle I(\vec{r}_2, t_2)\rangle \Delta t_2 [1 + \lambda(\vec{r}_1, t_1; \vec{r}_2, t_2)] \\ &= P_1(\vec{r}_1, t_1)\Delta t_1 P_2(\vec{r}_2, t_2)\Delta t_2 [1 + \lambda(\vec{r}_1, t_1; \vec{r}_2, t_2)] \end{aligned} \tag{3.22}$$

The normalized correlation function $\lambda(\vec{r}_1, t_1; \vec{r}_2, t_2)$ provides a measure of the lack of statistical independence of the photoelectric pulses. Only for states of the field for which $\lambda = 0$ do the pulses become independent.

We can also say that the different photodetections need not necessarily refer to different detectors, but single photodetector can be used. In this case the quantum efficiencies and surface areas are necessarily equal and light intensities differ only in time arguments. This formula can be generalized for N-photodetection events by calculating the expectation:

$$P_N(\vec{r}_1, t_1, \Delta t_1; .....; \vec{r}_N, t_N, \Delta t_N) = \prod_{l=1}^{N} \alpha_l S_l \Delta t_l \langle I(\vec{r}_1, t_1) .... I(\vec{r}_N, t_N) \rangle$$
$$= \prod_{l=1}^{N} [\alpha_l S_l \Delta t_l] \Gamma^{(N,N)}(\vec{r}_1, t_1, .., \vec{r}_N, t_N; \vec{r}_N, t_N, .., \vec{r}_1, t_1) \tag{3.23}$$

A consequence arising from correlations is the occurrence of photoelectric bunching, wherein emissions from a photodetector are more likely to cluster together than to occur at distant time intervals. If we examine two detections at times t and $t + \tau$ by a single photodetector (omitting the position dependency $\vec{r}$ on the detector), two-fold photodetection probability is written as:

$$P_2(t, t + \tau) = \eta^2 \langle I(t) I(t + \tau) \rangle \tag{3.24}$$

As $\tau \to \infty$, it follows for an ergodic process that $\langle I(t) I(t + \tau) \rangle \to \langle I \rangle^2$, or (Mandel and Wolf, 1995)

$$P_2(t, t + \tau) \to P_1^2(t) \quad for \quad \tau \to \infty \tag{3.25}$$

so that the detections become independent when they are far separated in time.

A graphical representation illustrating the joint probability density, denoted as $P_2(t, t + \tau)$, for photoelectric detection against the time interval τ, as depicted in Figure 3.11. The highest value of $P_2(t, t + \tau)$ is observed at zero separation distance τ, gradually diminishing to the constant value $P_1^2(t)$ for larger τ. This phenomenon manifests exclusively in fluctuating fields, particularly those generated by thermal sources as given in section 3.2.2. The observed effect has been linked to the bosonic nature of thermal photons, which exhibit a tendency to bunch. Since the light field is defined as an electromagnetic wave in our case, the bunching effect is observed over the light intensity fluctuations. For examining non-classical sources, antibunching case, the semi-classical approach is not adequate.

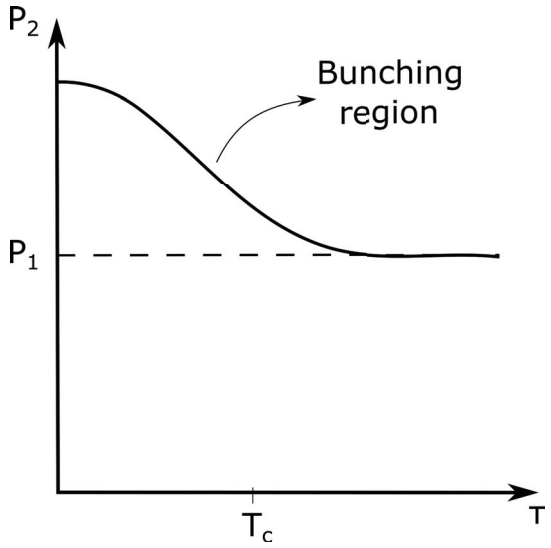

Figure 3.11. Expected joint detection probability for photodetection at two different times as a function of time difference τ

3.3.3. Correlation Measurement Technique: Coincidence Detection

The photoelectric detection occurring within an optical field exhibits spatial and temporal correlations. One method to demonstrate this correlation is by effectively multiplying the output currents of two detectors. Another, powerful and the most known procedure for gathering information about the joint probability $P_2(\vec{r}_1, t; \vec{r}_2, t+\tau)$ is to feed the photoelectric pulses from the two detectors to a coincidence counter (Ficek and Swain, 2005), as given in Figure 3.12, to measure the rate at which pulses from the two detectors arrive "in coincidence". A coincidence counter delivers an output pulse whenever pulses appear at its two inputs simultaneously or in coincidence, and not otherwise. However, the phrase "in coincidence" must be interpreted by reference to the intrinsic time resolution T_r of the circuit, which is limited by the width or rise time of pulses. By definition, two pulses at two inputs that begin at time t and $t+\tau$, respectively, will be judged to be coincidence if $|\tau| \leq \frac{T_r}{2}$ (see the channels in Figure 3.12). If $P_2(\vec{r}_1, t; \vec{r}_2, t+\tau)\Delta t \Delta\tau$ is the joint probability that one pulse appears at one input at time t within Δt and another input at time $t+\tau$ within $\Delta\tau$, the average rate R_c at which coincidence circuit delivers output pulses will be:

$$R_c = \int_{-T_r/2}^{T_r/2} P_2(\vec{r}_1, t; \vec{r}_2, t+\tau) d\tau \tag{3.26}$$

Using Equation (3.22), the last equation becomes (Mandel and Wolf, 1995):

$$R_c = R_1 R_2 T_r \left(1 + \frac{1}{T_r} \int_{-T_r/2}^{T_r/2} \lambda(\vec{r}_1, t; \vec{r}_2, t+\tau) d\tau \right) \tag{3.27}$$

in which $R_1 \equiv \alpha_1 S_1 \langle \hat{I}(\vec{r}_1) \rangle$ and $R_2 \equiv \alpha_2 S_2 \langle \hat{I}(\vec{r}_2) \rangle$ are the average rates at which pulses arrive in the two input channels. The first term on the right side of equation represents the random or accidental contribution to the coincidence rate R_c, resulting the purely random overlap of input pulses. However, the second term represents excess contribution to the light intensity fluctuations which can be either positive or negative.

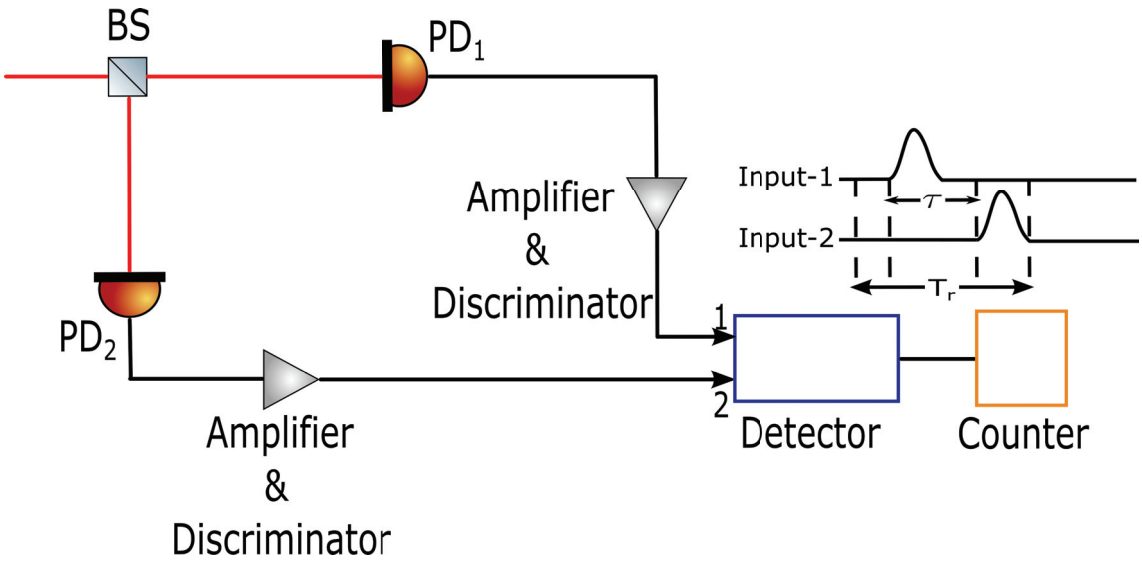

Figure 3.12. A typical correlation experiment setup based on coincidence detection

If we assume stationary and cross-spectrally pure light, we can write intensity correlation function in terms of second order correlation function as:

$$\lambda(\vec{r}_1, t; \vec{r}_2, t+\tau) = |\gamma(\vec{r}_1, \vec{r}_2, \tau)|^2 = |\gamma(\vec{r}_1, \vec{r}_2, 0)|^2 |\gamma(\tau)|^2 \tag{3.28}$$

From the coherence time definition from the statistical optics (Saleh and Teich, 2019):

$$\int_{-\infty}^{\infty} |\gamma(\tau)|^2 d\tau = T_c \tag{3.29}$$

where T_c represents the coherence time of light. Since T_r is greatly exceeded the correlation time in coincidence time experiments, we may replace the integral limits in Equation (3.27) by $\pm\infty$ to a reasonable approximation:

$$\int_{-T_r/2}^{T_r/2} |\gamma(\tau)|^2 d\tau \approx \int_{-\infty}^{\infty} |\gamma(\tau)|^2 d\tau = T_c \tag{3.30}$$

Then, it becomes:

$$R_c = R_1 R_2 T_r [1 + (T_c/T_r)|\gamma(\vec{r}_1, \vec{r}_2, 0)|^2] \tag{3.31}$$

It can be concluded from the equation above that the light fluctuations is to produce an excess contribution to the coincidence rate R_c, over accidental rate $R_1 R_2 T_r$, but the feasibility of detecting this excess strongly depends on the ratio T_c/T_r. If the coherence time of light is considered as a few nanoseconds on the experiments, the coincidence circuit resolving time must be on the order of 10^{-8} or 10^{-9} s. If resolving time becomes greater, the contribution due to the correlation can not be detected due to the averaging. Therefore, not only the statistical distribution approximate Poisson distribution but also the second order correlation function approximate to one. Considering entangled photons with coherence time smaller than picoseconds as in (Halder et al., 2008; Durak, 2020), coincidence detector resolving time should be around picoseconds to detect correlation on the detector for entanglement case. Besides, if we consider the entangled photon case with no coincidence due to the time separation between signal and idler photons, we can not talk about correlation since there is no overlap between signal and idler photons pulses. At this time, we only obtain the multiplication independent single photons probabilities on the detectors independently. The coincidence rate becomes:

$$R_c = R_1 R_2 T_r \tag{3.32}$$

which corresponds to the product of average intensities measured by the two detectors.

Other problem can be about the coincidence detection is the successive births of entangled photon pairs in a short time period. In this case, the detectors can not detect one photon pair (i.e., due to the dead time of the detector). However, this situation has a low probability in SPDC since the conversion efficiency (biphotons made per incident

pump photon) is of the order 10^{-8} (Schneeloch and Howell, 2016). Lastly, if the thermal and coherent source cases are examined, the resolving time issue is again a problem. Although coherent light has coherence length in several meters which corresponds coherence time on the order nanoseconds, the conventional scientific cameras can not resolve information in terms of both optical coherence function and photon statistics. As a result, the selection of detector plays a significant role in the field of photodetection to extract accurate statistics. Although, each light source has different requirements, detectors above a certain specifications are needed to perform even the simplest measurements.

CHAPTER 4

ENTANGLEMENT-BASED THIN FILM CHARACTERIZATION

This chapter presents a novel scheme based on the phase diffraction of spatially structured entangled photons to characterize the thickness of nanoscale dielectric films coated on optical fiber. The photons are tracked as rays by neglecting minor decoherence effects due to the short optical path length inside the phase object, simplifying the mathematical model. We have demonstrated that the transverse spatial correlations significantly improve the accurate determination of film thickness. The spatially entangled photons are also combined with a narrower aperture to yield confocality, further improving the thickness precision.

4.1. Biphoton Phase Diffraction from Optical Fiber

The general scheme of the classical phase diffraction model was given in Figure 1.2. The input field diffracts from the phase object and propagates to the sensor array exposing specific phase delays due to the three-layer geometry. Therefore, every point of the input field is represented by independent rays at the beginning of the phase object and tracked paraxially to obtain optical path length. After the wavefront is obtained at the output face of the fiber, the resultant diffraction pattern is calculated using the Huygens'-Fresnel diffraction formula (Makris and Psaltis, 2011). Then, the pattern is evaluated by curve fitting methods to extract optical parameters of phase object.

However, the mathematical model may show some differences in entanglement-based systems. In our model, we are interested in degenerate ($\omega_s = \omega_i$) collinear type-II SPDC where the generated signal and idler photons have equal but opposite wave vectors due to the momentum conservation at the output of non-linear crystal. This situation causes different scattering angles, transmission amplitudes, and optical path lengths for both photons. The scattering angles (α) are very close to zero with respect to the pump photon direction (k_{pz}) in nearly collinear SPDC (see Figure 4.1(a)). The probability of possible scattering angles is at about ± 30 mrad (Strekalov et al., 1995), as given in Figure 4.1(b) where the standard deviation (σ) is 10 mrad. As seen from Figure 4.1(b), the photon

pairs born $\%95.4$ probability with scattering angles smaller than ± 20 mrad.

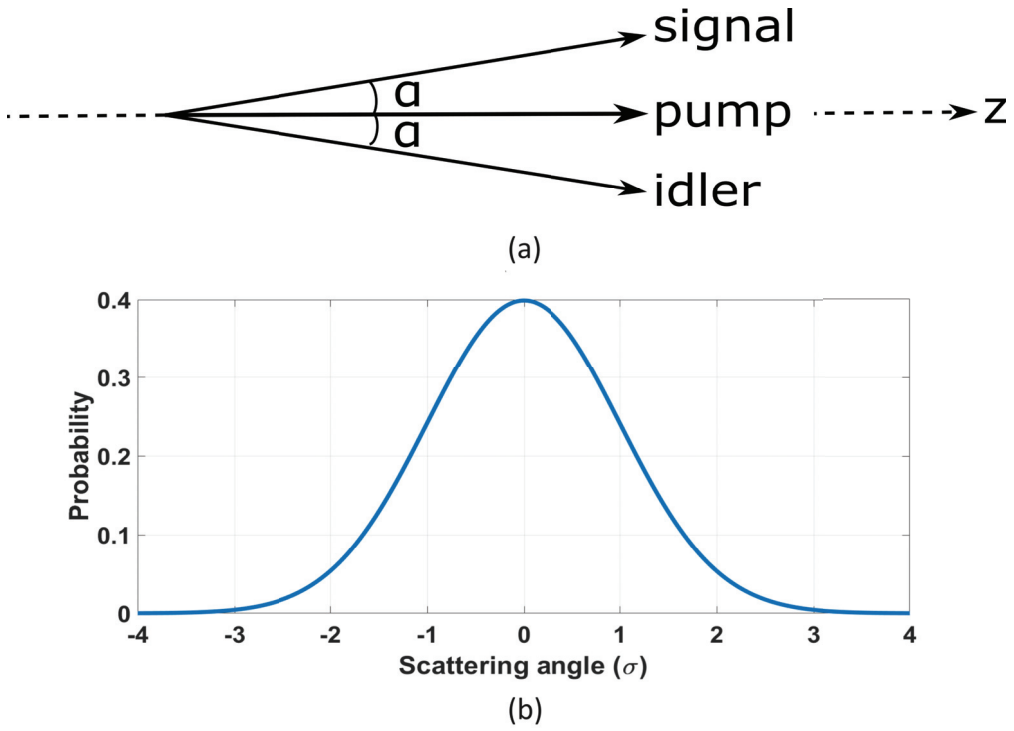

Figure 4.1. (a) Scattering angle geometry for nearly collinear emission (b) Probability of possible scattering angles of entangled photons generated by collinear SPDC

The exact tracing of a signal photon inside the optical fiber is given in Figure 4.2. The radius of core and cladding are represented by a and b, and n_s, n_{cl}, and n_{co} are the refractive index surrounding medium, cladding, and core, respectively. The optical path length of the signal photon can be written as neglecting the core due to small size and $n_{cl} \approx n_{co}$:

$$\varphi(x) = n_s\overline{OA} + n_{cl}\overline{AB} + n_s\overline{BP} \tag{4.1}$$

where according to the Snell law:

$$n_s \sin(\theta_1 + \alpha) = n_{cl} \sin(\theta_2) \tag{4.2}$$

and

$$\overline{OA} = \frac{b(1-\cos(\theta_1))}{\cos(\alpha)} \tag{4.3}$$

$$\overline{AB} = 2b\cos(\theta_2) \tag{4.4}$$

$$\overline{BP} = \frac{b(1-\cos(2\theta_2-\theta_1))}{\cos(2(\theta_2-\theta_1))} \tag{4.5}$$

Then, Equation (4.1) becomes:

$$\varphi(x) = n_s\frac{b(1-\cos(\theta_1))}{\cos(\alpha)} + 2n_{cl}b\cos(\theta_2) + n_s\frac{b(1-\cos(2\theta_2-\theta_1))}{\cos(2(\theta_2-\theta_1))} \tag{4.6}$$

Also an arbitrary point P on the x-plane can be represented as:

$$P(x) = b\sin(2\theta_2-\theta_1) - b\tan(2\theta_1-2\theta_2)(1-\cos(2\theta_2-\theta_1)) \tag{4.7}$$

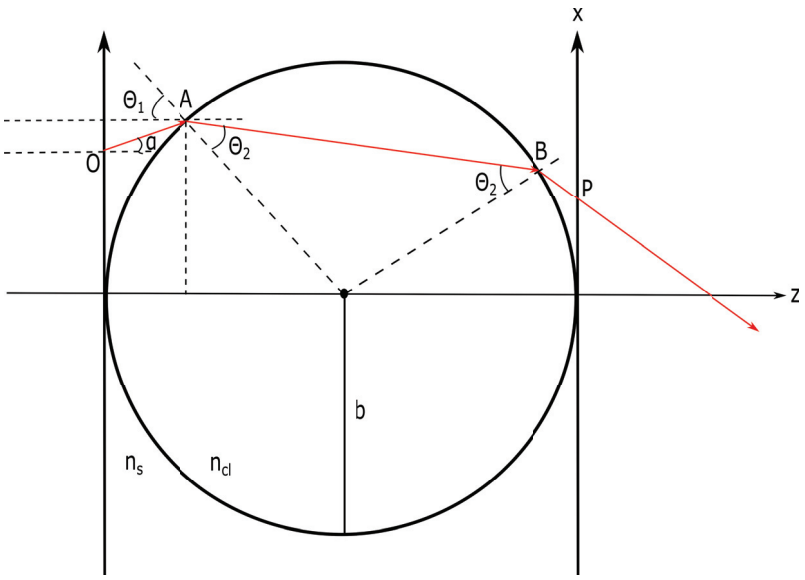

Figure 4.2. Exact tracing geometry of a photon traversing to phase object

The amplitude of the tracked field at point P can be written as:

$$A_P(x) = t_{1j}t_{2j}A_{ini} \tag{4.8}$$

where t_{1j} and t_{2j} are the Fresnel coefficients at point A and B for signal and idler (j=s,i), respectively and A_{ini} is the initial amplitude at the beginning of the phase object (point A). Since the signal and idler photons are orthogonal each other, the Fresnel coefficients are also different for both. Assuming the signal photon has vertical polarization, t_{1s} and t_{2s} are written as:

$$t_{1s} = \frac{2n_s \cos(\theta_1 + \alpha)}{n_s \cos(\theta_1 + \alpha) + n_{cl} \cos(\theta_2)} \tag{4.9}$$

$$t_{2s} = \frac{2n_{cl} \cos(\theta_2)}{n_{cl} \cos(\theta_2) + n_s \cos(\theta_1 + \alpha)} \tag{4.10}$$

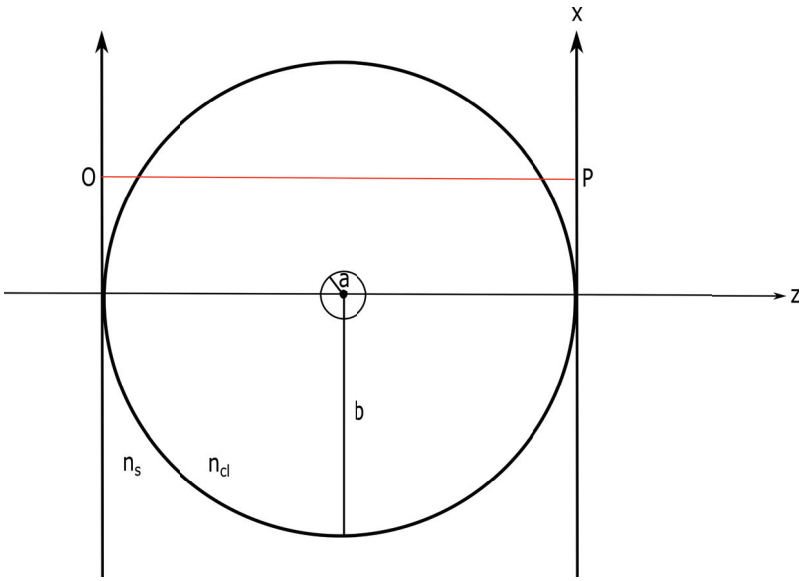

Figure 4.3. Paraxial tracing geometry of a photon traversing to phase object

Furthermore, the tracing process may also be modeled via paraxial tracing, as our experimental design, to obtain a simple model given in Figure 4.3. At this time, it is assumed that the signal and idler photons experience same phase delay through the system. The simple analytical expressions of signal's (or idler's) optical path lengths can be written as:

$$\begin{aligned}
\varphi(x) &= exp(i\phi_s), \quad |x| > b \\
\varphi(x) &= exp(i[\phi_s + \phi_{cl}]), \quad a < |x| < b \\
\varphi(x) &= exp(i[\phi_s + \phi_{cl} + \phi_{co}]), \quad 0 < |x| < a
\end{aligned} \tag{4.11}$$

where a, b are the core and the cladding radii, respectively. Furthermore, ϕ_s, ϕ_d, ϕ_{cl} and ϕ_{co} are represented as:

$$\begin{aligned}\phi_s &= 2kn_s b,\\ \phi_{cl} &= 2k(n_{cl}-n_s)\sqrt{b^2-x^2},\\ \phi_{co} &= 2k(n_{co}-n_{cl})\sqrt{a^2-x^2}\end{aligned} \tag{4.12}$$

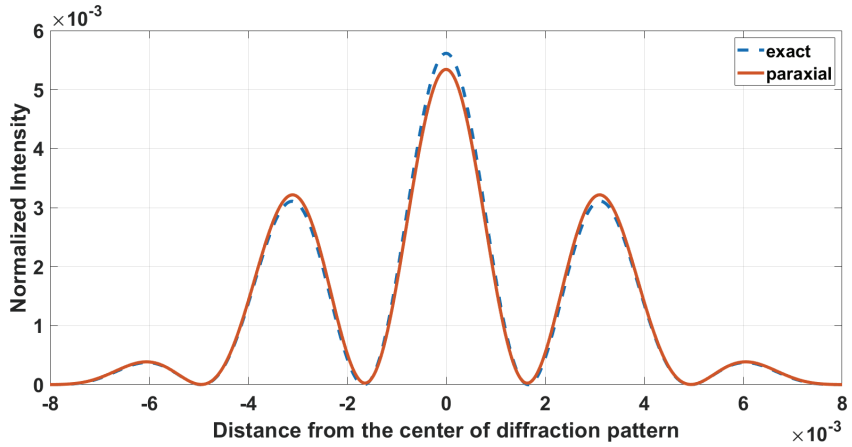

Figure 4.4. Simulation result of biphoton phase diffraction from 300 μm aperture for exact (blue) and paraxial (orange) tracing

In simulations, we investigate the necessity of exact photon tracing on the entanglement-based systems by comparing paraxial tracing. We choose aperture size as 300 μm to ensure the validity of paraxial approximation since the effect of exact amplitudes and phases increase by blocking stray biphotons. The normalized intensity patterns of exact and paraxial tracing biphoton phase diffraction are given in Figure 4.4. The scattering angles of signal and idler photons are taken $\pm$ 30 mrad which is approximately upper limit of angle. Although the exact paths and amplitudes are different on nano-scales, the result show no noticeable differences in amplitudes and zeros crossing of the patterns.

To verify our integration used in mathematical equations, we also make computational error and convergence analysis. The system model is created in "$Matlab$" environment. In the code, we used $integral2$ command for integration. It transforms the region of integration to a rectangular shape and subdivides it into smaller rectangular regions as needed. Also, we convert the integration to the summation via discritization for various

step sizes. According to the results, the deviation (σ) between two different method is on the order of 10^{-5} given in below.

$$\sigma = \sum_{i=1}^{N} \frac{|y_i - \bar{y_i}|}{N} \tag{4.13}$$

where y_i is the $integral2$ result and $\bar{y_i}$ is the summation result. Therefore, there is no significant differences between two methods for the utilization in system model.

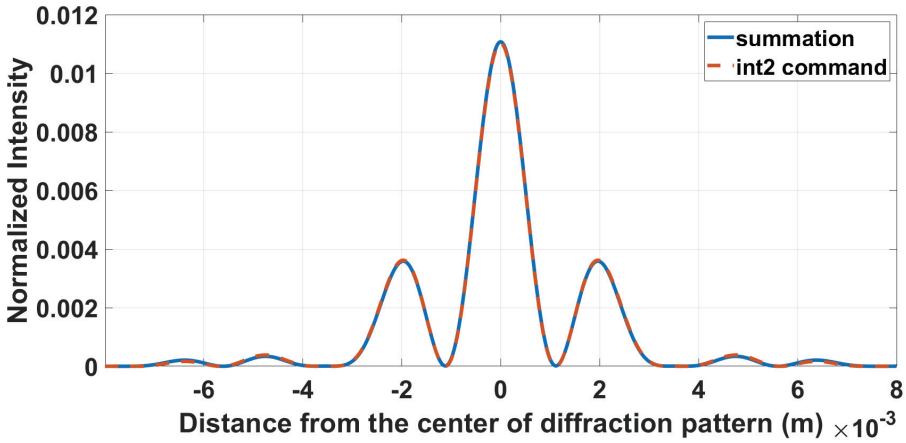

Figure 4.5. Diffraction pattern differences between summation having 10 nm step size (blue) and $integral2$ command (orange)

Table 4.1. The convergence analysis between summation and integral2 command for various step sizes

	20 nm	**15 nm**	**10 nm**	**5 nm**	**1 nm**
σ	2.3043×10^{-5}	2.3042×10^{-5}	2.3042×10^{-5}	2.3032×10^{-5}	2.3024×10^{-5}

4.2. Mathematical Model of Proposed System

The general overview of the proposed setup for dielectric film characterization is given in Figure 4.6. In the beginning, the degenerate collinear type-II SPDC process

is used, assuming the pump is sufficiently plane and the nonlinear crystal is very thin. Since the conservation of momentum requires well-defined, equal, and opposite exiting angles for signal and idler photons at the output of crystal, all photons can be modeled as rays (Pittman et al., 1996). Furthermore, the signal and idler photons have very small angles with respect to the pump direction (k_{pz}) (Strekalov et al., 1995). This means that they propagate same direction with the pump. This then allows us to make a simple and practical model in the following manner: parallel wavevectors for signal and idler photons with opposite polarizations. This way, spatially entangled photons can be tracked using paraxial ray approximation. The critical point is that collinearity provides paraxial tracing where orthogonality contributes to the visibility in the system.

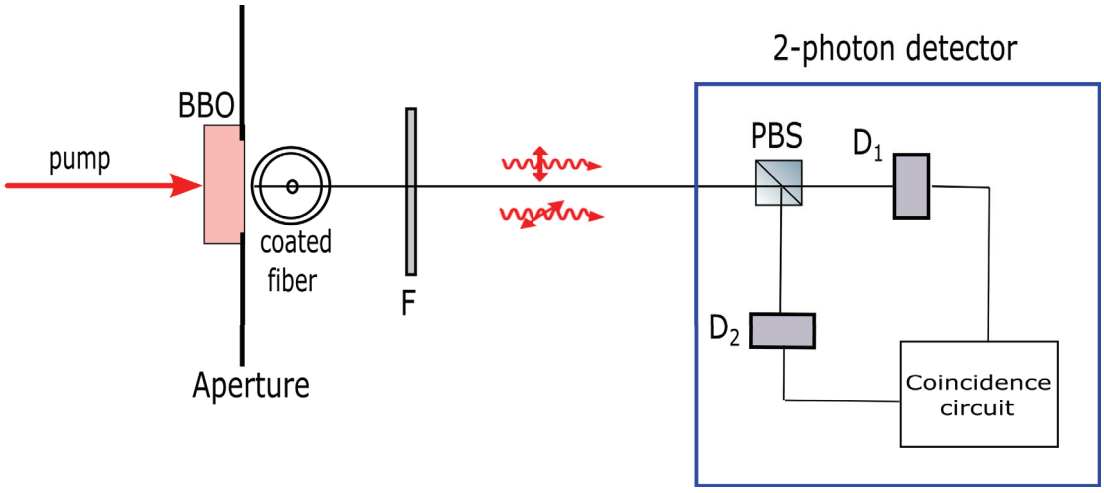

Figure 4.6. Proposed spatial entanglement based phase diffraction setup for transparent dielectric film characterization

The geometry of phase object and optical paths are given in Figure 4.7. The pairs are exposed to specific phase delays due to curved geometry and carry thickness information to the diffraction pattern. By courtesy of entanglement, phase delay inside traversing phase object region and so carried thickness information at the detectors is doubled. This causes significant deviations in amplitude and position on the resultant diffraction pattern. It is also seen from Figure 4.7 that the photon pair takes the longest path p_3 inside dielectric coating whereas p_4 is the stray path. Therefore, the aim is to limit the entangled photons by locating a narrow aperture close to the phase object. In this way, we can obtain confocality and detect nanometer thickness variations in the diffraction pattern more precisely via suppressing stray biphotons which propagate through air.

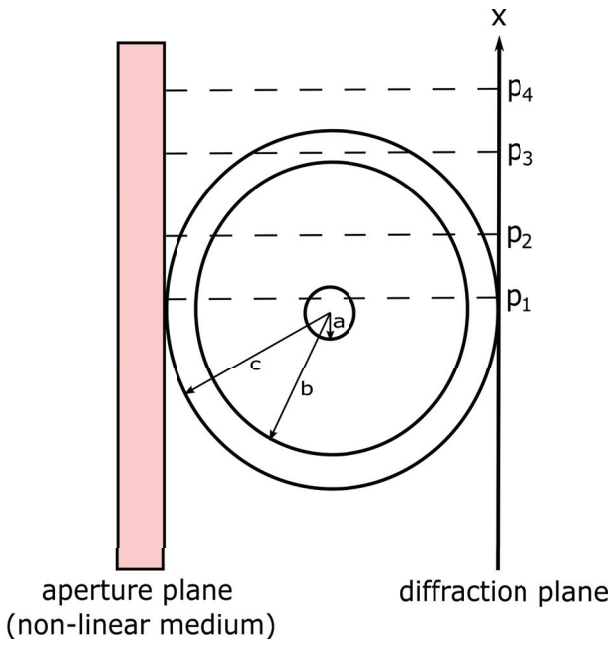

Figure 4.7. Optical paths for the regions of curved geometry

In mathematical model, the spatially entangled photon pairs born at any position on the aperture plane. Then, they propagate through the coated optical fiber experiencing different paths corresponding to the cross-section plane. Since the deflections through the fiber and inclination factor have no significant effect on intensity for large phase objects (Sabatyan and Tavassoly, 2007), the optical path lengths can be expressed as:

$$\begin{aligned}
&\varphi(x) = exp(i\phi_s), \quad |x| > c \\
&\varphi(x) = exp(i[\phi_s + \phi_d]), \quad b < |x| < c \\
&\varphi(x) = exp(i[\phi_s + \phi_d + \phi_{cl}]), \quad a < |x| < b \\
&\varphi(x) = exp(i[\phi_s + \phi_d + \phi_{cl} + \phi_{co}]), \quad 0 < |x| < a
\end{aligned} \tag{4.14}$$

where a, b and c are the core, the cladding and the coated optical fiber radii, respectively. In addition, ϕ_s, ϕ_d, ϕ_{cl} and ϕ_{co} are represented as:

$$\begin{aligned}
&\phi_s = 2kn_s c, \\
&\phi_d = 2k(n_d - n_s)\sqrt{c^2 - x^2}, \\
&\phi_{cl} = 2k(n_{cl} - n_d)\sqrt{b^2 - x^2}, \\
&\phi_{co} = 2k(n_{co} - n_{cl})\sqrt{a^2 - x^2}
\end{aligned} \tag{4.15}$$

where n_s, n_d, n_{cl} and n_{co} are refractive indices of the surrounding medium, the dielectric film, the cladding and the core, respectively.

After paraxial tracing, the resultant biphotons are exposed diffraction between exiting face of the fiber (diffraction plane) and detector plane. In the scheme, the filter (F) is used for pump suppression, and the signal and idler photons are separated by a polarizing beam splitter (PBS). The signal and idler have the same path length to the detectors. At the end, they are detected by coincidence detector arrays D_1 and D_2. The biphoton diffraction pattern is obtained by the coincidence counts recorded as a function of the spatial coordinates of ρ_1 on the detector D_1 and ρ_2 on the detector D_2. For this setup with aperture width d, the joint detection probability can be calculated as:

$$G^{(2)}(\rho_1, z; \rho_2, z) = \prod(T_D) \left| \tilde{\Phi}_0 \int_{-d/2}^{d/2} dx \varphi(x) e^{-i\frac{\omega}{cz}(x\cdot\rho_1 + x\cdot\rho_2)} \right|^2 \tag{4.16}$$

where $\prod(T_D)$ is a rectangular-shaped function. It takes the value "1" if the difference between detector click times is less than a particular value and "0" otherwise (Sergienko et al., 1995). It depends on the length (L) of the crystal and is expressed as:

$$\prod(T_D) = \begin{cases} 1, & 0 < T_D < DL \\ 0, & \text{otherwise} \end{cases} \tag{4.17}$$

where $D \equiv 1/\upsilon_{s(i)} - 1/\upsilon_{i(s)}$ and, υ_s and υ_i are the group velocity of signal and idler.

4.3. Numerical Simulations and Discussion

In this sub-section, we mainly focus on the contribution of the spatial entanglement concept to the precise determination of film thickness. We also investigate how changing the aperture size improves thickness resolution further. Experimental parameters from the literature are used as the simulation parameters to implement proposed model. We evaluate two scenarios for the comparisons of two different down-conversion wavelengths. Firstly, a CW (continuous wave) 351 nm line of an argon-ion laser is used to pump beta barium borate (BBO) ($\beta - BaB_2O_4$), which is cut for degenerate collinear type-II phase matching, to produce orthogonally polarized entangled photons (Strekalov et al., 1995). Secondly, we change the pump with a CW 458 nm line of an argon-ion laser as given in the (D'Angelo et al., 2001). The wavelength of the biphotons is 702 nm and

916 nm in these two different scenarios, respectively. The distance between the phase object and detectors is $z = 2$ m. The radius of core and cladding are $a = 2.2$ μm and $b = 62.5$ μm and the refractive indices are $n_{co} = 1.4591$ and $n_{cl} = 1.4537$, respectively. Indium-tin oxide (ITO) and polyvinyl alcohol (PVA) are chosen as the transparent coating materials, which have a refractive index 1.71 and 1.47 at the wavelength of interest (Shao et al., 2018; Kapoor and Sharma, 2020). Both detectors are preceded by a spectral filter (F) centered at the degenerate wavelength 702 nm for the ITO case and 916 nm for the PVA case (Pittman et al., 1995). The coincidence detector arrays are assumed to have 20 μm pixel sizes which is in the suitable range (Madonini et al., 2021).

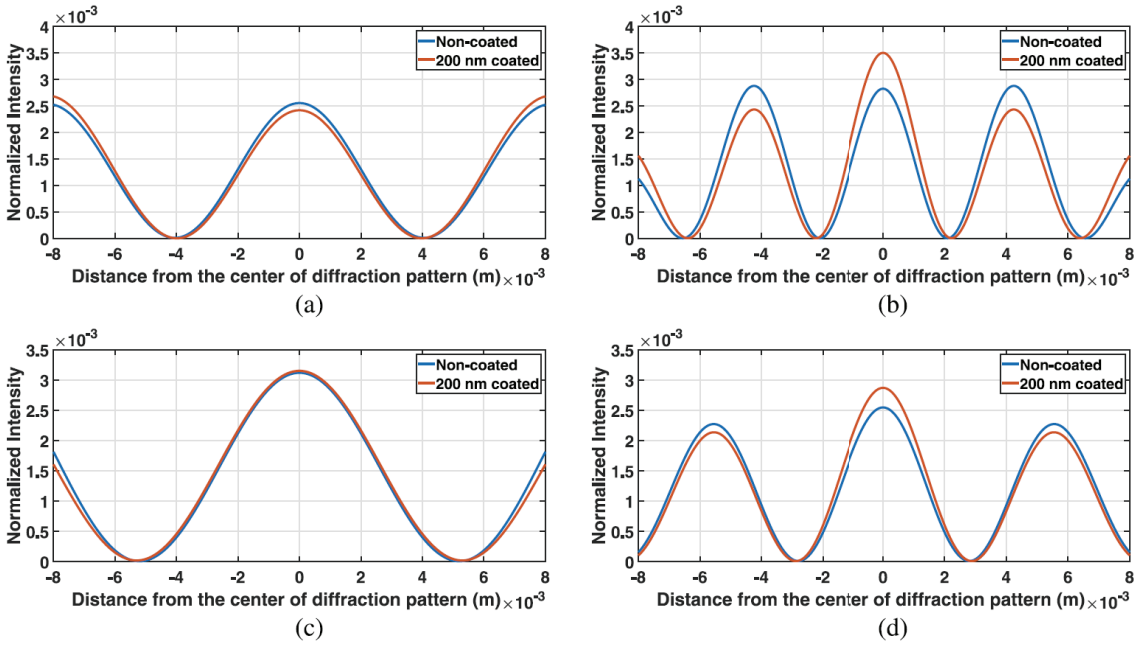

Figure 4.8. Simulation results of diffraction pattern deviation for 200 μm aperture: (a) classical case with 351 nm pump for non-coated and 200 nm ITO coated fiber (b) spatially entangled case with 351 nm pump for non-coated and 200 nm ITO coated fiber (c) classical case with 458 nm pump for non-coated and 200 nm PVA coated fiber (d) spatially entangled case with 458 nm pump for non-coated and 200 nm PVA coated fiber (Ataç and Dinleyici, 2023b)

To show the influence of biphotons on the system precision, we simulated two different cases given in Figure 4.8. The utilization of spatially entangled photons allows us to achieve the inherently higher thickness resolution due to the intensity correlations since the phase delay inside the phase object increases by factor 2. As seen from Figure 4.8(a) and (c), the deviation between non-coated and 200 nm coated optical fiber is not

distinct for the classical phase diffraction method (Ekici and Dinleyici, 2017) which is realized with plane wave case for two different coating materials at two down-conversion wavelengths. However, the effect of the nanoscale film becomes observable for entangled photon pairs in Figure 4.8(b) and (d) courtesy of spatial correlations. Despite the large aperture size compared with the phase object, the zero crossings shift and amplitude changes significantly. Since the number of alternative paths decreases at the polarizing beam splitter due to the well-defined polarizations of entangled photons, which prevent background noise, the diffraction pattern also has high visibility.

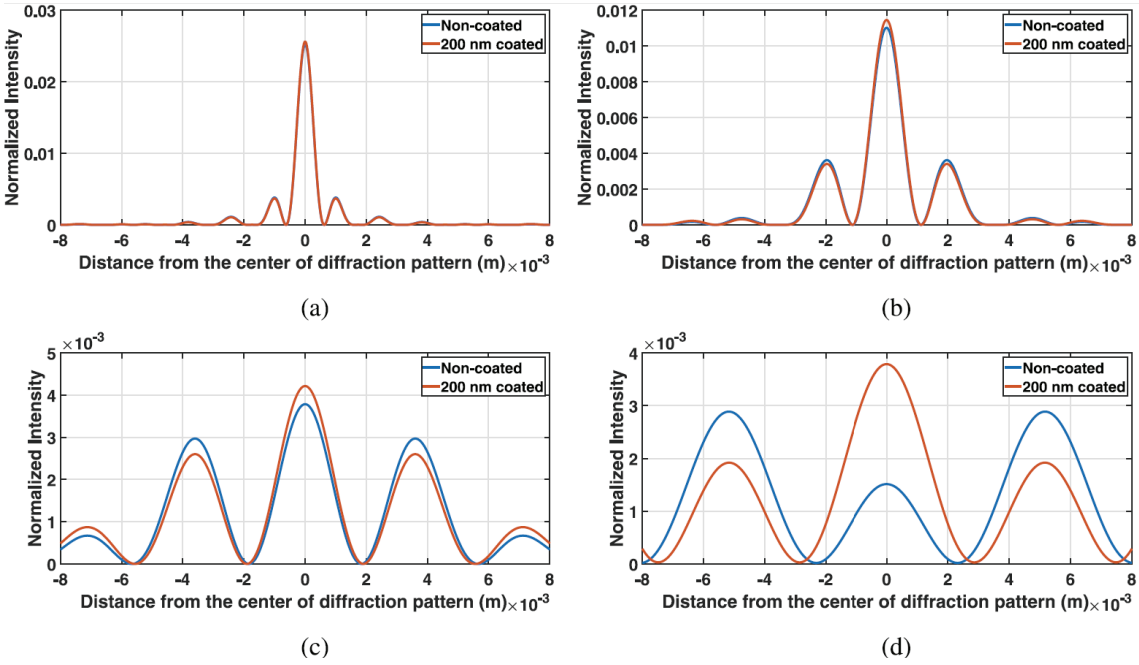

Figure 4.9. Simulation results of diffraction pattern deviation of non-coated and 200 nm ITO coated fiber with 351 nm pump for various aperture size (a) 1000 μm (b) 500 μm (c) 250 μm (d) 150 μm (Ataç and Dinleyici, 2023b)

To provide further enhancement on the resolution, we utilized the fundamental principle of confocal microscopy with an aperture (single slit in our case). In this way, we can block stray biphotons traversing through the air, which causes suppression of the thickness information about the film. The diversity of normalized diffraction patterns between non-coated and 200 nm ITO coated fibers with different aperture sizes are depicted in Figure 4.9. As expected, the 1000 μm aperture, much larger than the phase object, the pattern is nearly a single slit biphoton diffraction pattern due to the domination of stray biphotons. Therefore, we can not extract the thickness value since there is no discrepancy

between the patterns for sub-wavelength coating thicknesses. However, despite the ultra thin film thickness, it can be discriminated from non-coated fiber for 150 μm aperture. As seen from Figure 4.9(d), minimums shift approximately 540 μm and the amplitudes change significantly. The separation between first minima for non-coated and 200 nm ITO coated fiber according to the various aperture sizes is given in Figure 4.10.

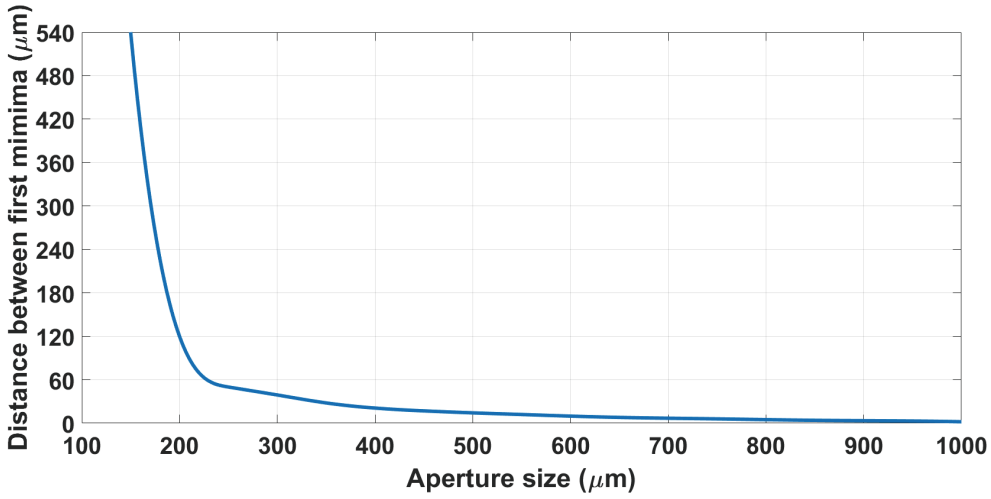

Figure 4.10. The distance between first minima for various aperture sizes (200 nm ITO coating) (Ataç and Dinleyici, 2023b)

Table 4.2. Evaluation of main lobe amplitude ratio and minima shift for various ITO coating thickness (Ataç and Dinleyici, 2023b)

Coating thickness	**200 nm**	**100 nm**	**50 nm**	**25 nm**	**10 nm**
Amplitude ratio	2.51	1.8	1.35	1.2	1.06
Minima shift	540 μm	270 μm	135 μm	67.5 μm	25 μm

The other investigation is about the detectable thickness value for proposed setup. We focus on thickness around 50 nm due to importance in SPR sensors. The aperture size is fixed as 150 μm which is comparable with the size of the phase object. In this way, the diffraction pattern includes more thickness information about the coating. The numerical simulations are given in Figure 4.11. Observable differences arise despite film thickness. The position shift of first minima versus coating thickness up to 100 nm is given in Figure 4.12. The shift of the first minimum is at around 70 μm for 25 nm coating,

and it increases with larger thickness values. Furthermore, representative data is provided in Table 4.2 to demonstrate the amplitude ratio and minimum shift between coated and non-coated fiber. The outputs reveal that the dielectric film thickness up to 25 nm can be accurately estimated. The thickness below 25 nm may not be measured due to the small main lobe amplitude ratio and minimum deviations on the biphoton diffraction pattern as well as the low-intensity values on coincidence detection and noise noise factors.

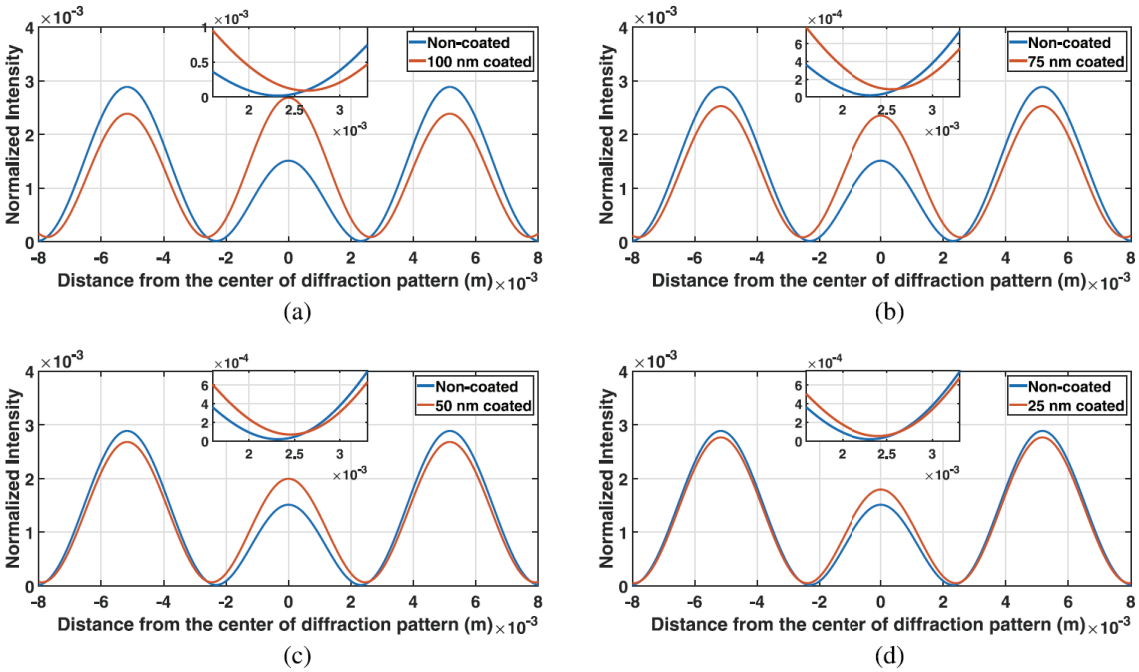

Figure 4.11. Simulation results for 150 μm aperture with 351 nm pump (a) non-coated and 100 nm ITO coated (b) non-coated and 75 nm ITO coated (c) non-coated and 50 nm ITO coated (d) non-coated and 25 nm ITO coated (Ataç and Dinleyici, 2023b)

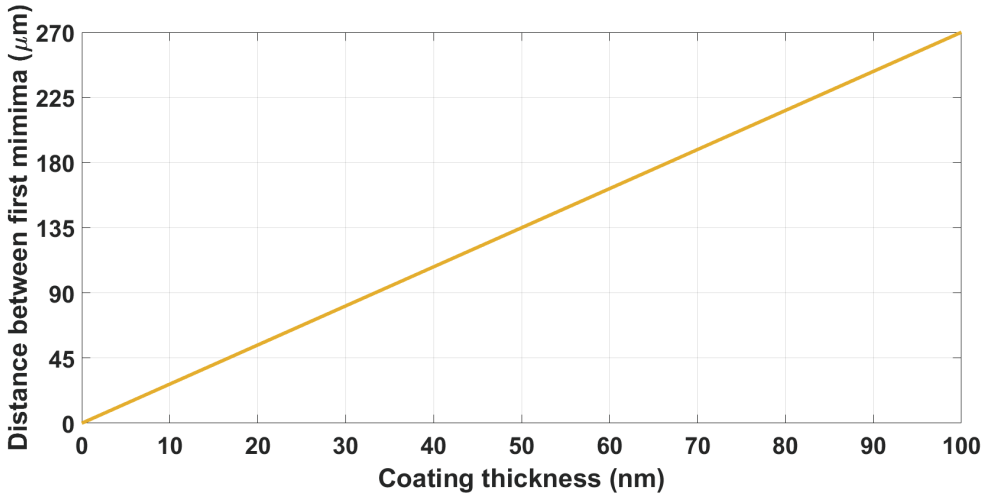

Figure 4.12. The distance between first minima versus various ITO coating thickness (for fixed 150 μm aperture) (Ataç and Dinleyici, 2023b)

4.4. An Alternative Model: Thermal Photon Phase Diffraction

Entangled photons generated by SPDC exhibit several properties analogous to the ordinary photons generated by incoherent sources (Saleh et al., 2000). This means that each photon pairs are correlated in itself but mimic classical independent point sources between each other. Therefore, entangled photons can be also imitated as independent point sources generated by chaotic light sources (Scarcelli et al., 2004; Zhai et al., 2005). In this way, main disadvantages of utilization of entangled photons in our system can be eliminated: (1) strict alignment in experimental setup for phase matching, (2) low conversion efficiency (biphotons made per incident pump photon) on the order 10^{-8}.

In the quantum theory of photodetection, the second order correlation function is calculated as:

$$G^{(2)}(t_1,\vec{r}_1;t_2,\vec{r}_2) = Tr\left[\rho E_1^{(-)}(t_1,\vec{r}_1)E_2^{(-)}(t_2,\vec{r}_2)E_2^{(+)}(t_2,\vec{r}_2)E_1^{(+)}(t_1,\vec{r}_1)\right] \tag{4.18}$$

where the density matrix is:

$$\rho \propto \sum_{\vec{q}}\sum_{\vec{q}'} |1_{\vec{q}}1_{\vec{q}'}\rangle \langle 1_{\vec{q}}1_{\vec{q}'}| \tag{4.19}$$

where the light source is modeled as an incoherent statistical mixture of two photons with

equal probability of having any transverse momentum $\vec{q}$ and $\vec{q}\prime$.

The transverse part of second order correlation function can be written as (Scarcelli et al., 2006):

$$\begin{aligned} G^{(2)}(\vec{x}_1;\vec{x}_2) &= \sum_{\vec{q},\vec{q}\prime} \langle 1_{\vec{q}} 1_{\vec{q}\prime} | E_1^{(-)}(\vec{x}_1) E_2^{(-)}(\vec{x}_2) E_2^{(+)}(\vec{x}_2) E_1^{(+)}(\vec{x}_1) | 1_{\vec{q}} 1_{\vec{q}\prime} \rangle \\ &= \sum_{\vec{q},\vec{q}\prime} |\langle 0 | E_2^{(+)}(\vec{x}_2) E_1^{(+)}(\vec{x}_1) | 1_{\vec{q}} 1_{\vec{q}\prime} \rangle|^2 \end{aligned} \tag{4.20}$$

where $\vec{x}_j$ is the transverse coordinate of jth detector. Also the electric field operator can be written as:

$$E_j^{(+)}(x_j) = \sum_{\vec{q}} g_j(\vec{x}_j;\vec{q}) \hat{a}(\vec{q}) \tag{4.21}$$

where $\hat{a}(\vec{q})$ is the annihilation operator for the mode corresponding to $\vec{q}$ and $g_j(\vec{x}_j;\vec{q})$ is the Green's function associated to the propagation of the field from the source to the detector.

Figure 4.13. Hanbury-Brown-Twiss (HBT) configuration

Substituting electric field operators in HBT setup given in Figure 4.13, joint detection probability becomes:

$$G^{(2)}(\vec{x}_1;\vec{x}_2) = \sum_{\vec{q},\vec{q}\prime} |g_1(\vec{x}_1,\vec{q}) g_2(\vec{x}_2,\vec{q}\prime) + g_1(\vec{x}_1,\vec{q}\prime) g_2(\vec{x}_2,\vec{q})|^2 \tag{4.22}$$

Then,

$$G^{(2)}(\vec{x}_1;\vec{x}_2) = \sum_{\vec{q}} |g_1(\vec{x}_1,\vec{q})|^2 \sum_{\vec{q}\prime} |g_2(\vec{x}_2,\vec{q}\prime)|^2 + |\sum_{\vec{q}} g_1^*(\vec{x}_1,\vec{q}) g_2(\vec{x}_2,\vec{q})|^2 \tag{4.23}$$

which equals:

$$G^{(2)}(\vec{x}_1;\vec{x}_2) = G^{(1)}_{11}(\vec{x}_1)G^{(1)}_{22}(\vec{x}_2) + |G^{(1)}_{12}(\vec{x}_1,\vec{x}_2)|^2 \tag{4.24}$$

The first term in Equation (4.24) represents the product of the average intensities measured by the two detectors. However, the second term corresponds to the intensity fluctuations or two photon interference term. This equation is the basis of HBT effect. A fundamental difficulty in observing this effect is the small relative magnitude of second term when the coherence time of detected field is much smaller than the detection time interval.

If the coincidence rate for thermal case is written including time resolution of detectors and coherence time of light, it becomes (Mandel and Wolf, 1995):

$$G^{(2)}(\vec{x}_1;\vec{x}_2) = R_1R_2T_r[1 + (T_c/T_r)|G^{(1)}_{12}(\vec{x}_1,\vec{x}_2)|^2] \tag{4.25}$$

in which $R_1 \equiv \alpha_1 S_1\langle\hat{I}(\vec{r}_1)\rangle$ and $R_2 \equiv \alpha_2 S_2\langle\hat{I}(\vec{r}_2)\rangle$ are the average rates at which pulses arrive in the two input channels.

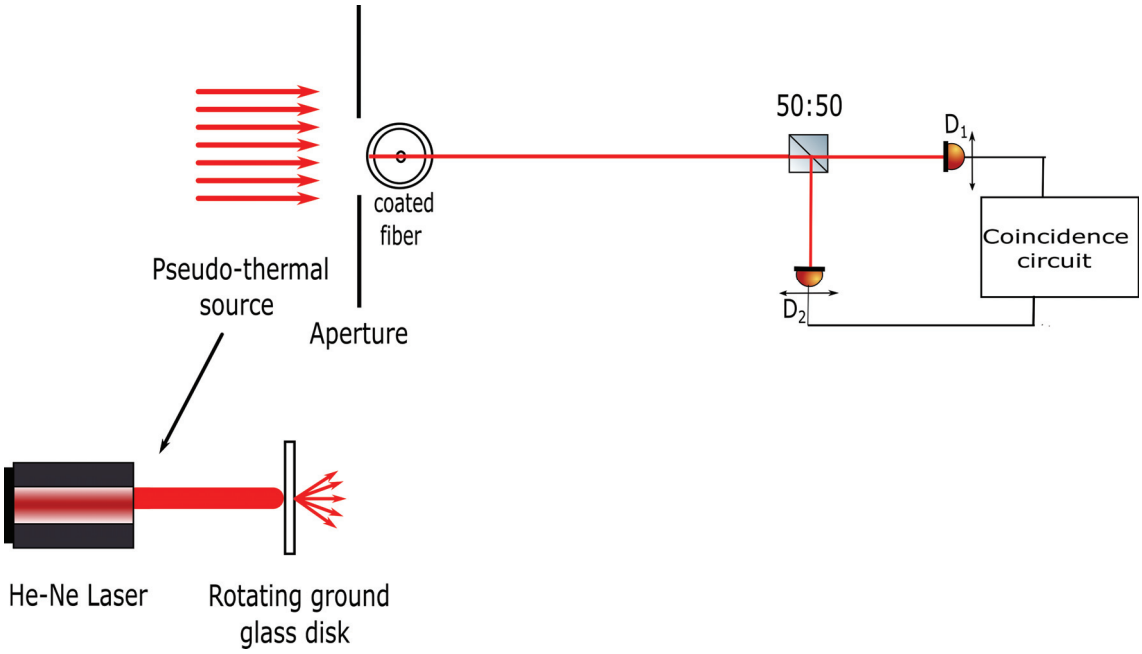

Figure 4.14. Proposed thermal photons based phase diffraction setup

The critical point is that photon coincidence rate in our proposed SPDC model with spatially entangled photons is:

$$G^{(2)}(\vec{x}_1;\vec{x}_2) = |\Psi(\vec{x}_1,\vec{x}_2)|^2 = |G_{12}^{(1)}(\vec{x}_1,\vec{x}_2)|^2 \tag{4.26}$$

which means that there is no background term. Therefore, although diffraction patterns are the same for thermal photons and entangled cases, they have different visibilities.

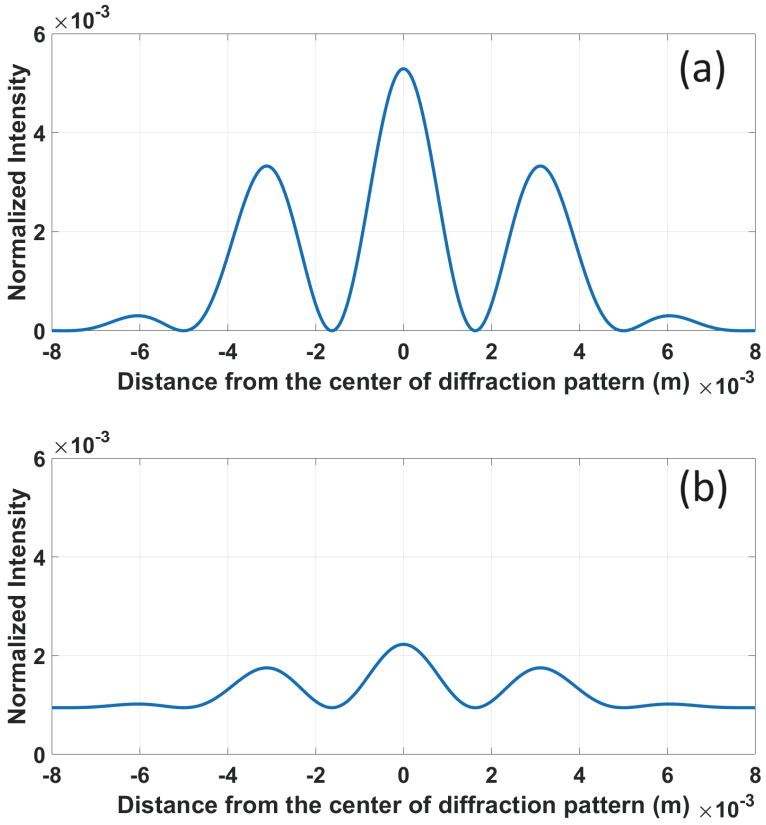

Figure 4.15. Simulation results for 300 μm aperture with 351 nm pump (a) spatially entangled photons (b) thermal photons

The general overview of the proposed setup with thermal photons is given in Figure 4.14. The numerical simulations assume same conditions with entangled case. We take time resolution of detectors $T_r = 25\ \mu s$ and coherence time of thermal photons $T_c = 8\ \mu s$, respectively. The resultant diffraction patterns for spatially entangled and thermal case are given in Figure 4.15. It can be seen that the visibility is %100 in entanglement case. This situation is already evident from the Equation (4.26). However, it

reduces approximately $V = 0.35$ in thermal case due to the DC offset. Therefore, the only difference between diffraction patterns is visibility as expected due to the analogy between thermal photons and entangled photons. This configuration proves that the proposed method may be realized with thermal source instead of spatially entangled photons.

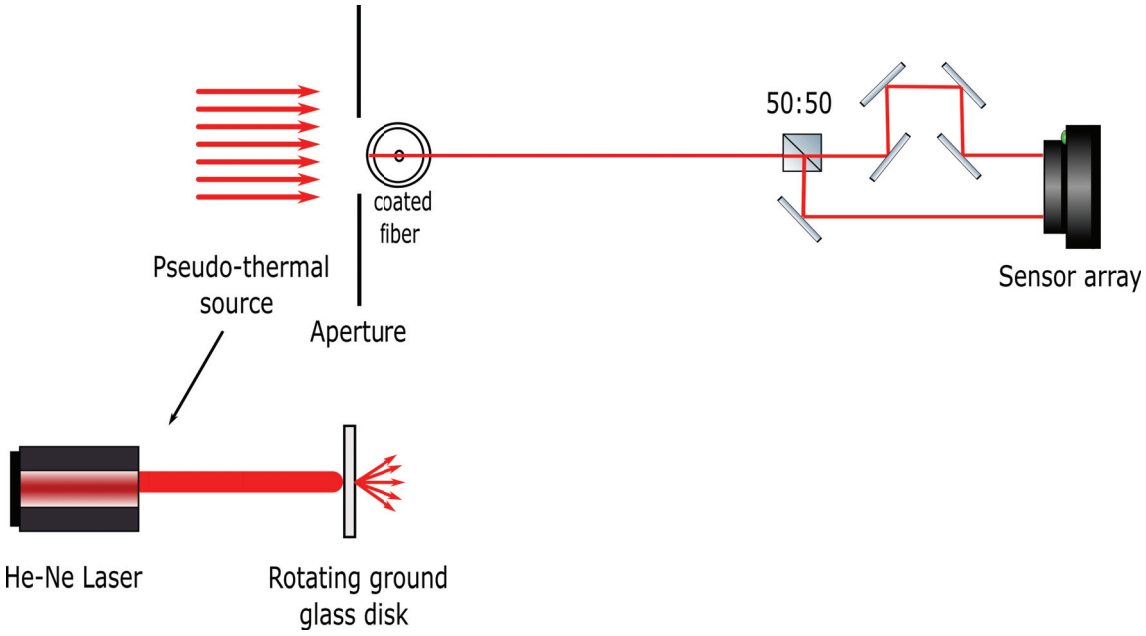

Figure 4.16. Proposed thermal photon based phase diffraction setup for transparent dielectric film characterization with single detector

Furthermore, we propose a configuration eliminating the utilization of two detectors in coincidence detection as given in Figure 4.16. The proposed setup needs one large detector array because we utilize the sensor's surface as two independent areas or detectors. Since the detector array behaves as having a self-coincidence circuit, we can avoid the time-synchronization problem. By adjusting the same optical path for the photons, we can realize coincidence detection in a single detector. Although this configuration can be problematic for large diffraction patterns (especially in far-field systems), it may be an alternative in scenarios with limited budgets.

CHAPTER 5

THERMAL LIGHT CHARACTERIZATION WITH A CCD

In this section, we propose a novel, practical, and low-cost experimental procedure for characterizing thermal light photon number statistics and normalized second order optical coherence function $g^{(2)}(\tau)$ using an ordinary CCD camera. The main idea is obtaining time-bin information from the spatially distributed intensity values. Since theoretical analysis indicates that confined area measurements of thermal light naturally lead to the Bose-Einstein statistics in the very faint light condition, the proposed model is mainly based on evaluating single pixels intensities of the CCD array. Considering that operating at the single-photon levels is not readily achievable in conventional CCD cameras, the photon number-intensity relation has been leveraged utilizing semi-classical approach. In this way, the photon counts on single pixels mapped to the intensity values have enabled the demonstration of thermal distribution and bunch light phenomenon. Furthermore, we also demonstrate that $g^{(2)}(0)$ of the thermal light source is well above the coherent case and close to the theoretical value two which is the signature of thermal light.

5.1. Mathematical Model and Experimental Preliminaries

In the proposed model, we focus on examining thermal light's photon statistics and second-order correlation function with an ordinary scientific CCD camera. However, both the generation of thermal light with an adjustable coherence time and its detection are not simple procedures, particularly in scenarios with limited budgets. Therefore, the practical engineering methods for these purposes, including mathematical preliminaries, are given below.

5.1.1. Pseudo-thermal Light Generation and Statistical Analysis

A rotating scattered medium (e.g., rotating ground glass) illuminated with a laser light can produce a speckle pattern (Diament and Teich, 1970). This pattern results from the interference of diffusely transmitted light, which alternates between constructive and

destructive interference across various spatial areas. (Lib and Bromberg, 2022). The light emanating from this setup is referred to as pseudo-thermal because its coherence characteristics resemble those of true thermal light sources such as a Light Emitting Diodes (LEDs) (Pieper et al., 2018). It has chaotic statistics where correlation time can be adjusted according to the parameters such as rotating speed of medium and beam waist of laser light (Gatti et al., 2006). To investigate the photon number statistics and coherence properties of thermal sources by relaxing coherence time problem in the detection, the pseudo-thermal source concept was introduced (Ahmad et al., 2019). By doing so, fluctuations in light intensity can be directly measured using detectors. Analyzing the time series representing intensity, facilitated by the extended or long coherence time (Kuusela, 2017), allows for the determination of photon statistics through numerical methods. The obtained counting results, which is in terms of intensity values, can also serve as an indication of the bunching phenomenon of light, where groups of photons moving together cause pronounced fluctuations in intensity.

The general overview of pseudo-thermal light generation and its detection with a detector array, which is CCD camera in our case, is given in Figure 5.1. The model based on the generation of scattered light while laser light traversing to the rotating scattering medium (RSM) such as rotating ground glass (RGG). Since the medium contains randomly distributed large number of scatterers (or granules) due to the number of surface details, they produce speckles from the input field having N_p photons. Therefore, we mainly interested in the analysis of randomly distributed N_p photons on K pixels. In our scheme, n_ρ represents the recorded photon counts at pixel ρ in frame k with equal probabilities. n_ρ satisfy the energy conservation $\sum_\rho n_\rho = N_p$ which corresponds conservation constraint of total photon count. The total number of combinations on the detector array can simply be written according to the Binomial distribution (Landau and Lifshitz, 2013):

$$C := \binom{N_p + K - 1}{K - 1} = \frac{(N_p + K - 1)!}{(K-1)!(N_p)!} \tag{5.1}$$

The probability that n photons are received by a single pixel can be written using that how $N_p - n$ photons are distributed the rest of $K - 1$ pixels:

$$P_n^{(N_p)} = \frac{1}{C}\binom{N_p - n + K - 2}{K - 2} \qquad for \quad 0 \leq n \leq N_p \tag{5.2}$$

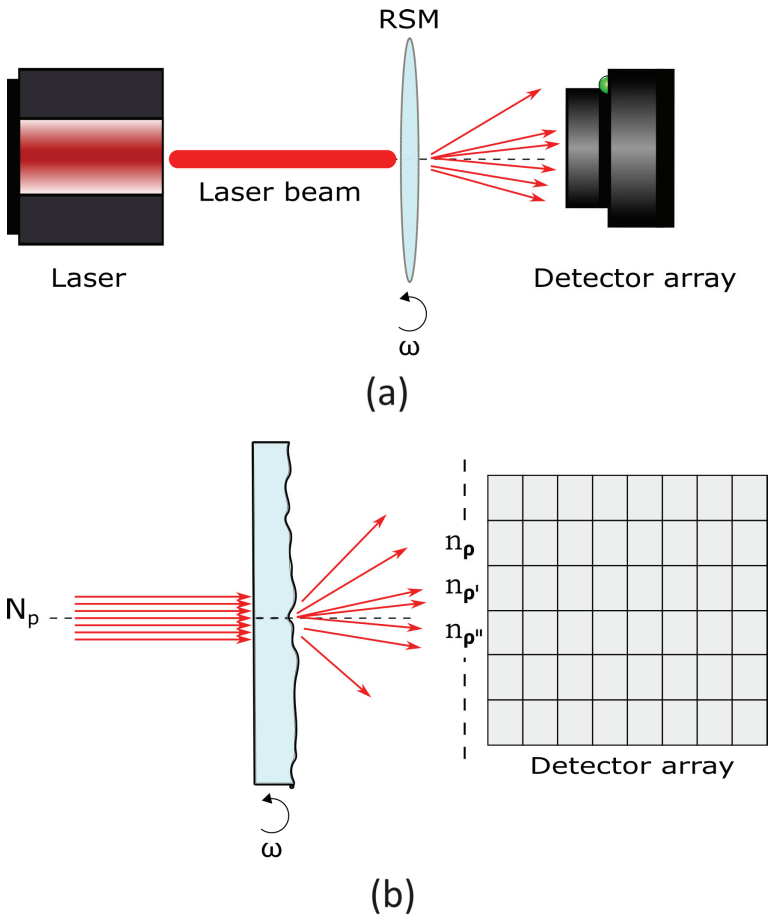

Figure 5.1. (a) Pseudo-thermal light generated by rotating scattered medium and its detection with a detector array (b) A typical demonstration of detection process

Then, the probability is written for $n \ll N_p$ condition as:

$$\begin{aligned}\frac{P_{n+1}^{(N_p)}}{P_n^{(N_p)}} &= \frac{(N_p-n+K-3)!}{(K-2)!(N_p-n-1)!}\frac{(K-2)!(N_p-n)!}{(N_p-n+K-2)!} \\ &= \frac{\cancel{(N_p-n+K-3)!}}{\cancel{(K-2)!}\cancel{(N_p-n-1)}}\frac{\cancel{(K-2)!}(N_p-n)\cancel{(N_p-n-1)!}}{(N_p-n+K-2)\cancel{(N_p-n+K-3)!}} \\ &= \frac{N_p-n}{N_p-n+K-2} = \frac{1}{1+\frac{K-2}{N_p-n}} \simeq \frac{1}{1+\frac{K}{N_p}}\end{aligned} \tag{5.3}$$

As seen from the Equation (5.3), the result is constant and smaller than one, which indicates that the statistics obey the thermal distribution by fitting to the exponential function. Therefore, when the total number of the whole scattered photons obey the conservation constraint of photon count, the behavior of quantifying photon numbers acquired

within a confined region inherently provides access to thermal light statistical characteristics. If the incoming light statistics with a certain distribution ($\mathcal{P}_{in}$) to the scattered medium is taken into account such as following a Poisson distribution (i.e. laser light) from the scattering of N photons:

$$P_n = \sum_N \mathcal{P}_{in}(N) P_n^{(N)} \tag{5.4}$$

where the probability ratio between consecutive photon numbers becomes for $n \ll \bar{N}_p$ as (Li et al., 2020):

$$\frac{P_{n+1}^{(\bar{N}_p)}}{P_n^{(\bar{N}_p)}} \simeq \frac{1}{1 + \frac{K}{\bar{N}_p}} \tag{5.5}$$

where $\bar{N}_p$ is the mean photon value of the input light.

5.1.2. Feasibility of Photon Counting with a CCD Camera

A CCD camera, a standard device in scientific imaging, operates by capturing light across its pixel array, converting the accumulated charge to voltage, amplifying it, and generating a digital output reflecting electron counts per pixel. It has high sensitivity and expansive dynamic range (Giles et al., 1998). There are various types, such as intensified CCD (ICCD) and electron-multiplying CCD (EMCCD) (Moomaw, 2007). The CCD's primary advantage lies in its efficient use of large pixel area for light capture, making it particularly versatile in low-light conditions where traditional charge-to-voltage conversion may introduce significant noise. To address this, techniques such as binning, which merges multiple pixels to enhance signal-to-noise ratio (SNR), can be employed during readout. Additionally, integrating a gain register before conversion can amplify electron counts through impact ionization, rendering it an EMCCD, thus further improving performance in low-light environments.

In any given image, noise is an inevitable factor. Despite receiving an equal number of photons on average, individual pixels exhibit variance in their output values, following a Gaussian distribution. The actual measure of a camera's performance lies not in the amplitude of its signal output, but rather in the SNR, which delineates the ratio between the desired signal and the ambient noise level. For the 8-bit quantization, the SNR can be expressed as (Chen et al., 2009):

$$SNR = 20log\frac{255}{\sigma_N} \tag{5.6}$$

where σ_N corresponds to the RMS of the image noise (or the standard deviation of noise). The noise includes all factors, we called them as artefacts, such as read noise, fixed pattern noise and dark current noise. Since the proposed method contains CCD as a main component of novelty, the effect of these artefacts as a DC offset, especially including standard deviation, is required before the experiments where it gives an insight about the feasibility of off-the-shelf CCDs for photon counting and coherence measurements.

Typically, photon counting experiments utilize highly sensitive light detectors functioning at the single photon level alongside electronic counting systems. While these detectors register electron counts that validate the presence of photons in the incoming light, variations in these counts provide valuable information about the statistical characteristics of the photon stream. Nevertheless, an ongoing question is whether events registered by photon counters are an inherent property of the photon statistics or simply a creation of the detection process. Therefore, the experiments should require expensive and high quality of detectors (Dennis, 2012). In the literature, these detectors are usually single photon detectors, on-off detectors or photon number resolving detectors (Kwiat et al., 1993; Takeuchi et al., 1999; Esmaeil Zadeh et al., 2017; Chrapkiewicz, 2014; Jönsson and Björk, 2019). In addition to these devices, after recent advancements, some specific CCD cameras, such that Electron-Multiplying CCDs (EMCCD) and Intensified CCD (ICCD) cameras are used for photon counting and correlation experiments (Smith et al., 2004; Kumar and Marino, 2019; Bolduc et al., 2017; Oemrawsingh et al., 2002). However, this situation should be reconsidered for traditional CCD cameras, which have many advantages such as affordability and easy availability, because CCD cameras are not considered suitable for photon experiments. The main reason is that achieving optimal performance for single-photon scale with ordinary CCDs and mitigating internal noise are cumbersome problems. Nevertheless, a feasibility analysis should be performed based on the type of experiment. Considering the qualification of laboratories particularly in undergraduate level, the realization of statistics experiments with such simple and low-cost device may need practical engineering solutions. Therefore, we tried to implement a more humble measurement technique by combining the statistical analysis of confined area measurements of thermal light with the pseudo-thermal light concept and an ordinary CCD camera.

Coincidence detection is an indispensable measurement technique due to the wide

range applications from classical correlations to the classical correlations (Bennink et al., 2004; Bennink et al., 2002). However, it is known that all coincidence detection methods such as two scanning single-photon detectors, two scanning slits or array of single-photon detectors are suffer from either too much loss of light, or strict alignment requirements with expensive and sophisticated devices, or multiple measurements, which adversely affect the accuracy of measurements (Bhattacharjee et al., 2022). Furthermore, this detection type needs highly precise time synchronization (Unternährer et al., 2016). In the literature, the methods are mainly based on probability algorithms with or without tresholding (Defienne et al., 2018; Reichert et al., 2018) especially for entangled photon pairs. However, although the two-photon detector issue has been solved, the cost and requirement of adequate laboratory environment are still problems. To overcome this challenging task, the CCD camera exposure time as its coincidence circuit can be exploited which provides self-time synchronization and cost-effectiveness for experiments.

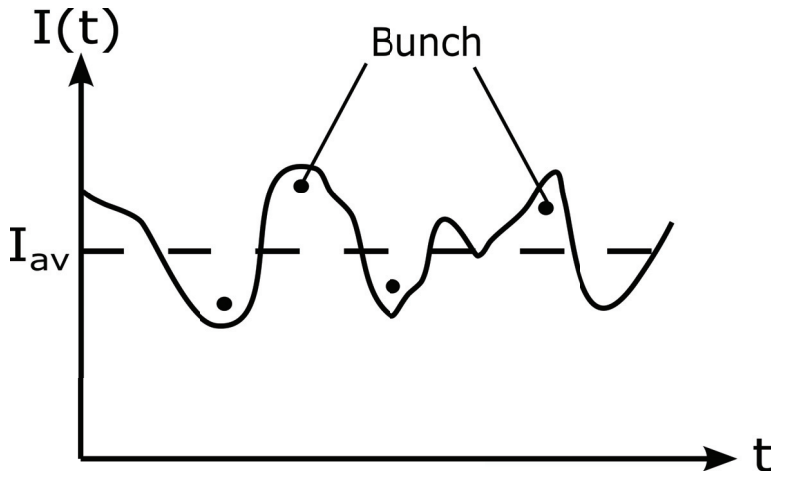

Figure 5.2. Connection between classical fluctuations in intensity around the mean intensity (I_{av}) and photon bunching in a thermal light where photon bunching corresponds to the high intensity fluctuations.

The electron count readings produced by CCD cameras are represented by the intensity values. From the semi-classical standpoint, the probability density of photon counts is related to the intensity of light (see Figure 5.2) (Straka et al., 2018). As we know from the Section 3.3.1, at low intensity values, the relation between probability of photodetection $P(t)$ and detected light intensity $I(t)$ in a short time interval Δt is (Mandel and Wolf, 1995):

$$P(t)\Delta t \sim \eta I(t)\Delta t \tag{5.7}$$

where η represents the quantum efficiency of the CCD camera . Despite the infinitesimally small time intervals involved, the condition remains unfulfilled and detection probability can not be defined in terms of intensity values. Considering that CCDs commonly offer time differentials, Δt, on the order of milliseconds, it becomes imperative to engage in operations within the domain of exceedingly low-intensity values.

Furthermore, the relation between the variance of photocount number $(\Delta N)^2$ and variance of impinging photons $(\Delta n)^2$ on the detector is (Loudon, 2000):

$$(\Delta N)^2 = \eta^2(\Delta n)^2 + \eta(1-\eta)\bar{n} \tag{5.8}$$

where $\bar{n}$ is the mean number. As seen from the Equation (5.8), minimum quantum efficiency of detector should be at around 50% to detect intensity fluctuations. If we investigate the cases for η:

- For $\eta = 1$, the fluctuations in photocounts faithfully mirror the variations in the incoming photon stream.
- For $\eta \ll 1$, the fluctuations in photocounts converge towards a Poissonian outcome due to the averaging.
- If the incident light shows Poissonian statistics, which means that $(\Delta n)^2 = \bar{n}$, the statistical characteristics of photocounts consistently yield a Poisson distribution independent from the η.

Therefore, one may conclude that accurate photon statistics measurement mandates the utilization of high-efficiency detectors since in the regime of exceedingly low efficiencies, the interval between photoelectrons would exhibit complete randomness, resulting in Poissonian counting statistics across all potential incoming distributions. With such detectors in place, photocount statistics offer a genuine assessment of the incoming photon statistics, showcasing an enhanced fidelity that correlates with the heightened efficiency of the detector. In Figure 5.3, it has been demonstrated that quantum efficiency of commercially available standart CCDs are at around %50. Since their η value in only around half ot the ideal value one, it can be inferred that conventional CCDs may be

used to extract approximate photon statistics and coherence function measurements over intensity values.

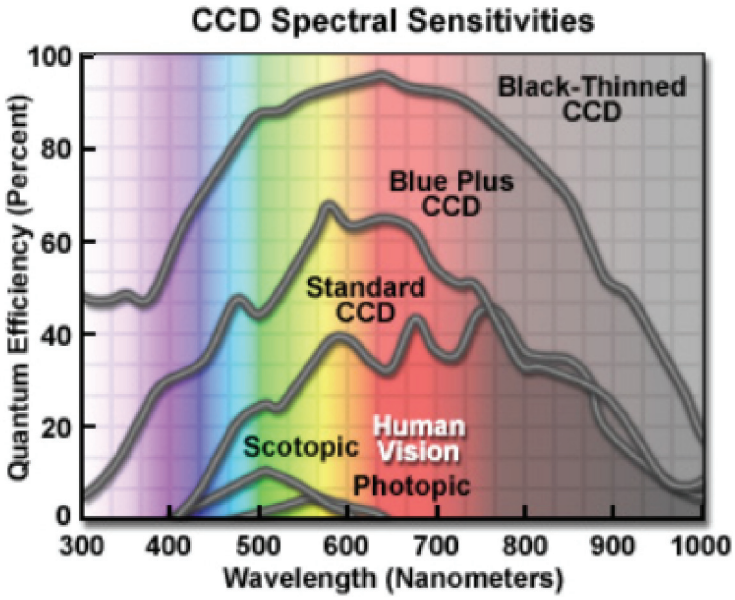

Figure 5.3. A typical spectral sensitivity curve for commercially available CCDs (Photonics)

5.2. Experimental Setup and Measurement Results

Test benches for the proof of concept experiments (see Figure 5.4) were constructed for the investigation of the photon number statistics and coherence of two optical sources: pseudo-thermal and coherent. The $632.8\ nm$ single mode He-Ne laser having $1.5\ mW$ power was used in the experiments as the coherent light source. The neutral-density filters were used to obtain very faint light, decreasing the power of the input field. In the detection part, the SONY XC-711 series CCD camera having $40\ ms$ exposure time was used. The camera also has 768 (H) $\times$ 493 (V) pixels with 17 (H) μm $\times$ 11 (V) μm pixel size. For the generation of pseudo-thermal light, the rotator combined with scattering medium having $4\ Hz$ to $3.7\ kHz$ frequencies was exploited. For the photon statistics and coherence analysis, 10000 frames were recorded for each experiment. Furthermore, for the comparisons, the experiment results were fitted to the numerical calculations and the radius of errors were calculated.

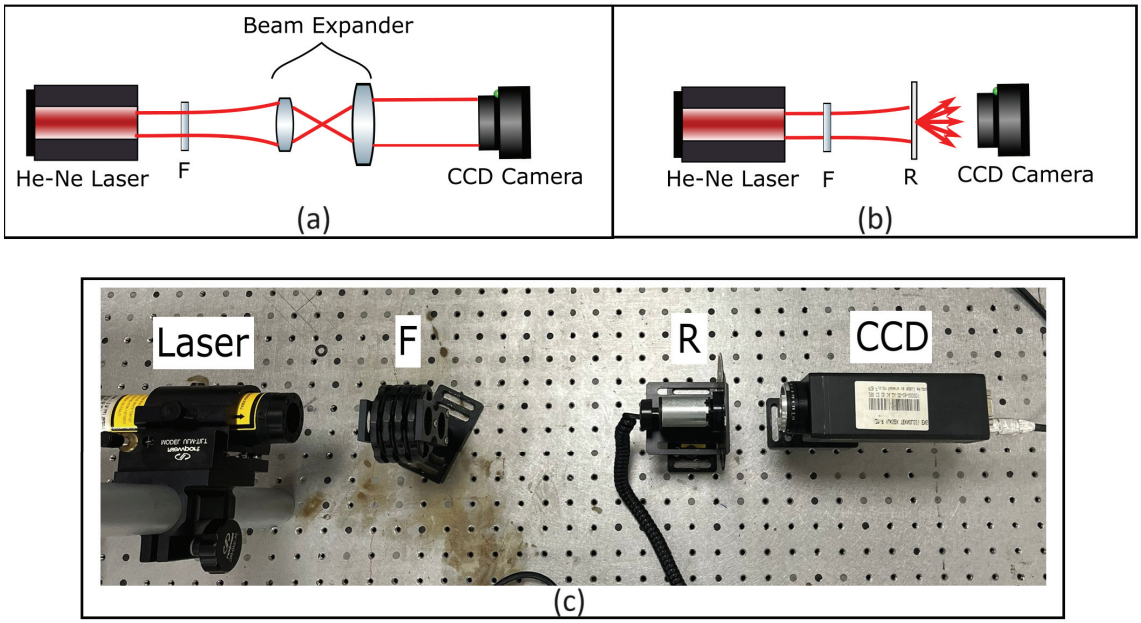

Figure 5.4. (a) Coherent light scheme (b) Pseudo-thermal light scheme where F is neutral density filter to obtain very faint light; R is a rotating diffuser. (c) An experiment photo for pseudo-thermal light measurements

For the experimental measurements and calculations, the coherence time of pseudo-thermal light must be known. In the literature, it has been shown that the coherence time of a source obtained via Gaussian beam with the limit of very many scatterers is given as (Kuusela, 2017):

$$t_c = \frac{W_0}{\upsilon\sqrt{(1+D/L)^2+y^2}} \tag{5.9}$$

where W_0 is the minimum beam waist, υ is the velocity of diffuser at the center of the laser spot, D is the distance between laser and glass and L is the distance between scattered medium and detector. Also the parameter $y = \frac{kW_0}{2L}$ with wavenumber of the laser k. With the help of Equation. (5.9), the coherence time of the pseudo-thermal field can be adjusted, which is extremely important for light sources having the Bose-Einstein and super-Poisson photon statistics. In experiments, the distances D and L is taken as 45 cm and 8 cm, respectively. To receive all scattered light, the rotator is placed close to the CCD. The pseudo-thermal light experiments were realized with rotator frequency $f_r = 25$ Hz, which approximately corresponds to the $t_c = 3\ \mu s$.

5.2.1. Photon Statistics Measurements

The general overview of the photon statistics measurement schemes and an experimental setup photo is given in Figure 5.4. The coherent case is realized with a nearly uniform plane wave obtained via a beam expander. For the pseudo-thermal case, the primary coherence time in experiments is determined as $t_c = 3\ \mu s$. For the comparisons, we also investigate the effect of coherence time on the proposed system by adjusting the coherence time as $t_c = 68\ ns$. At the beginning of experiments, the feasibility of the CCD, including noise floor needs to be examined. We realized two experiments with two different gain (G) levels of CCD, G=1000 and G=0, respectively. In a light-deprived environment, the frames are recorded to calculate the average DC offset on the pixels. The average standard deviations of background offset (σ_N) are computed individually for each pixel. These results correspond to the noise floor, such as electronic noise due to the inherent nature of CCD and compression noise while obtaining frame photos, which cause a DC offset to the frames. It has been found that $\sigma_N = 1.7315$ and $\sigma_N = 0.4701$ for G=1000 and G=0, respectively. The experimental image photo and its standard deviation analysis are given in Figure 5.5. The average intensity for G=0 is $\bar{I}_N = 0.3057$ (in video recording, it reaches 5.27), which offsets our results. Since the faint light condition is required for photon counting experiments where intensity levels (red channel is used) are at about 2 or 3 on average, the CCD experiments with zero gain should introduce fair results.

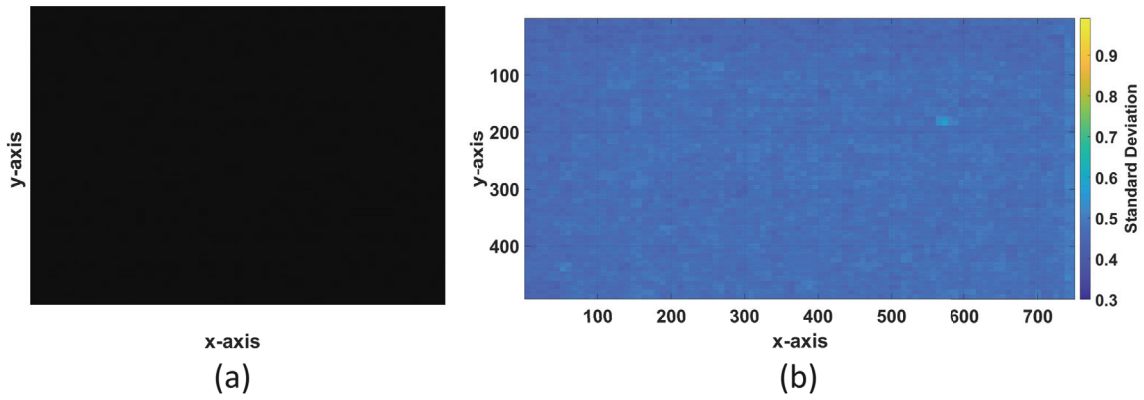

Figure 5.5. Experimental noise floor photo from a frame (b) Standard deviation (σ_N) of CCD camera pixels in the average (G=0)

The intensity values presented in the results (both coherent and pseudo-thermal

cases) are DC offset subtracted intensity values, a necessary step to preserve accuracy during variance computation, as large mean values can lead to significant loss of precision (Chan et al., 1983). It involves shifting the data by an estimated mean, prior to variance calculations (Higham, 2002). Additionally, when intensity recordings are affected by a DC offset caused by noise sources such as photon noise, dark noise, read noise or compression algorithms, the ratio between mean and variance deviates from the ideal distribution, which is crucial for accurately extracting photon statistics (Fox, 2006). To address this, the DC offset across all pixels throughout the frames is computed from the recorded frames in a light-deprived laboratory environment and subtracted from each pixel in every frame. This procedure ensures that photon counts reflect the source more accurately. The intensity of a pixel in the frame j is calculated as follows:

$$I_j = I_j - \bar{I}_N \tag{5.10}$$

where $\bar{I}_N$ the mean intensity of DC offset on the CCD array through the all frames. To illustrate the effect of DC offset, let's take a thermal light photon number series with and without DC offset as:

$$A = [5\ 5\ 0\ 1\ 4\ 0\ 6] \rightarrow without\ DC\ offset$$
$$B = [8\ 8\ 3\ 4\ 7\ 3\ 9] \rightarrow with\ DC\ offset$$

When we examine the mean and variance of these vectors, $\bar{I}_A = 3$, $(\Delta I_A)^2 = 6.6667$, $\bar{I}_B = 6$ and $(\Delta I_B)^2 = 6.6667$. Since the Poisson distributions are interpreted according to the their mean and variance ratio, noise is directly affect the distribution. Besides, the second order coherence functions of these vectors are completely different where $g^{(2)}(0) = 1.6349$ for vector A and $g^{(2)}(0) = 1.1587$ for vector B.

To visualize this problem, we also give a numerical simulation example using a Poisson distribution provided in Figure 5.6 as a reference. Initially, we assumed that the distribution in Figure 5.6 (a) is the actual distribution originating from the light source. Then, we observed the influence of DC offset with 1, 5, and 10 intensity values, respectively, on the distribution. As seen from the results, the distributions almost entirely deviate from actual distributions in Figure 5.6 (a) and (b). Therefore, it can be concluded that the noise factors (as a DC component on pixels) strongly influences the distribution and fluctuation results, preventing the accurate distribution and coherence function.

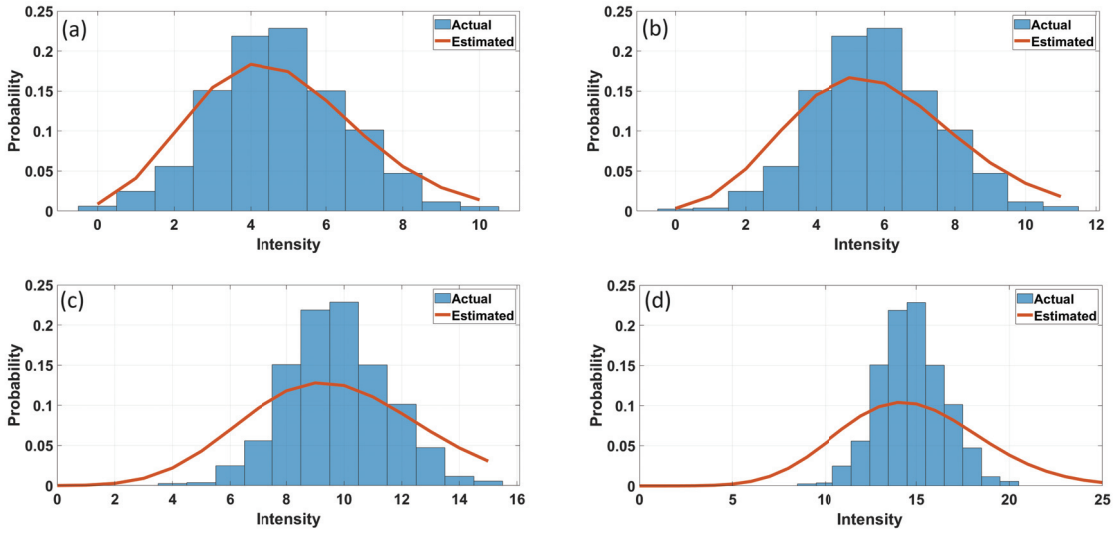

Figure 5.6. Deviation of Poisson distribution due to the DC offset (a) actual: $\bar{I}_{exp} = 4.75$ and $(\Delta I_{exp})^2 = 3.12$ (b) with +1 DC offset: $\bar{I}_{exp} = 5.75$ and $(\Delta I_{exp})^2 = 3.12$ (c) with +5 DC offset: $\bar{I}_{exp} = 9.75$ and $(\Delta I_{exp})^2 = 3.12$ (d) with +10 DC offset: $\bar{I}_{exp} = 14.75$ and $(\Delta I_{exp})^2 = 3.12$

The proposed setup's main goal is to examine thermal light on the pixels of an ordinary CCD array. Before these measurements, we initially examined the photon statistics of coherent light, intending to serve as a reference and benchmark for thermal source outcomes. The normalized histogram of the detected intensity numbers can be constructed by gathering sufficient measurements to represent the photon number distribution. We also realized coherent light experiments in two different gain levels to show the effect of noise on measurement accuracy and precision. For a fair comparison with the pseudo-thermal light source, we studied confined areas represented by the CCD pixels. At G=1000, the photon statistics of four different pixels through a cross-section of the CCD are given in Figure 5.7. Pixels have been selected from the CCD's sides and center through a cross-section. The experimental intensity number distribution outcomes show the Poisson distribution. Although there are small fluctuations in the mean ($\bar{I}_{exp}$) and variance $(\Delta I_{exp})^2$ of intensity values, which corresponds to red channel intensity in RGB values, they are approximately equal to each other which obey the Poisson distribution property. However, it can be seen that the mean number is not constant and shows a great discrepancy between pixels. From the theoretical framework, this is not possible with conventional CCD cameras due to the long exposure time, which causes time averaging. The main reason for observing this situation is the standard deviation of noise floor, which causes DC offset with variance due to the detector's high gain adjustment. Since we study with

very faint light levels, it substantially affects the distribution of mean intensity and leads to deviations that should not occur.

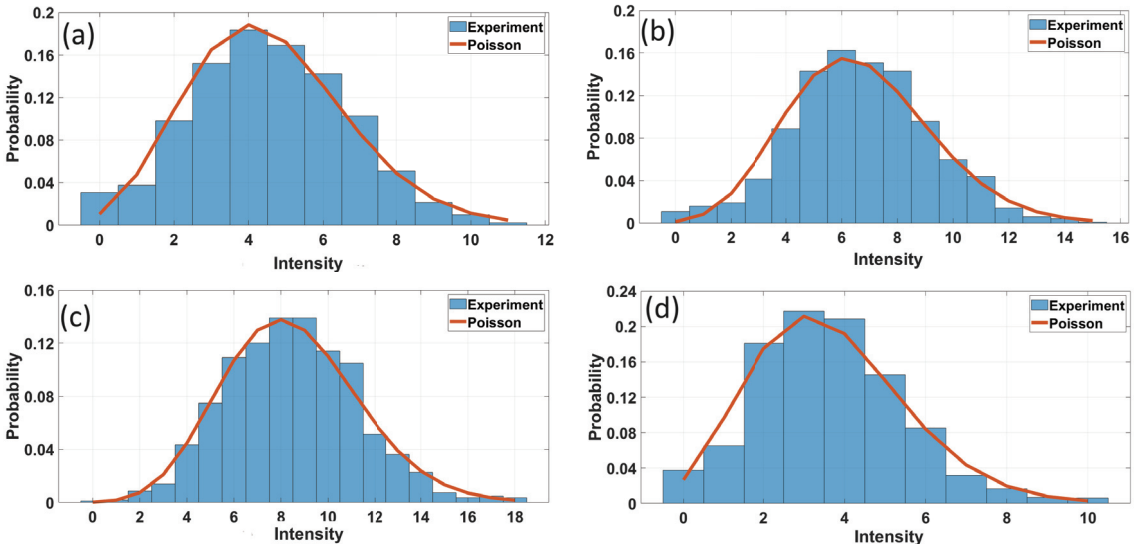

Figure 5.7. Intensity distribution of laser light through a cross-section (G=1000) (a) pixel-1: $\bar{I}_{exp} = 4.57$ and $(\Delta I_{exp})^2 = 4.54$ (b) pixel-2: $\bar{I}_{exp} = 6.69$ and $(\Delta I_{exp})^2 = 6.32$ (c) pixel-3: $\bar{I}_{exp} = 8.48$ and $(\Delta I_{exp})^2 = 7.98$ (d) pixel-4: $\bar{I}_{exp} = 3.62$ and $(\Delta I_{exp})^2 = 3.41$

At G=0, the photon statistics of four different pixels through a cross-section of the CCD are given in Figure 5.8. Again, the pixels have been selected both from the sides and the center of the CCD. The results demonstrate that the intensity histograms converge to the sub-Poisson distribution due to the time averaging as expected. This constant intensity proves that the fluctuations coming from the noise floor are negligible because its effect on the variance of distribution is so weak as given in Figure 5.8. The $(\Delta I_{exp})^2/\bar{I}_{exp}$ ratio on the CCD pixels is given in Figure 5.9. The average mean of the pixels is around 3. The constant intensity value between frames can be observed with a fractional variance on all the pixels of the CCD, as shown in the figures. 96.11% of the pixels exhibit a ratio smaller than 0.15, which is a strong indication of uniform sub-Poisson distribution over the detector array. The negligible deviations between sub-Poisson distribution and experimental results are due to the utilization of an imperfect detector, non-uniformity of plane wave at some regions and loss factor through optical path. For the investigation of pseudo-thermal source in the next part, these results are used as a reference and benchmark.

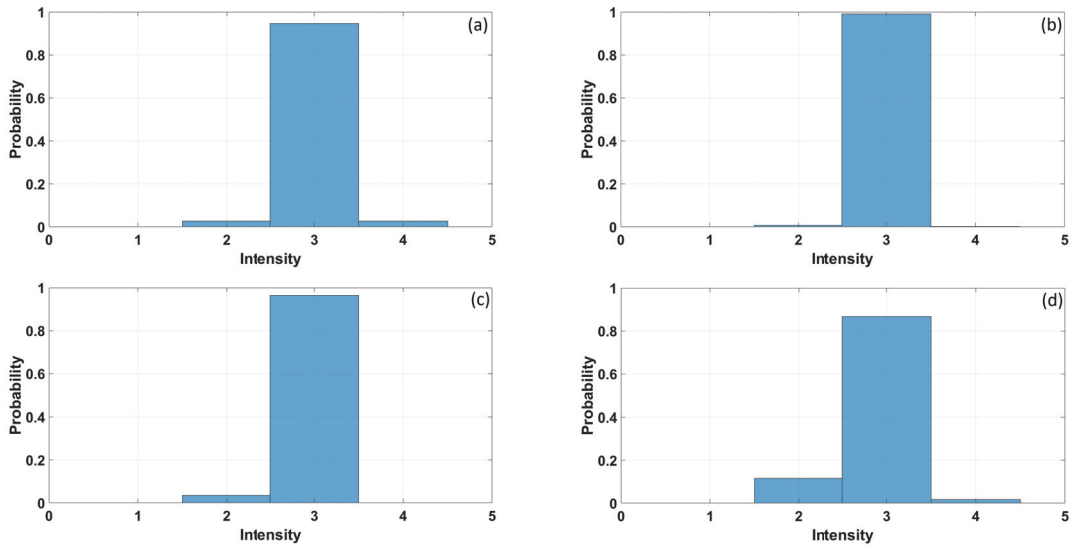

Figure 5.8. Intensity distribution of laser light through a cross-section (G=0) (a) pixel-1: $\bar{I}_{exp} = 3.00$ and $(\Delta I_{exp})^2 = 0.05$ (b) pixel-2: $\bar{I}_{exp} = 2.99$ and $(\Delta I_{exp})^2 = 0.009$ (c) pixel-3: $\bar{I}_{exp} = 2.96$ and $(\Delta I_{exp})^2 = 0.03$ (d) pixel-4: $\bar{I}_{exp} = 2.90$ and $(\Delta I_{exp})^2 = 0.12$

In the second part, we analyze the outcomes of pseudo-thermal light experiments. We have shown that the bunching phenomenon is observed even though CCD's exposure time is much higher than the coherence time of light. The coherence time of light is adjusted to $t_c = 3\ \mu s$. The average mean and the variance of the pixels are around 2 and 3.75, respectively. Therefore, the calculated $(\Delta I_{exp})^2/\bar{I}_{exp}$ ratio is approximately 1.85. The distribution of ratio is given in Figure 5.10. The results reveal that 96.32% of the pixels exhibit a ratio greater than 1.5. However, it can be seen that the statistical behavior of pixels is different from each other on the contrary to coherent case. The ratio mainly indicates the bunching phenomenon of thermal light since a bunch of photons moving together in groups causes high-intensity fluctuations, so the distribution has large variance values. According to the measurements, the pixels with small intensity values, or small number of photons, can be closely approximated by a Bose-Einstein distribution as expected from the Equation 5.5. Four different single-pixels results obeying the Bose-Einstein distribution are given in Figure 5.11. The pixels have been different sides of the CCD according to the mean intensity values of pixels. They agree with the theoretical Bose-Einstein distribution.

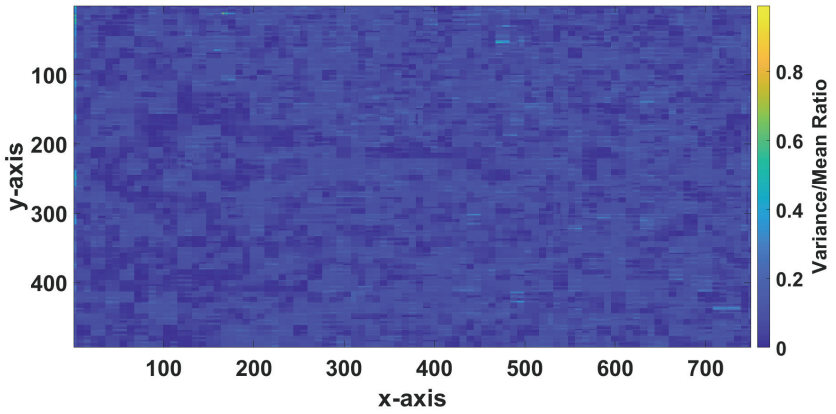

Figure 5.9. $(\Delta I_{exp})^2/\bar{I}_{exp}$ on the CCD camera pixels for laser light (G=0)

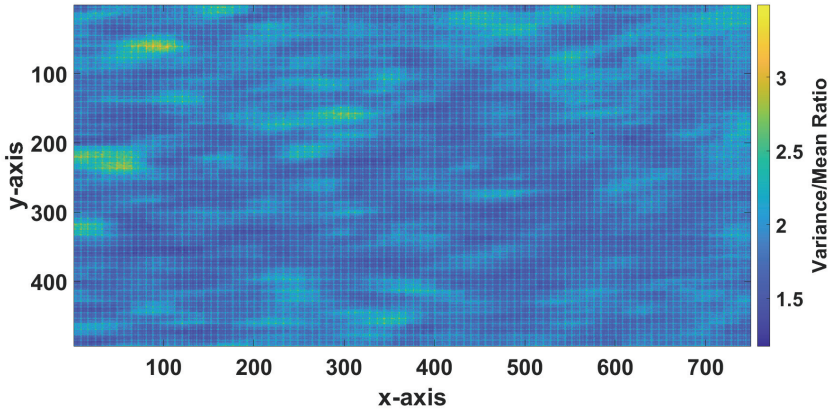

Figure 5.10. $(\Delta I_{exp})^2/\bar{I}_{exp}$ on the CCD camera pixels for thermal light ($t_c = 3\ \mu s$)

On the other hand, as the mean value increases, which means that more photons fall to the pixel in the average, the expectation is that the distribution starts to evolve from Bose-Einstein to the Poisson distribution. These deviations are observed in the pixels with a high mean number especially having mean intensity value above 2.5. Although the distribution deviates from the Bose-Einstein distribution, it has still large variance values which indicates the super-Poisson distribution. The intensity distributions of two diverged pixels are given in Figure 5.12. Figure 5.12 (a), while bearing similarity to the Bose-Einstein distribution, contains radius of errors especially in 1 and 2 intensity values. However, Figure 5.12 (b) is almost entirely deviant. Therefore, it can be stated that obtaining a reliable thermal light distribution for values where the mean intensity exceeds number 3 (cutting edge) may be problematic in standard CCDs.

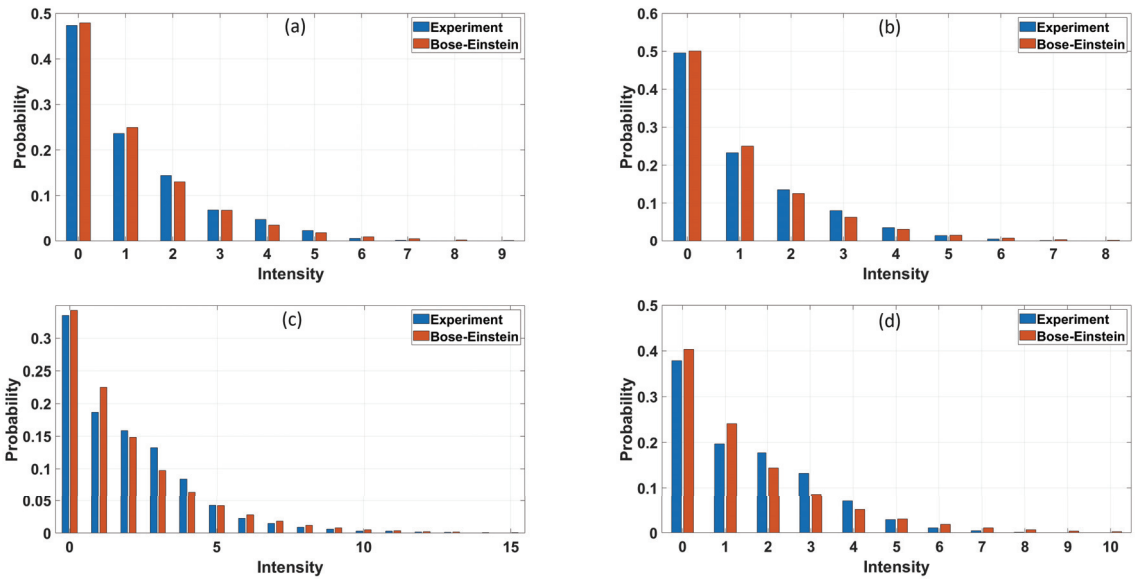

Figure 5.11. Intensity distribution of pixels obeying Bose-Einstein distribution (a) pixel-1: $\bar{I}_{exp} = 1.08$ and $(\Delta I_{exp})^2 = 1.9215$ (b) pixel-2: $\bar{I}_{exp} = 0.99$ and $(\Delta I_{exp})^2 = 1.68$ (c) pixel-3: $\bar{I}_{exp} = 1.91$ and $(\Delta I_{exp})^2 = 4.55$ (d) pixel-4: $\bar{I}_{exp} = 1.47$ and $(\Delta I_{exp})^2 = 2.45$

The outcomes have proven that although the coherent light shows the same Poisson distribution statistics in every pixel, the behavior is not the same for the thermal source, which indicates that Bose-Einstein and super-Poisson statistics can be observed with the single pixel analysis of ordinary CCDs. Additionally, considering that the output from the CCD is within the range of 0-255 and our operating range is between 0-3, approximately a 1/100 ratio in intensity values is required for observations to be conducted.

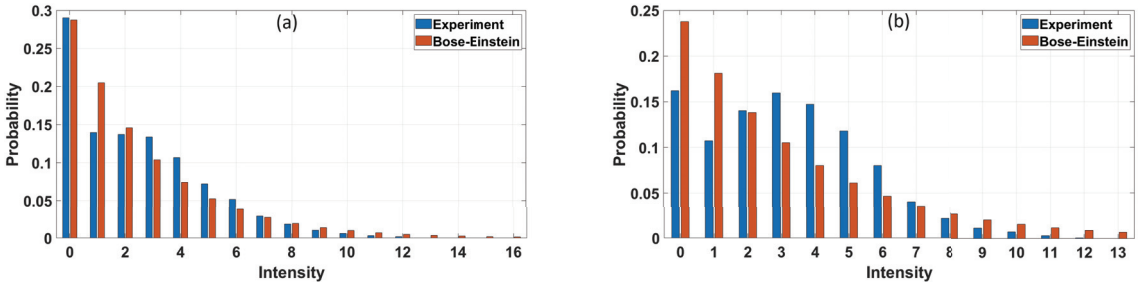

Figure 5.12. Intensity distribution of two deviated pixels from Bose-Einstein to Poisson due to increasing mean intensity value (a) pixel-5: $\bar{I}_{exp} = 2.48$ and $(\Delta I_{exp})^2 = 5.95$ (b) pixel-6: $\bar{I}_{exp} = 3.20$ and $(\Delta I_{exp})^2 = 5.59$

.

We also examine the feasibility of our proposed system for increased rotator speed which corresponds low coherence. Therefore, we make an independent experiment where the diffuser frequency is adjusted to $f_r = 1500$ Hz, which generates pseudo-thermal light having $t_c = 68\ ns$. The mean and variance intensity values are around 1.87 and 2.33, respectively. $(\Delta I_{exp})^2/\bar{I}_{exp}$ ratio is approximately 1.3 as seen from the Figure 5.13. As the previous results, the distributions obey the Bose-Einstein distribution for small number of intensity values. The outcomes indicates that the acquisition of time information from spatial intensity data is applicable for thermal light having very low coherence time which prove that the measurement is valid regardless of the coherence of thermal light.

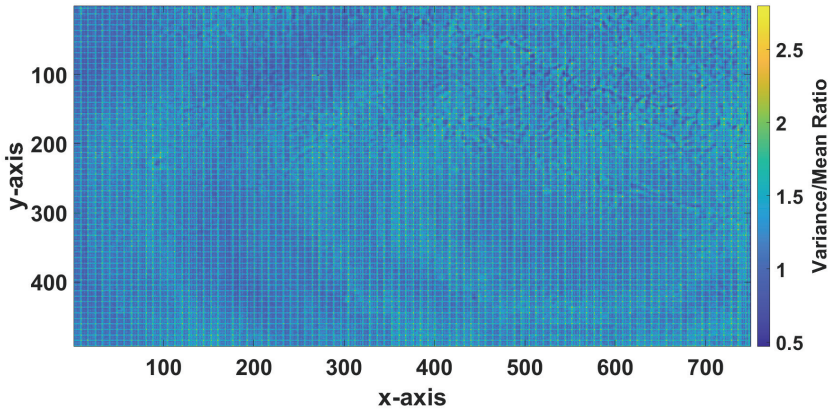

Figure 5.13. $(\Delta I_{exp})^2/\bar{I}_{exp}$ on the CCD camera pixels for thermal light ($t_c = 68\ ns$)

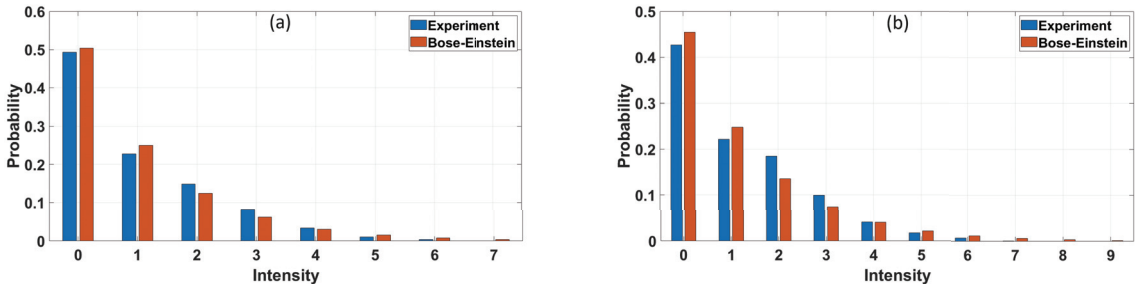

Figure 5.14. Intensity distribution of thermal light ($t_c = 68\ ns$) pixels obeying Bose-Einstein distribution (a) pixel-1: $\bar{I}_{exp} = 0.99$ and $(\Delta I_{exp})^2 = 1.55$ (b) pixel-2: $\bar{I}_{exp} = 1.20$ and $(\Delta I_{exp})^2 = 1.8911$

.

5.2.2. Second Order Coherence Measurements

We start this subsection with coherence length measurements of our coherent source He-Ne laser before temporal and spatial coherence experiments. In this way, we not only verify the coherence degree (both temporal and spatial) of our source but also re-extract the characteristics of this extensively employed light source over the years. For this purpose, we employed a most common interferometric-based method known as Michelson interferometer. It is an amplitude-splitting interferometer conceived by Albert Michelson in 1890, marking him as the first American physicist to be awarded the Nobel Prize (1907) for advancements in optics. Michelson, in collaboration with Morley, employed this interferometer in their renowned sequence of experiments designed to validate the existence of the ether. The experimental setup of Michelson interferometer is given in Figure 5.15. In the configuration, the laser light is directed onto a beam splitter (BS), comprising a glass plate with a partially reflective surface. Approximately 50% of the incident light is reflected, while the remaining 50% is transmitted. The reflected light, denoted as beam 1, encounters mirror M_1, undergoing reflection back towards the beam splitter. Simultaneously, the transmitted light, identified as beam 2, is reflected back towards the beam splitter by movable mirror M_2. Half of the intensity of each reflected beam is transmitted or reflected toward the observation screen. At the screen, the two beams intersect, leading to constructive or destructive interference contingent upon the relative phase shift between the two plane waves. By adjusting the optical path of beam 2 via movable mirror M_2, we can obtain information about coherence of optical source.

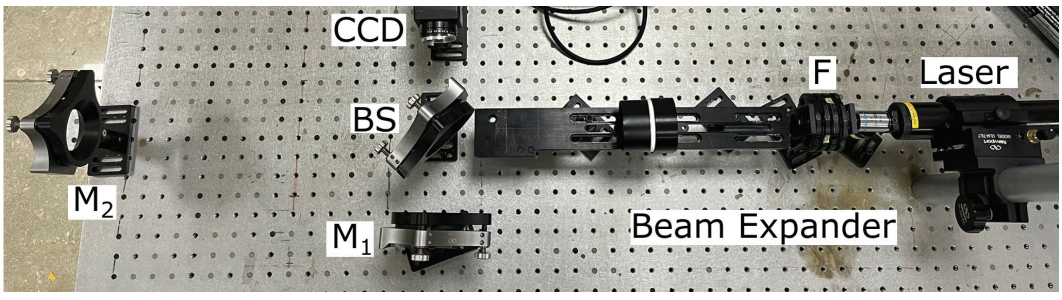

Figure 5.15. Michelson Interferometer setup

Then, we realized coherence function measurements for both temporal and spatial. For the temporal second order correlation function $g^{(2)}(\tau)$ measurements, we used

the setup in Figure 5.4 by leveraging CCD camera frames. For the spatial second order correlation function measurements, the utilized setup for coherent source are given in Figure 5.16. To dispose of the two detectors requirement for the coincidence detection, CCD camera pixels are divided in two parts as it behaves two different detectors having same frame rate. This way, we can also eliminate the time-synchronization problem between detectors in coincidence circuits. Furthermore, for the relaxation coherence time, the two arms are arranged to have approximately same optical path to the CCD camera. The divided light beams fall onto the centers of the first and second portions of the CCD.

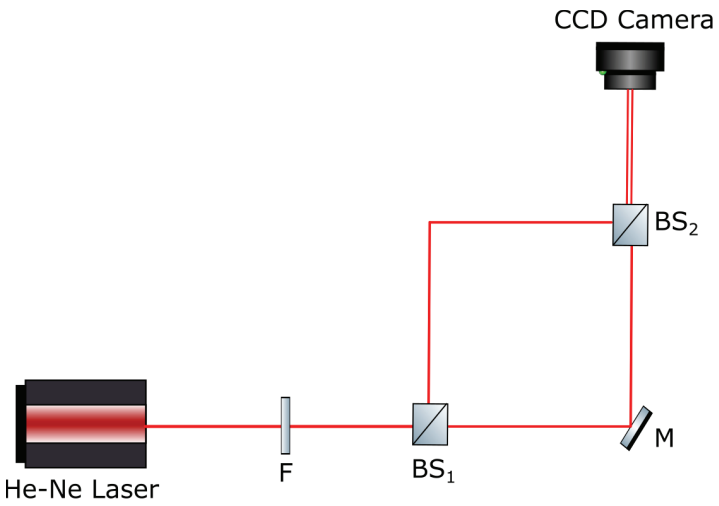

Figure 5.16. The experimental setup for spatial coherence measurement for laser light. F is ND filter to prevent saturation; M is a mirror; BS is beam splitter.

5.2.2.1. Coherence Length Measurements

To find the laser coherence length, we systematically acquired 8 distinct measurements by incrementally distancing from the source. The starting point is 120 cm in our setup due to the fact that beam expander occupy large area. Since the coherence length of a beam of light (l_c) is defined as the maximum difference in path length between two interfering beams such that an interference pattern is still visible, we calculate the visibility of interference pattern for 8 different points according to the Equation (5.11). Recorded interference patterns for two different distances between laser and CCD are given in Figure 5.17. As expected, the visibility decreases with increased optical path.

$$\mathcal{V} = \frac{I_{i(max)} - I_{i(min)}}{I_{i(max)} + I_{i(min)}} \tag{5.11}$$

where $I_{i(max)}$ and $I_{i(min)}$ represent the maximum and minimum value of interfered intensity, respectively.

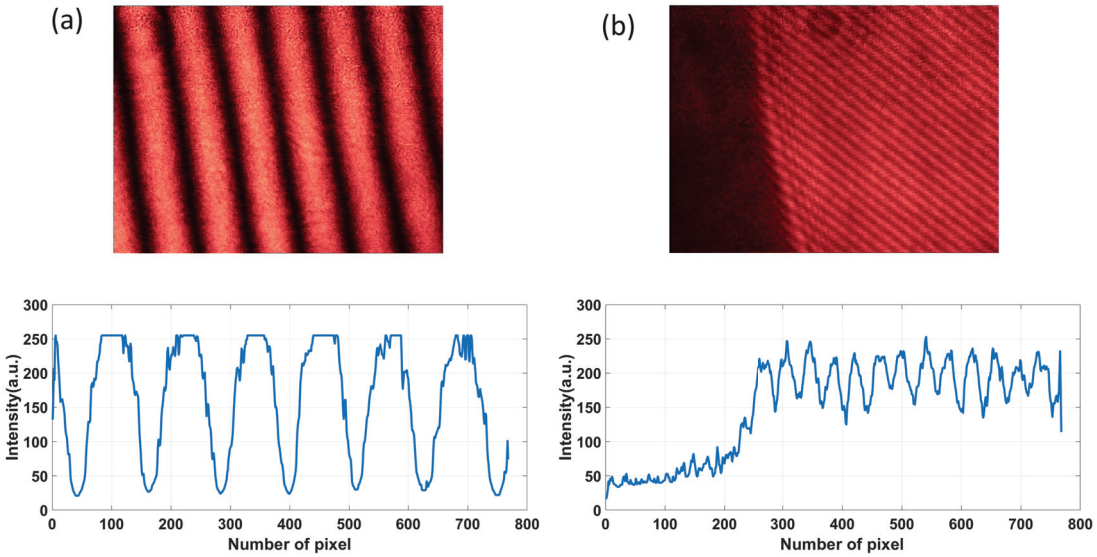

Figure 5.17. Recorded intensity patterns and cross section plots for distance (a) at 120 cm (b) at 530 cm

To obtain the coherence length curve using discrete measurements, we exploit polynomial fitting. The approximated polynomial is given below:

$$p(x) = p_1 x^4 + p_2 x^3 + p_3 x^2 + p_4 x + p_5 \tag{5.12}$$

where $p_1 = -1.031 \times 10^{-9}$, $p_2 = 1.363 \times 10^{-6}$, $p_3 = -4.913 \times 10^{-4}$, $p_4 = -0.06326$, and $p_5 = 98.03$. According to the curve fitting result, the coherence length of the laser is at around 8 m as given in Figure 5.18.

We know that the coherence length depends on the distribution of the frequencies that create the beam. The broader the frequency distribution, the shorter the coherence length. The length of cavity approximately 15 cm for the laser. We extract coherence time (t_c), line-width ($\Delta\lambda$) and spectral width ($\Delta\upsilon$) of the laser. The results reveal that the coherence time, line-width and spectral width of laser is approximately 26.6 ns, 0.05 pm and

36 MHz, respectively. For more detailed formulations and calculations, see (Ackermann and Eichler, 2007).

$$l_c = c\, t_c \tag{5.13}$$

$$t_c = \frac{1}{\Delta \upsilon} \tag{5.14}$$

$$\Delta \upsilon = c\frac{\Delta \lambda}{\lambda^2} \tag{5.15}$$

where c is the speed of light.

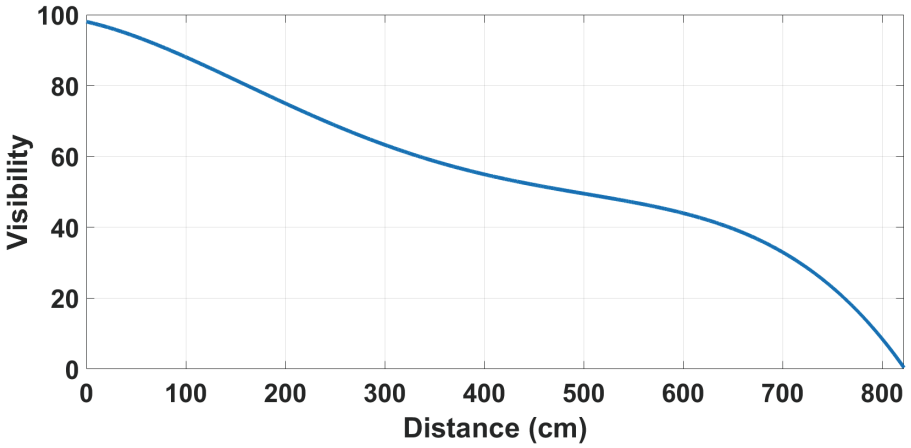

Figure 5.18. Polynomial fitting result for the He-Ne laser coherence length

5.2.2.2. Temporal Coherence Measurements

The second-order temporal correlation function of the light is defined by:

$$g^{(2)}(\tau) = \frac{\langle E^*(t)E^*(t+\tau)E(t+\tau)E(t)\rangle}{\langle E^*(t)E(t)\rangle\langle E^*(t+\tau)E(t+\tau)\rangle} = \frac{\langle I(t)I(t+\tau)\rangle}{\langle I(t)\rangle\langle I(t+\tau)\rangle} \tag{5.16}$$

where $E(t)$ and $I(t)$ are electric field and intensity of light at time t, respectively. Based

on this definition, the $g^{(2)}(\tau)$ describes the correlation between two temporally separated intensity signals with time difference $\tau = t_2 - t_1$ from one light source. Since the number of counts registered on a photoncounting detector is proportional to the intensity according to the Equation (5.7), we can write $g^{(2)}(\tau)$ in terms of photon numbers as:

$$g^{(2)}(\tau) = \frac{\langle n_1(t) n_2(t+\tau) \rangle}{\langle n_1(t) \rangle \langle n_2(t+\tau) \rangle} \tag{5.17}$$

where $n_i(t)$ represents the number of counts registered on detector i at time t. If the analysis is made between single detector frames, there is no need to sub-index i (as in our case). Also $\langle \cdot \rangle$ designates the statistical averaging that is done over a large ensemble of different realizations of the input field.

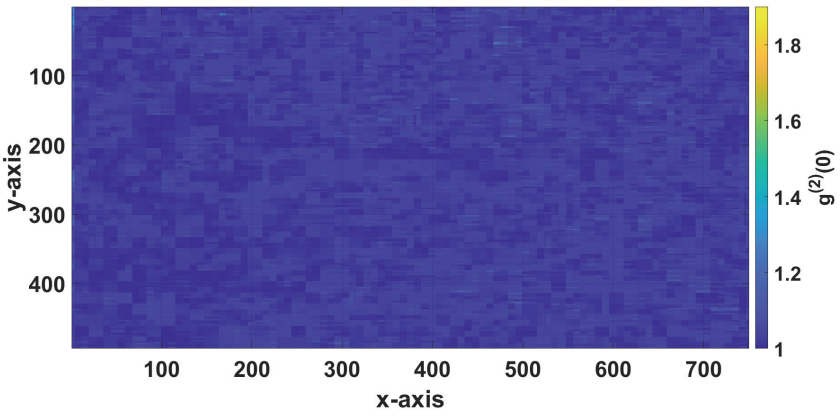

Figure 5.19. $g^{(2)}(0)$ result on the CCD camera pixels for coherent light

In part 5.2.1, we have demonstrated the pseudo-thermal light photon statistics by examining the single pixels of the CCD camera. We have seen that although most of pixels reveal thermal distribution behavior while some pixels do not due to the mean intensity value of pixels. However, the distribution is the same for nearly all pixels in the coherent source case. In this part, same recorded frames in the previous sections are examined by the normalized second order temporal correlation function $g^{(2)}(\tau)$ perspective. This way, not only we can make validation about the statistics of light source but also we try to establish a relationship between two different evaluation criterion. Through the measurements, the exposure time of the CCD is used as the time difference τ, which indicates that we scrutinize the correlation between frames. In order to conduct a fair

assessment, camera pixels with extracted photon statistics were examined in terms of $g^{(2)}(\tau)$. The experiments are realized for both coherent and thermal light.

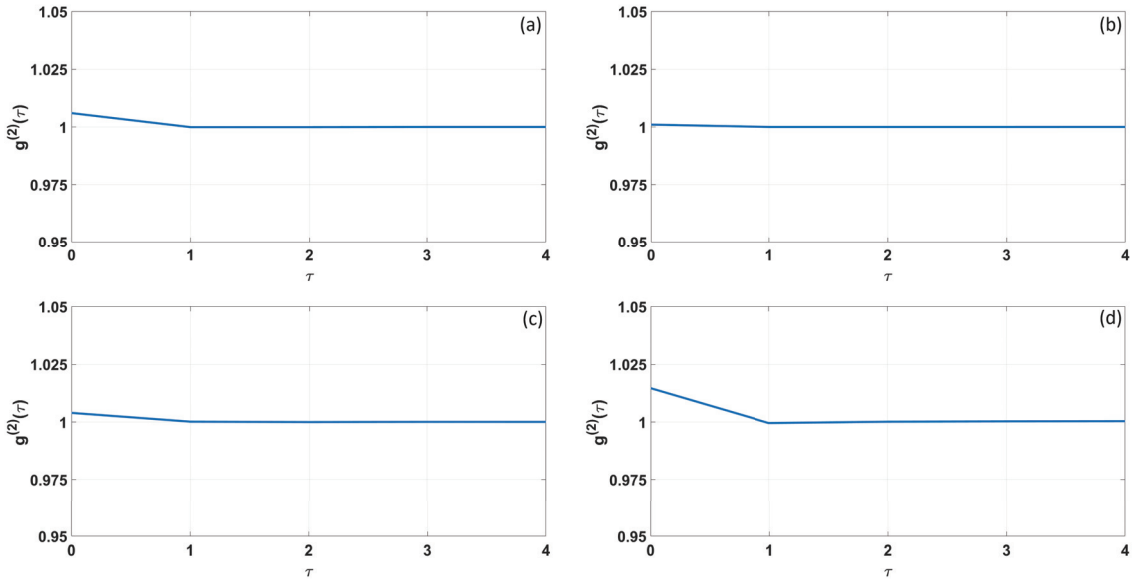

Figure 5.20. Coherent light $g^{(2)}(\tau)$ results for four different pixels on the CCD camera. τ is in terms of the frame number.

$g^{(2)}(\tau)$ of coherent light on the CCD array and selected four pixel results are given in Figure 5.19 and 5.20, respectively. According to the coherent light outcomes, $g^{(2)}(0)$ starts with a value close to the 1 and shows negligible fluctuations at around 1 which obey the theory (see Figure 1.9). This attitude is valid for almost all pixel as photon statistics analysis of coherent light. 93.04% of the pixels have $g^{(2)}(0)$ between 1 and 1.05. The percentage reaches 99.9% for the range between 1 and 1.1. The average $g^{(2)}(0)$ of all pixels is 1.0207. Since the selected pixels are the same with photon statistics part, it can be concluded that the pixel having large variance (as in Figure 5.8 (d)) also has slightly high $g^{(2)}(0)$ value which corresponds approximately 1.014.

For the thermal light $g^{(2)}(0)$ measurements, we use the main idea which is the distribution of time-bin information to the spatial information as mentioned in previous sections. As the frequency of multiphoton events rises, the temporal gap between successive photon arrivals contracts relative to the prescribed sampling duration. Alternatively expressed, the sampling duration extends beyond the coherence time of the emitted photons. When we examine the pseudo-thermal light results, all pixels have distinct characteristics similar to photon statistics results. $g^{(2)}(\tau)$ of thermal light on the CCD array and selected

four pixel results are given in Figure 5.21 and 5.22, respectively. The average $g^{(2)}(0)$ of all pixels is 1.7264. This outcome indicates thermal light and bunching phenomenon As the mean intensity value increases further, the distribution gets closer to the Poisson distribution. For the pixel obeying Bose-Einstein distribution, as expected (Guo et al., 2018), $g^{(2)}(\tau)$ decreases gradually to 1 in increasing τ which is determined by exposure time. It can be seen in Figure 5.22, the $g^{(2)}(\tau)$ exhibits a sharp decline with $\tau = 1$.

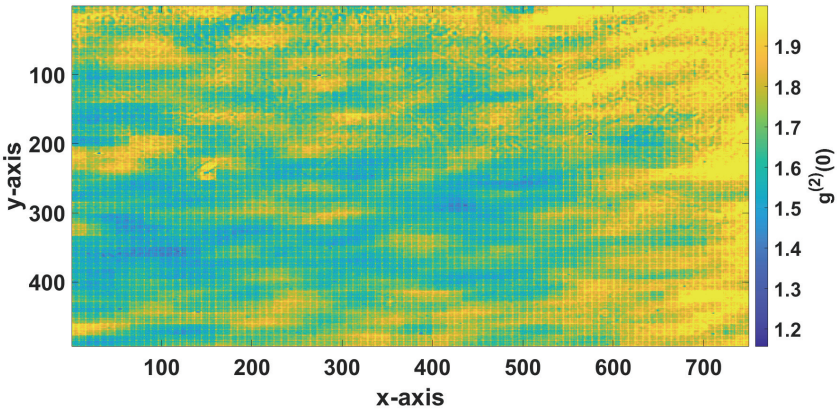

Figure 5.21. $g^{(2)}(0)$ result on the CCD camera pixels for thermal light ($t_c = 3\ \mu s$).

Table 5.1. $g^{(2)}(0)$ classification of thermal light pixels

	>1.5	**>1.6**	**>1.7**	**>1.8**	**>1.9**
$g^{(2)}(0)$	97.68%	82.06%	54.84%	28.29%	11.84%

On the other hand, for the pixel diverging from Bose-Einstein distribution, $g^{(2)}(0)$ starts from 1.5 revealing that source characteristics move away from thermal statistics and goes to the coherent light statistics. This inference can be easily seen from Figure 5.22. Pixels with a larger $g^{(2)}(0)$ exhibit better conformity with Bose-Einstein distribution (for comparison of same pixels see Figure 5.11). Therefore, it can be concluded that although photon statistics and second order correlation function measurements are two different approach for source characterization and have no direct relationship, they are in agreement with each other. On the other hand, there are undesired fluctuations around 1 in the incremental τ values because $g^{(2)}(\tau)$ should one expect τ due to the long exposure

time of the detector. For example, the mean value of $g^{(2)}(1)$ is equal to the 0.998 and 95.22% of the pixels have $g^{(2)}(1)$ between 0.95 and 1.05. These fluctuations may occur due to rotating diffuser granule size, some scattered field diffractions at the sharp edges of CCD and utilization of CCD which can be defined as imperfect detector for statistical measurements.

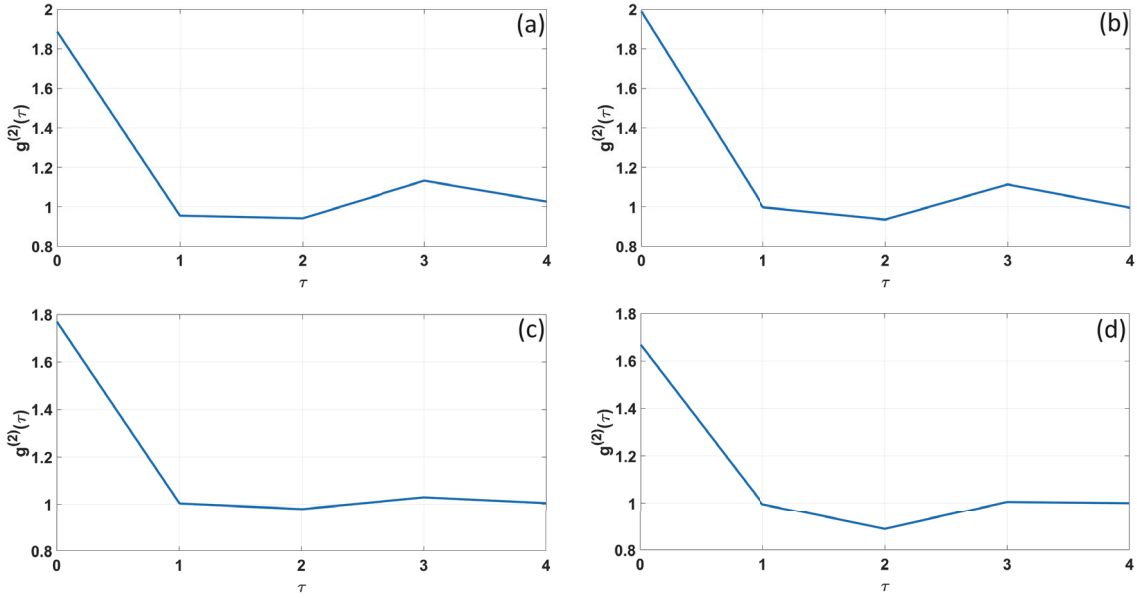

Figure 5.22. Thermal light $g^{(2)}(\tau)$ results for four different pixels on the CCD camera ($t_c = 3\ \mu s$). τ is in terms of the frame number.

We also evaluate the $g^{(2)}(\tau)$ for $\tau_c = 68\ ns$. The $g^{(2)}(0)$ distribution on the CCD array is given in Figure 5.23. Since this is an independent measurement having distinct coherence time, the distribution change completely from the previous thermal light measurements. However, the results indicates same implication. According to the outcomes, $g^{(2)}(0)$ has large values for the intensity distributions obeying the Bose-Einstein distribution, which corresponds a small number of intensity values.

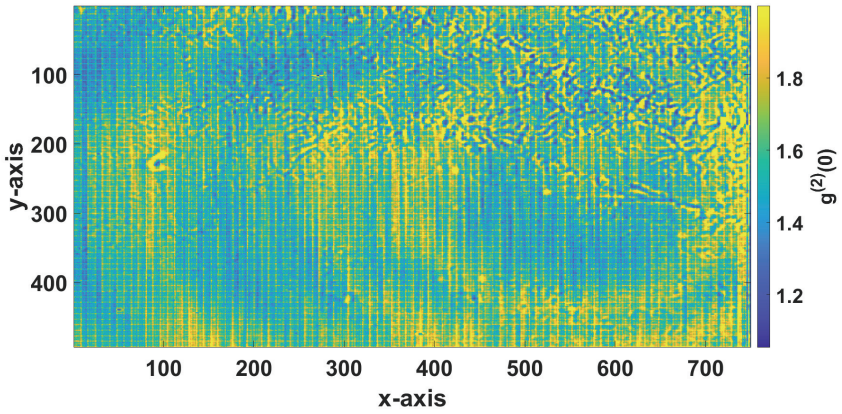

Figure 5.23. $g^{(2)}(0)$ results on the CCD camera pixels for thermal light ($t_c = 68\ ns$)

5.2.2.3. Spatial Coherence Measurements

The second-order spatial correlation function of the light is defined by:

$$g^{(2)}(x_1, x_2) = \frac{\langle E^*(x_1)E^*(x_2)E(x_2)E(x_1)\rangle}{\langle E^*(x_1)E(x_1)\rangle\langle E^*(x_2)E(x_2)\rangle} = \frac{\langle I(x_1)I(x_2)\rangle}{\langle I(x_1)\rangle\langle I(x_2)\rangle} \tag{5.18}$$

where $E(x_j)$ and $I(x_j)$ are electric field and intensity of light at position or pixel i, respectively. Like second order temporal correlation function, we can write $g^{(2)}(x_1, x_2)$ in terms of photon numbers as:

$$g^{(2)}(x_1, x_2) = \frac{\langle n_1(x_1)n_2(x_2)\rangle}{\langle n_1(x_1)\rangle\langle n_2(x_2)\rangle} \tag{5.19}$$

where $n_i(t)$ represents the number of counts registered on detector i at position or pixel x_j.

For spatial coherence experiments, we used experimental setup, which is given in Figure 5.16. The CCD camera sensor area was treated as if there were two separate detectors. We examined the spatial coherence between the light beams directed into two distinct areas. The optical paths were adjusted to be as closely aligned as possible since the requirement of temporal coherence has been relaxed (Zhang et al., 2009). However, it does not seem quite feasible in a non-sophisticated laboratory environment, especially considering the wavelength of light. To show the exact distribution of the light, the recorded

pattern in Figure 5.24 (a) was not taken in very faint light conditions. After this step, the light was attenuated.

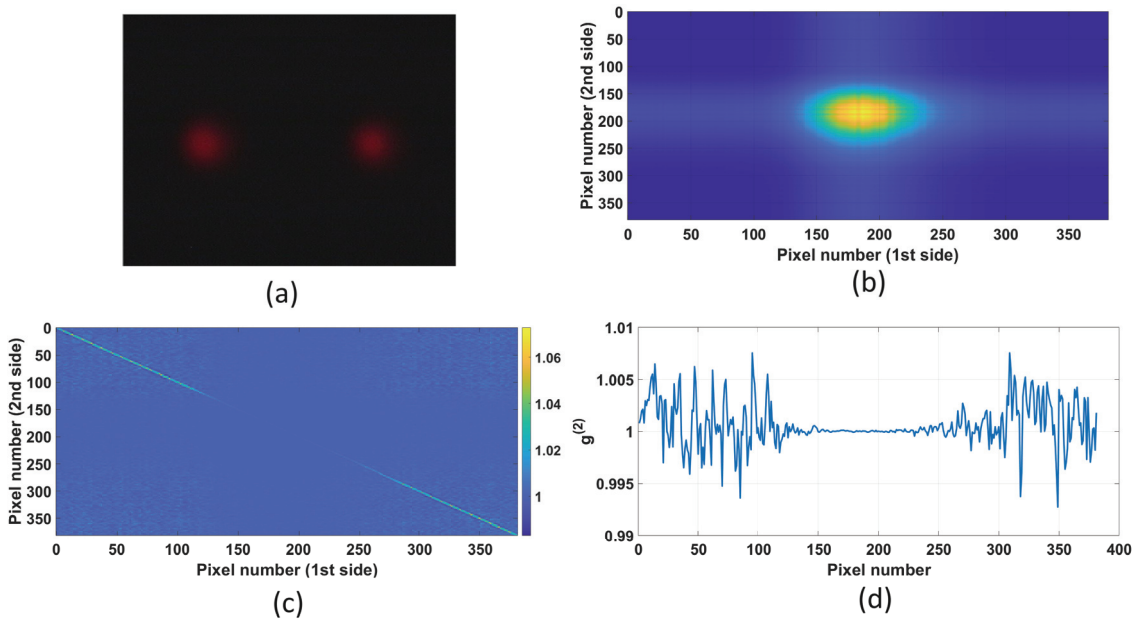

Figure 5.24. Spatial coherence measurements for coherent source (a) Recorded CCD pattern from a frame (b) Joint detection probability between pixels in first and second side of CCD camera (c) Normalized spatial second order correlation function $g^{(2)}(x_i, x_j)$ on the CCD camera pixels (d) Normalized spatial second order correlation function $g^{(2)}(x_i, x_i)$ through the diagonal cross section

The joint detection probability of two beams is given in Figure 5.24 (b). Since both areas have 384 pixels (768/2) horizontally, the probability should take its maximums at around one-fourth of the total number of pixels. Furthermore, the $g^{(2)}(x_1, x_2)$ has very small and negligible fluctuations at around one and become more stable through the center points of the diagonal cross-section as expected (see Figure 5.24 (c) and (d)). The results prove that spatial correlation measurements, especially in extended patterns, CCD cameras are effective solutions.

CHAPTER 6

CONCLUSIONS AND FUTURE WORKS

Within this dissertation, we first present a novel methodology based on the phase diffraction properties of spatially structured entangled photons. This approach is designed to effectively characterize the thickness of nanoscale dielectric films on optical fibers. The proposed method involves tracking photons as rays while disregarding minor decoherence effects resulting from the short optical path length within the phase object, leading to a simplified mathematical model. Notably, we have illustrated that the utilization of transverse spatial correlations significantly enhances the precision in determining film thickness. In the model, spatially entangled photons are integrated with a narrower aperture to achieve confocality, thereby further refining thickness precision. Simulation results indicate that the amplitude ratio reaches 1.2, and zero crossings shift to approximately 70 μm for a 25-nanometer film-coated optical fiber. Despite the low conversion efficiency affecting detector intensity in SPDC, this observable and measurable deviation corresponds to nearly 4 pixels on a 20 μm pixel-size detector array. By assessing these deviations, accurate determination of film thickness becomes feasible. Consequently, the spatial entanglement-based phase diffraction design emerges as a potent technique for characterizing transparent curved dielectric film thickness, particularly up to 25 nm, a critical requirement for various optical fiber sensor applications.

We have also demonstrate an alternative scheme depending on phase diffraction of thermal photons instead of spatially entangled photons. The suggested system provides a cost-effective and practical solution, especially suitable for non-sophisticated conventional laboratories. This enables circumvention of issues such as low generation probabilities of entangled photons and strict laboratory alignment. According to the results, the sole distinction between thermal photons and entangled photons appears to be in terms of visibility. Although it may produce sub-optimal results for detectors with exceedingly high exposure times, minima shifts and amplitude variations are measurable in a sufficient laboratory environment.

As optical coherence and coincidence detection techniques forms an essential in the proposed characterization system, a comprehensive analysis of photon statistics and optical coherence is undertaken through the introducing an innovative and straightforward measurement procedure for thermal light characterization. The proof-of-concept exper-

imental design is constructed to extract photon number statistics and second degree of coherence of thermal light sources by leveraging single pixel measurements through a CCD camera. The semi-classical approach is used in the analysis which provides simple and practical model. Before the experiments, a comprehensive feasibility analysis of CCD was conducted. Coherent source is also examined to serve a reference for thermal source outcomes. In light of the photon statistics outcomes, it is evident that the Bose-Einstein statistics associated with scattered light can be extracted by scrutinizing individual pixel intensity values, notwithstanding the extended exposure time of the detector. The results reveal that as the mean photon number increases, the photon number distribution showcases a transition from a Bose-Einstein distribution to a Poisson distribution. Subsequently, we examine and evaluate both temporal and spatial second-order coherence function measurements. The exposure time of the CCD is exploited time difference in temporal $g^{(2)}(\tau)$ measurements. While the cameras exposure is used as an internal coincidence circuit in temporal coherence measurements, the sensor area of the CCD camera is treated as though it comprised two distinct detectors in spatial coherence experiments. At small intensities, the degree of temporal coherence is well above reference coherent case value. These results are the clear signature of thermal light. Hence, Bose-Einstein distribution and bunch light phenomenon can be observed over the pixel intensity values of CCD which is a conventional, non-sophisticated commercially available detector.

For the future works, the N-fold detection scheme may be integrated to the characterization system to increase the thickness resolution since the studies have been proven that the maximally entangled multiphoton entangled states (NOON) acquire N times sensitivity to the system (Mitchell et al., 2004; Afek et al., 2010). Superradiance (Oppel et al., 2014) or multiphoton interference phenomena (Oppel et al., 2012) can also be used in the system model. Besides, it is known that the coherence properties of pump affect the biphoton wavefunction directly (Cui et al., 2024; Defienne and Gigan, 2019; Boucher et al., 2021). Therefore, tunable control of spatial correlations between photon pairs produced by SPDC can be considered a topic worthy of investigation. At last, the identification of nanoscale thickness in dielectric films can pose challenges due to the inadequacy and prolonged nature of classical curve matching algorithms. Neural network and signal processing algorithms (Ataç et al., 2023; Ataç and Dinleyici, 2023a) may also helpful for thickness classification with relatively small tolerances.

By considering the effect of pixel size on the acquired photon statistics, the utilized CCD detector type may be changed with a sensor array having small pixel size. In this way, the number of photons impinged on detector decrease and bunching effect may be

observed almost all pixels of detector. Furthermore, the optical losses through propagation path (i.e. beam splitter, ND filters, quantum efficiency of detector) may be examined and taken into account for more realistic models since this situation causes random sapling of photons and so less accurate results. Lastly, taking into account the operational principles of Optical Coherence Tomography (OCT) and multi-layer dielectric films, the proposed model for incoherent light statistics could prove useful in determining layer thickness or refractive index profiles.

REFERENCES

Abouraddy, A. F., K. C. Toussaint, A. V. Sergienko, B. E. Saleh, and M. C. Teich (2002). Entangled-photon ellipsometry. *JOSA B 19*(4), 656–662.

Ackermann, G. K. and J. Eichler (2007). *Holography: a practical approach*. John Wiley & Sons.

Afek, I., O. Ambar, and Y. Silberberg (2010). High-noon states by mixing quantum and classical light. *Science 328*(5980), 879–881.

Agarwal, G. S. (2012). *Quantum optics*. Cambridge University Press.

Ahmad, A., T. Mahanty, V. Dubey, A. Butola, B. S. Ahluwalia, and D. S. Mehta (2019). Effect on the longitudinal coherence properties of a pseudothermal light source as a function of source size and temporal coherence. *Optics letters 44*(7), 1817–1820.

Albarelli, F., M. Barbieri, M. G. Genoni, and I. Gianani (2020). A perspective on multiparameter quantum metrology: From theoretical tools to applications in quantum imaging. *Physics Letters A 384*(12), 126311.

Alwis, L., K. Bremer, T. Sun, and K. T. Grattan (2012). Analysis of the characteristics of pva-coated lpg-based sensors to coating thickness and changes in the external refractive index. *IEEE Sensors Journal 13*(3), 1117–1124.

Ataç, E. (2019). *Optical characterization of nanoscale dielectric films on curved surfaces using near field diffraction method*. Ph. D. thesis, Izmir Institute of Technology (Turkey).

Ataç, E. and M. S. Dinleyici (2020). Nanoscale curved dielectric film characterization beyond diffraction limits using spatially structured illumination. *Optical Fiber Technology 58*, 102267.

Ataç, E. and M. S. Dinleyici (2023a). Sensitivity improvement in optical phase diffraction using empirical mode decomposition. In *2023 31st Signal Processing and Communications Applications Conference (SIU)*, pp. 1–4. IEEE.

Ataç, E. and M. S. Dinleyici (2023b). Subwavelength thickness characterization of curved dielectric films exploiting spatially structured entangled photons. *JOSA B 40*(8), 2036–2042.

Ataç, E., A. Karatay, and M. S. Dinleyici (2023). Enhancing thickness determination of nanoscale dielectric films in phase diffraction-based optical characterization systems with radial basis function neural networks. *Measurement Science and Technology 34*(12), 125201.

Bennink, R. S., S. J. Bentley, and R. W. Boyd (2002). "two-photon" coincidence imaging with a classical source. *Physical review letters 89*(11), 113601.

Bennink, R. S., S. J. Bentley, R. W. Boyd, and J. C. Howell (2004). Quantum and classical coincidence imaging. *Physical review letters 92*(3), 033601.

Bernd, D., M. Henriette, H. Gross, et al. (2012). *Handbook of optical systems, volume 5: Metrology of optical components and systems*. John Wiley & Sons.

Bhattacharjee, A., N. Meher, and A. K. Jha (2022). Measurement of two-photon position–momentum einstein–podolsky–rosen correlations through single-photon intensity measurements. *New Journal of Physics 24*(5), 053033.

Boitier, F., A. Godard, E. Rosencher, and C. Fabre (2009). Measuring photon bunching at ultrashort timescale by two-photon absorption in semiconductors. *Nature Physics 5*(4), 267–270.

Bolduc, E., D. Faccio, and J. Leach (2017). Acquisition of multiple photon pairs with an emccd camera. *Journal of Optics 19*(5), 054006.

Boucher, P., H. Defienne, and S. Gigan (2021). Engineering spatial correlations of entangled photon pairs by pump beam shaping. *Optics Letters 46*(17), 4200–4203.

Briggs, I., S. Hou, C. Cui, and L. Fan (2021). Simultaneous type-i and type-ii phase matching for second-order nonlinearity in integrated lithium niobate waveguide. *Optics Express 29*(16), 26183–26190.

Bromberg, J. L. (2016). Explaining the laser's light: classical versus quantum electrody-

namics in the 1960s. *Archive for History of Exact Sciences 70*, 243–266.

Cameron, P., B. Courme, D. Faccio, and H. Defienne (2024). Shaping the spatial correlations of entangled photon pairs. *Journal of Physics: Photonics*.

Catalano, J. (2014). Spontaneous parametric down-conversion and quantum entanglement.

Chan, T. F., G. H. Golub, and R. J. LeVeque (1983). Algorithms for computing the sample variance: Analysis and recommendations. *The American Statistician 37*(3), 242–247.

Chen, L., X. Zhang, J. Lin, and D. Sha (2009). Signal-to-noise ratio evaluation of a ccd camera. *Optics & Laser Technology 41*(5), 574–579.

Chrapkiewicz, R. (2014). Photon counts statistics of squeezed and multimode thermal states of light on multiplexed on–off detectors. *JOSA B 31*(10), B8–B13.

Chunnilall, C. J., I. P. Degiovanni, S. Kück, I. Müller, and A. G. Sinclair (2014). Metrology of single-photon sources and detectors: a review. *Optical Engineering 53*(8), 081910–081910.

Couteau, C., S. Barz, T. Durt, T. Gerrits, J. Huwer, R. Prevedel, J. Rarity, A. Shields, and G. Weihs (2023). Applications of single photons in quantum metrology, biology and the foundations of quantum physics. *Nature Reviews Physics*, 1–10.

Cui, D., X.-L. Wang, X. Yi, and L.-P. Yang (2024). Control of quantum coherence of photons exploiting quantum entanglement. *Physical Review Applied 21*(2), 024019.

D'Angelo, M., M. V. Chekhova, and Y. Shih (2001). Two-photon diffraction and quantum lithography. *Physical review letters 87*(1), 013602.

Debnath, S. K., J. You, and S.-W. Kim (2009). Determination of film thickness and surface profile using reflectometry and spectrally resolved phase shifting interferometry. *International journal of precision engineering and manufacturing 10*, 5–10.

Defienne, H. and S. Gigan (2019). Spatially entangled photon-pair generation using a partial spatially coherent pump beam. *Physical Review A 99*(5), 053831.

Defienne, H., M. Reichert, and J. W. Fleischer (2018). General model of photon-pair detection with an image sensor. *Physical review letters 120*(20), 203604.

DeMille, D., N. R. Hutzler, A. M. Rey, and T. Zelevinsky (2024). Quantum sensing and metrology for fundamental physics with molecules. *Nature Physics*, 1–9.

Demkowicz-Dobrzański, R., J. Kołodyński, and M. Guţă (2012). The elusive heisenberg limit in quantum-enhanced metrology. *Nature communications 3*(1), 1063.

Dennis, P. (2012). *Photodetectors: an introduction to current technology*. Springer Science & Business Media.

Di Giuseppe, G., M. Atatüre, M. D. Shaw, A. V. Sergienko, B. E. Saleh, and M. C. Teich (2002). Entangled-photon generation from parametric down-conversion in media with inhomogeneous nonlinearity. *Physical Review A 66*(1), 013801.

Diament, P. and M. Teich (1970). Photoelectron-counting distributions for irradiance-modulated radiation. *JOSA 60*(5), 682–689.

Dowling, J. P. (2008). Quantum optical metrology–the lowdown on high-n00n states. *Contemporary physics 49*(2), 125–143.

Dowling, J. P. and K. P. Seshadreesan (2014). Quantum optical technologies for metrology, sensing, and imaging. *Journal of Lightwave Technology 33*(12), 2359–2370.

Durak, K. (2020). Optimization of collection optics for maximum fidelity in entangled photon sources. *Turkish Journal of Physics 44*(6), 528–538.

Einstein, A., B. Podolsky, and N. Rosen (1935). Can quantum-mechanical description of physical reality be considered complete? *Physical review 47*(10), 777.

Ekici, Ç. (2021). *A study on entangled photon pairs in graded-index optical fibers*. Ph. D. thesis, Izmir Institute of Technology (Turkey).

Ekici, Ç. and M. S. Dinleyici (2017). A practical approach for optical characterization of a film coated on the optical fiber. *Optical Fiber Technology 36*, 382–386.

Esmaeil Zadeh, I., J. W. Los, R. Gourgues, V. Steinmetz, G. Bulgarini, S. M. Dobrovolskiy, V. Zwiller, and S. N. Dorenbos (2017). Single-photon detectors combining high efficiency, high detection rates, and ultra-high timing resolution. *Apl Photonics 2*(11).

Ficek, Z. and S. Swain (2005). *Quantum interference and coherence: theory and experiments*, Volume 100. Springer Science & Business Media.

Fox, A. M. (2006). *Quantum optics: an introduction*, Volume 15. Oxford University Press, USA.

Garrison, J. and R. Chiao (2008). *Quantum optics*. OUP Oxford.

Gatti, A., M. Bache, D. Magatti, E. Brambilla, F. Ferri, and L. Lugiato (2006). Coherent imaging with pseudo-thermal incoherent light. *Journal of Modern Optics 53*(5-6), 739–760.

Gatti, A., E. Brambilla, M. Bache, and L. A. Lugiato (2004). Correlated imaging, quantum and classical. *Physical Review A 70*(1), 013802.

Gilaberte Basset, M., F. Setzpfandt, F. Steinlechner, E. Beckert, T. Pertsch, and M. Gräfe (2019). Perspectives for applications of quantum imaging. *Laser & Photonics Reviews 13*(10), 1900097.

Giles, J. H., T. D. Ridder, R. H. Williams, D. A. Jones, and M. B. Denton (1998). Product review: selecting a ccd camera. *Analytical Chemistry 70*(19), 663A–668A.

Giovannetti, V., S. Lloyd, and L. Maccone (2006). Quantum metrology. *Physical review letters 96*(1), 010401.

Giovannetti, V., S. Lloyd, and L. Maccone (2011). Advances in quantum metrology. *Nature photonics 5*(4), 222–229.

Glauber, R. J. (1963). The quantum theory of optical coherence. *Physical Review 130*(6), 2529.

Gong, P., X. Li, X. Zhou, Y. Zhang, N. Chen, S. Wang, S. Zhang, and Y. Zhao (2021). Optical fiber sensors for glucose concentration measurement: A review. *Optics &*

Laser Technology 139, 106981.

Goodman, J. W. (2015). *Statistical optics*. John Wiley & Sons.

Grynberg, G., A. Aspect, and C. Fabre (2010). *Introduction to quantum optics: from the semi-classical approach to quantized light*. Cambridge university press.

Guo, Y., C. Peng, Y. Ji, P. Li, Y. Guo, and X. Guo (2018). Photon statistics and bunching of a chaotic semiconductor laser. *Optics express 26*(5), 5991–6000.

Halder, M., A. Beveratos, R. T. Thew, C. Jorel, H. Zbinden, and N. Gisin (2008). High coherence photon pair source for quantum communication. *New Journal of Physics 10*(2), 023027.

Higham, N. J. (2002). *Accuracy and stability of numerical algorithms*. SIAM.

Hloušek, J., M. Dudka, I. Straka, and M. Ježek (2019). Accurate detection of arbitrary photon statistics. *Physical review letters 123*(15), 153604.

Holland, M. and K. Burnett (1993). Interferometric detection of optical phase shifts at the heisenberg limit. *Physical review letters 71*(9), 1355.

Hu, H. (2008). Poisson distribution and application. *A Course in Department of Physics and Astronomy; University of Tennessee at Knoxville: Knoxville, TN, USA*.

Jha, A. K. (2009). *Coherence properties of the entangled two-photon field produced by parametric down conversion*. University of Rochester.

Jönsson, M. and G. Björk (2019). Evaluating the performance of photon-number-resolving detectors. *Physical Review A 99*(4), 043822.

Kapoor, V. and N. K. Sharma (2020). Surface plasmon resonance-based fiber optic sensor prepared from bilayers of indium tin oxide-indium oxide. *Microwave and Optical Technology Letters 62*(7), 2439–2443.

Karan, S., S. Aarav, H. Bharadhwaj, L. Taneja, A. De, G. Kulkarni, N. Meher, and A. K. Jha (2020). Phase matching in β-barium borate crystals for spontaneous parametric

down-conversion. *Journal of Optics 22*(8), 083501.

Karmakar, S. (2019). Super-resolution noninvasive confocal quantum microscope. *Optik 198*, 163209.

Kim, M.-g. (2022). Spectroscopic imaging ellipsometry for two-dimensional thin film thickness measurement using a digital light processing projector. *Measurement Science and Technology 33*(9), 095016.

Klassen, S. (2011). The photoelectric effect: Reconstructing the story for the physics classroom. *Science & Education 20*, 719–731.

Koczyk, P., P. Wiewior, and C. Radzewicz (1996). Photon counting statistics-undergraduate experiment. *American Journal of Physics 64*(3), 240–244.

Kuhn, S., S. Hartmann, and W. Elsäßer (2016). Photon-statistics-based classical ghost imaging with one single detector. *Optics Letters 41*(12), 2863–2866.

Kumar, A. and A. M. Marino (2019). Spatial squeezing in bright twin beams generated with four-wave mixing: Constraints on characterization with an electron-multiplying charge-coupled-device camera. *Physical Review A 100*(6), 063828.

Kumazawa, M., T. Sasaki, and M. Koashi (2019). Rigorous characterization method for photon-number statistics. *Optics Express 27*(4), 5297–5313.

Kuusela, T. A. (2017). Measurement of the second-order coherence of pseudothermal light. *American Journal of Physics 85*(4), 289–294.

Kwiat, P., A. Steinberg, R. Chiao, P. Eberhard, and M. Petroff (1993). High-efficiency single-photon detectors. *Physical Review A 48*(2), R867.

Laiho, K., T. Dirmeier, M. Schmidt, S. Reitzenstein, and C. Marquardt (2022). Measuring higher-order photon correlations of faint quantum light: a short review. *Physics Letters A 435*, 128059.

Landau, L. D. and E. M. Lifshitz (2013). *Statistical Physics: Volume 5*, Volume 5. Elsevier.

Leal-Junior, A. G., A. Theodosiou, C. Marques, M. J. Pontes, K. Kalli, and A. Frizera (2018). Compensation method for temperature cross-sensitivity in transverse force applications with fbg sensors in pofs. *Journal of Lightwave Technology 36*(17), 3660–3665.

Lee, S. M., H. Kim, M. Cha, and H. S. Moon (2016). Polarization-entangled photon-pair source obtained via type-ii non-collinear spdc process with ppktp crystal. *Optics express 24*(3), 2941–2953.

Leuchs, G., R. J. Glauber, and W. P. Schleich (2015). Dimension of quantum phase space measured by photon correlations. *Physica Scripta 90*(7), 074066.

Li, C., W. Yang, M. Wang, X. Yu, J. Fan, Y. Xiong, Y. Yang, and L. Li (2020). A review of coating materials used to improve the performance of optical fiber sensors. *Sensors 20*(15), 4215.

Li, S.-W., F. Li, T. Peng, and G. Agarwal (2020). Photon statistics of quantum light on scattering from rotating ground glass. *Physical Review A 101*(6), 063806.

Lib, O. and Y. Bromberg (2022). Thermal biphotons. *APL Photonics 7*(3).

Liu, Q., J. Sun, Y. Sun, Z. Ren, C. Liu, J. Lv, F. Wang, L. Wang, W. Liu, T. Sun, et al. (2020). Surface plasmon resonance sensor based on photonic crystal fiber with indium tin oxide film. *Optical Materials 102*, 109800.

Liu, Z., I. Ahmed, F. Wen, W. Wang, S. Fan, S. Hui, and H.-X. Wang (2019). Photon bunching and n-photon interference in thermal light. *Optics Communications 434*, 104–109.

Loudon, R. (2000). *The quantum theory of light*. OUP Oxford.

Madonini, F., F. Severini, F. Zappa, and F. Villa (2021). Single photon avalanche diode arrays for quantum imaging and microscopy. *Advanced Quantum Technologies 4*(7), 2100005.

Makris, K. G. and D. Psaltis (2011). Huygens–fresnel diffraction and evanescent waves. *Optics Communications 284*(6), 1686–1689.

Mandel, L. (1958). Fluctuations of photon beams and their correlations. *Proceedings of the Physical Society 72*(6), 1037.

Mandel, L., E. G. Sudarshan, and E. Wolf (1964). Theory of photoelectric detection of light fluctuations. *Proceedings of the Physical Society 84*(3), 435.

Mandel, L. and E. Wolf (1995). *Optical coherence and quantum optics*. Cambridge university press.

Meyer, V., M. Rowe, D. Kielpinski, C. Sackett, W. M. Itano, C. Monroe, and D. J. Wineland (2001). Experimental demonstration of entanglement-enhanced rotation angle estimation using trapped ions. *Physical review letters 86*(26), 5870.

Mishra, S. K. and B. D. Gupta (2012). Surface plasmon resonance-based fiber-optic hydrogen gas sensor utilizing indium–tin oxide (ito) thin films. *Plasmonics 7*, 627–632.

Mishra, S. K., S. P. Usha, and B. D. Gupta (2016). A lossy mode resonance-based fiber optic hydrogen gas sensor for room temperature using coatings of ito thin film and nanoparticles. *Measurement Science and Technology 27*(4), 045103.

Mishra, V., M. Lohar, and A. Amphawan (2016). Improvement in temperature sensitivity of fbg by coating of different materials. *Optik 127*(2), 825–828.

Mitchell, M. W., J. S. Lundeen, and A. M. Steinberg (2004). Super-resolving phase measurements with a multiphoton entangled state. *Nature 429*(6988), 161–164.

Monticone, D. G., K. Katamadze, P. Traina, E. Moreva, J. Forneris, I. Ruo-Berchera, P. Olivero, I. Degiovanni, G. Brida, and M. Genovese (2014). Beating the abbe diffraction limit in confocal microscopy via nonclassical photon statistics. *Physical review letters 113*(14), 143602.

Moomaw, B. (2007). Camera technologies for low light imaging: overview and relative advantages. *Methods in cell biology 81*, 251–283.

Morgan, B. and L. Mandel (1966). Measurement of photon bunching in a thermal light beam. *Physical Review Letters 16*(22), 1012.

Morton, G. (1968). Photon counting. *Applied Optics 7*(1), 1–10.

Nawrocki, W. (2015). *Introduction to quantum metrology: quantum standards and instrumentation*. Springer.

Nestler, P. and C. A. Helm (2017). Determination of refractive index and layer thickness of nm-thin films via ellipsometry. *Optics Express 25*(22), 27077–27085.

Oemrawsingh, S., W. Van Drunen, E. Eliel, and J. Woerdman (2002). Two-dimensional wave-vector correlations in spontaneous parametric downconversion explored with an intensified ccd camera. *JOSA B 19*(10), 2391–2395.

Oppel, S., T. Büttner, P. Kok, and J. von Zanthier (2012). Superresolving multiphoton interferences with independent light sources. *Physical review letters 109*(23), 233603.

Oppel, S., R. Wiegner, G. Agarwal, and J. Von Zanthier (2014). Directional superradiant emission from statistically independent incoherent nonclassical and classical sources. *Physical review letters 113*(26), 263606.

Paul, H. (1982). Photon antibunching. *Reviews of Modern Physics 54*(4), 1061.

Photonics, H. Concepts in digital imaging technology, quantum efficiency. https://hamamatsu.magnet.fsu.edu/articles/quantumefficiency.html. Accessed on: 25/11/2023.

Pieper, K., A. Bergmann, R. Dengler, and C. Rockstuhl (2018). Using a pseudo-thermal light source to teach spatial coherence. *European Journal of Physics 39*(4), 045303.

Pittman, T., D. Strekalov, D. Klyshko, M. Rubin, A. Sergienko, and Y. Shih (1996). Two-photon geometric optics. *Physical Review A 53*(4), 2804.

Pittman, T. B., Y. Shih, D. Strekalov, and A. V. Sergienko (1995). Optical imaging by means of two-photon quantum entanglement. *Physical Review A 52*(5), R3429.

Powers, P. E. and J. W. Haus (2017). *Fundamentals of nonlinear optics*. CRC press.

Premkumar, M. and S. Vadivel (2017). Effect of annealing temperature on structural,

optical and humidity sensing properties of indium tin oxide (ito) thin films. *Journal of Materials Science: Materials in Electronics 28*, 8460–8466.

Rajendran, V., A. Prathuru, C. Fernandez, D. Sujatha, S. K. Panda, and N. H. Faisal (2024). Indium tin oxide thin film preparation and property relationship for humidity sensing: A review. *Engineering Reports 6*(3), e12836.

Rarity, J. and P. Tapster (1990). Experimental violation of bell's inequality based on phase and momentum. *Physical Review Letters 64*(21), 2495.

Reichert, M., H. Defienne, and J. W. Fleischer (2018). Massively parallel coincidence counting of high-dimensional entangled states. *Scientific reports 8*(1), 7925.

Riza, M. A., Y. I. Go, S. W. Harun, and R. R. Maier (2020). Fbg sensors for environmental and biochemical applications-a review. *IEEE sensors journal 20*(14), 7614–7627.

Sabatyan, A. and M. T. Tavassoly (2007). Application of fresnel diffraction to nondestructive measurement of the refractive index of optical fibers. *Optical Engineering 46*(12), 128001–128001.

Sabatyan, A. and M. T. Tavassoly (2009). Determination of refractive indices of liquids by fresnel diffraction. *Optics & Laser Technology 41*(7), 892–896.

Saleh, B. E., A. F. Abouraddy, A. V. Sergienko, and M. C. Teich (2000). Duality between partial coherence and partial entanglement. *Physical Review A 62*(4), 043816.

Saleh, B. E. and M. C. Teich (2019). *Fundamentals of photonics*. john Wiley & sons.

Sampath, U., D. Kim, H. Kim, and M. Song (2018). Polymer-coated fbg sensor for simultaneous temperature and strain monitoring in composite materials under cryogenic conditions. *Applied optics 57*(3), 492–497.

Scarcelli, G., V. Berardi, and Y. Shih (2006). Can two-photon correlation of chaotic light be considered as correlation of intensity fluctuations? *Physical review letters 96*(6), 063602.

Scarcelli, G., A. Valencia, and Y. Shih (2004). Two-photon interference with thermal

light. *Europhysics Letters 68*(5), 618.

Schneeloch, J. and J. C. Howell (2016). Introduction to the transverse spatial correlations in spontaneous parametric down-conversion through the biphoton birth zone. *Journal of Optics 18*(5), 053501.

Scully, M. O. and M. S. Zubairy (1997). *Quantum optics*. Cambridge university press.

Sergienko, A., Y. Shih, and M. Rubin (1995). Experimental evaluation of a two-photon wave packet in type-ii parametric downconversion. *JOSA B 12*(5), 859–862.

Sezemsky, P., D. Burnat, J. Kratochvil, H. Wulff, A. Kruth, K. Lechowicz, M. Janik, R. Bogdanowicz, M. Cada, Z. Hubicka, et al. (2021). Tailoring properties of indium tin oxide thin films for their work in both electrochemical and optical label-free sensing systems. *Sensors and Actuators B: Chemical 343*, 130173.

Shao, Y., Y. Wang, S. Cao, Y. Huang, L. Zhang, F. Zhang, C. Liao, and Y. Wang (2018). Mechanism and characteristics of humidity sensing with polyvinyl alcohol-coated fiber surface plasmon resonance sensor. *Sensors 18*(7), 2029.

Shapiro, J. H. (2009). The quantum theory of optical communications. *IEEE journal of selected topics in Quantum Electronics 15*(6), 1547–1569.

Shih, Y. (1999). Two-photon entanglement and quantum reality. In *Advances in Atomic, Molecular, and Optical Physics*, Volume 41, pp. 1–42. Elsevier.

Shih, Y. (2003). Entangled photons. *IEEE Journal of selected topics in quantum electronics 9*(6), 1455–1467.

Shih, Y. (2007). Quantum imaging. *IEEE Journal of Selected Topics in Quantum Electronics 13*(4), 1016–1030.

Shih, Y. (2012). The physics of ghost imaging. *Classical, semi-classical and quantum noise*, 169–222.

Shih, Y. (2020). *An introduction to quantum optics: photon and biphoton physics*. CRC press.

Shih, Y. and A. Sergienko (1994). A two-photon interference experiment using type ii optical parametric down conversion. *Physics Letters A 191*(3-4), 201–207.

Simon, D. and A. Sergienko (2010a). The correlation confocal microscope. *Optics Express 18*(10), 9765–9779.

Simon, D. and A. Sergienko (2010b). Twin-photon confocal microscopy. *Optics Express 18*(21), 22147–22157.

Simon, D. S., G. Jaeger, and A. V. Sergienko (2017). *Quantum Metrology, Imaging, and Communication*. Springer Cham.

Sirohi, R. S. (2017). *Introduction to optical metrology*. CRC press.

Smith, N., C. Coates, A. Giltinan, J. Howard, A. O'Connor, S. O'Driscoll, M. Hauser, and S. Wagner (2004). Emccd technology and its impact on rapid low-light photometry. In *Optical and Infrared Detectors for Astronomy*, Volume 5499, pp. 162–172. SPIE.

Sparavigna, A. C. (2021). Poissonian distributions in physics: Counting electrons and photons.

Stevens, M. J. (2013). Photon statistics, measurements, and measurements tools. In *Experimental Methods in the Physical Sciences*, Volume 45, pp. 25–68. Elsevier.

Stöhr, J. (2019). Overcoming the diffraction limit by multi-photon interference: a tutorial. *Advances in Optics and Photonics 11*(1), 215–313.

Straka, I., J. Mika, and M. Ježek (2018). Generator of arbitrary classical photon statistics. *Optics Express 26*(7), 8998–9010.

Strekalov, D., T. Pittman, A. Sergienko, Y. Shih, and P. Kwiat (1996). Postselection-free energy-time entanglement. *Physical Review A 54*(1), R1.

Strekalov, D., A. Sergienko, D. Klyshko, and Y. Shih (1995). Observation of two-photon "ghost" interference and diffraction. *Physical review letters 74*(18), 3600.

Takeuchi, S., J. Kim, Y. Yamamoto, and H. H. Hogue (1999). Development of a high-

quantum-efficiency single-photon counting system. *Applied Physics Letters 74*(8), 1063–1065.

Tan, P. K., G. H. Yeo, H. S. Poh, A. H. Chan, and C. Kurtsiefer (2014). Measuring temporal photon bunching in blackbody radiation. *The Astrophysical Journal Letters 789*(1), L10.

Tavassoly, M. T., A. Darudi, H. R. Khalesifard, and S. M. R. S. Hosseini (2001). Applications of fresnel diffraction from phase objects. In *Optical Measurement Systems for Industrial Inspection II: Applications in Production Engineering*, Volume 4399, pp. 98–106. SPIE.

Tavassoly, M. T. and A. Saber (2010). Optical refractometry based on fresnel diffraction from a phase wedge. *Optics letters 35*(21), 3679–3681.

Taylor, M. A. and W. P. Bowen (2016). Quantum metrology and its application in biology. *Physics Reports 615*, 1–59.

Torres, J. P., Y. Deyanova, L. Torner, and G. Molina-Terriza (2003). Preparation of engineered two-photon entangled states for multidimensional quantum information. *Physical Review A 67*(5), 052313.

Turunen, J., A. Halder, M. Koivurova, and T. Setälä (2022). Measurement of spatial coherence of light. *JOSA A 39*(12), C214–C239.

Unternährer, M., B. Bessire, L. Gasparini, D. Stoppa, and A. Stefanov (2016). Coincidence detection of spatially correlated photon pairs with a monolithic time-resolving detector array. *Optics express 24*(25), 28829–28841.

Verma, R. K., A. Joy, N. Sharma, et al. (2019). Performance study of surface plasmon resonance and lossy mode resonance based fiber optic sensors utilizing silver and indium oxide layers: An experimental investigation. *Optics & Laser Technology 112*, 420–425.

Villeneuve-Faure, C., K. Makasheva, C. Diaou, L. Boudou, and G. Teyssedre (2018). Characterization of the electrical behaviour of thin dielectric films at nanoscale using methods derived from atomic force microscopy: application to plasma deposited

agnps-based nanocomposites. In *2018 IEEE 13th Nanotechnology Materials and Devices Conference (NMDC)*, pp. 1–4. IEEE.

Volpe, F. A., P.-D. Letourneau, and A. Zhao (2017). Huygens–fresnel wavefront tracing. *Computer Physics Communications 212*, 123–131.

Waks, E., E. Diamanti, B. C. Sanders, S. D. Bartlett, and Y. Yamamoto (2004). Direct observation of nonclassical photon statistics in parametric down-conversion. *Physical review letters 92*(11), 113602.

Wakui, K., Y. Eto, H. Benichi, S. Izumi, T. Yanagida, K. Ema, T. Numata, D. Fukuda, M. Takeoka, and M. Sasaki (2014). Ultrabroadband direct detection of nonclassical photon statistics at telecom wavelength. *Scientific reports 4*(1), 4535.

Wang, Y., J. Dong, Y. Luo, J. Tang, H. Lu, J. Yu, H. Guan, J. Zhang, and Z. Chen (2017). Indium tin oxide coated two-mode fiber for enhanced spr sensor in near-infrared region. *IEEE Photonics Journal 9*(6), 1–9.

Woyessa, G., K. Nielsen, A. Stefani, C. Markos, and O. Bang (2016). Temperature insensitive hysteresis free highly sensitive polymer optical fiber bragg grating humidity sensor. *Optics express 24*(2), 1206–1213.

Xiang, G.-Y. and G.-C. Guo (2013). Quantum metrology. *Chinese Physics B 22*(11), 110601.

Yoshino, H., A. Abbas, P. M. Kaminski, R. Smith, J. Walls, and D. Mansfield (2017). Measurement of thin film interfacial surface roughness by coherence scanning interferometry. *Journal of Applied Physics 121*(10).

Yu, J., X. Zhu, F. Wang, Y. Chen, and Y. Cai (2023). Research progress on manipulating spatial coherence structure of light beam and its applications. *Progress in Quantum Electronics*, 100486.

Zamarreño, C., M. Hernáez, I. Del Villar, I. Matías, and F. Arregui (2011). Optical fiber ph sensor based on lossy-mode resonances by means of thin polymeric coatings. *Sensors and Actuators B: Chemical 155*(1), 290–297.

Zambra, G., A. Andreoni, M. Bondani, M. Gramegna, M. Genovese, G. Brida, A. Rossi, and M. G. Paris (2005). Experimental reconstruction of photon statistics without photon counting. *Physical review letters 95*(6), 063602.

Zhai, Y.-H., X.-H. Chen, D. Zhang, and L.-A. Wu (2005). Two-photon interference with true thermal light. *Physical Review A 72*(4), 043805.

Zhang, S.-H., L. Gao, J. Xiong, L.-J. Feng, D.-Z. Cao, and K. Wang (2009). Spatial interference: From coherent to incoherent. *Physical review letters 102*(7), 073904.

Zhang, W., R. Fickler, E. Giese, L. Chen, and R. W. Boyd (2019). Influence of pump coherence on the generation of position-momentum entanglement in optical parametric down-conversion. *Optics express 27*(15), 20745–20753.

Zhang, X., H. Alemohammad, and E. Toyserkani (2013). Sensitivity alteration of fiber bragg grating sensors with additive micro-scale bi-material coatings. *Measurement Science and Technology 24*(2), 025106.

Zhou, Z., Y. Xu, C. Qiao, L. Liu, and Y. Jia (2021). A novel low-cost gas sensor for co2 detection using polymer-coated fiber bragg grating. *Sensors and Actuators B: Chemical 332*, 129482.

Zubizarreta Casalengua, E., J. C. López Carreño, F. P. Laussy, and E. d. Valle (2020). Conventional and unconventional photon statistics. *Laser & Photonics Reviews 14*(6), 1900279.

VITA

EDUCATION

2019 - 2024 Doctor of Philosophy in Electronics and Communication Engineering
Graduate School, İzmir Institute of Technology, Turkey
Thesis Title: Dielectric Film Characterization Beyond Classical Limits Exploiting Spatially Structured Entangled Photon Pairs
Supervisor: Prof. Dr. M. Salih Dinleyici

2016 - 2019 Master of Science in Electronics and Communication Engineering
Graduate School of Engineering and Sciences, İzmir Institute of Technology, Turkey
Thesis Title: Optical Characterization of Nanoscale Dielectric Films on Curved Surfaces Using Near Field Diffraction Method
Supervisor: Prof. Dr. M. Salih Dinleyici

2011 - 2016 Bachelor of Electrical and Electronics Engineering
Department of Electrical and Electronics Engineering Dokuz Eylül University, Turkey

PUBLICATIONS

Ataç, E. and M. S. Dinleyici (2023). Subwavelength thickness characterization of curved dielectric films exploiting spatially structured entangled photons. JOSA B 40(8), 2036-2042.

Ataç, E. and M. S. Dinleyici (2020). Nanoscale curved dielectric film characterization beyond diffraction limits using spatially structured illumination. Optical Fiber Technology 58, 102267.